Development of an Air-cooled, Loop-type Heat Pipe with Multiple Condensers

by

Harumichi Arthur Kariya

B.S., Mechanical Engineering, 2005
University of California, Berkeley

S.M., Mechanical Engineering, 2009
Massachusetts Institute of Technology

Submitted to the Department of Mechanical Engineering
in Partial Fulfillment of the Requirements for the Degree of

DOCTOR OF PHILOSOPHY IN MECHANICAL ENGINEERING

AT THE

MASSACHUSETTS INSTITUTE OF TECHNOLOGY

September, 2012

Signature of Author .....
Department of Mechanical Engineering
August 17, 2012

Certified by .....
Evelyn N. Wang
Associate Professor of Mechanical Engineering
Thesis Advisor

Accepted by .....
David E. Hardt
Chairman, Department Committee on Graduate Students

(This page intentionally left blank)

Development of an Air-cooled, Loop-type Heat Pipe with Multiple Condensers

By

Harumichi Arthur Kariya

Submitted to the Department of Mechanical Engineering on August 17, 2012 in partial fulfillment of the requirements for the degree of Doctor of Philosophy in Mechanical Engineering

Abstract

Thermal management challenges are prevalent in various applications ranging from consumer electronics to high performance computing systems. Heat pipes are capillary-pumped devices that take advantage of the latent heat of vaporization of a working fluid to achieve low thermal resistance (~0.1°C/W), and have been of particular interest to address these thermal management needs for cooling solutions such as air-cooled heat sinks.

This thesis reports the design, fabrication, and characterization of a novel loop-type heat pipe with multiple condensers for a high performance air-cooled heat sink. While multiple-condenser heat pipes have been developed in the past, this heat pipe layout is the first to ensure equal operation of the individual condensers. The layout incorporates wicks in both evaporator and condenser; the wick in the evaporator supplies the capillary pressure to drive the circulation and the wick in the condenser uses capillary pressure to separate the vapor and liquid phases for controlled condensation. Additionally, methods of liquid and vapor pressure control are developed to modulate the capillary pressure in the condenser.

The heat pipe was first evaluated using an analytical model to determine the required thermophysical properties and geometries of the capillary wicks in the evaporator and condenser. The model results were subsequently used to obtain a detailed evaporator design that is compatible with the multiple-condenser layout. The evaporator was fabricated with a multi-step metal sintering process, characterized, and integrated into both single-condenser and six-condenser prototypes. The prototypes successfully operated in a wide range of angles, with automatic heat pipe startup and with a heat pipe thermal resistance as low as 0.0065 °C/W with equal condenser performance. The air-cooled, six-condenser prototype demonstrated removal of 500 W from a heat source at 75 °C. The heat pipe cycle developed in this study enables the use of multiple condensers in a loop-type heat pipe to achieve a large surface area with little thermal resistance for heat sink applications.

Thesis Advisor: Evelyn N. Wang
Title: Associate Professor of Mechanical Engineering

(This page intentionally left blank)

Acknowledgements

Entering the doctoral program was a decision to further hone my engineering and analysis skills. At this time of writing, I can appreciate my growth, fostered by the mentoring of Professor Evelyn Wang and the guidance of Professor John Brisson. I thank Professor Wang, my advisor, for the freedom that she entrusted to me, which I feel is key to conducting novel research. I thank Professor Brisson for his critical reviews of my thoughts and experimental methodology; I have developed a similar eye for reviewing my own work as well as those around me. I am likewise inspired to advance myself further.

I would also like to express my appreciation to Professor Bora Mikic for his technical advising, Professor Jeffery Lang for his support in this project and Professor Joseph Smith for teaching me the art of welding as well as patience in fabrication. Similarly, I would like to thank Michael Demaree for teaching me an immense amount of practical knowledge and skills, ranging from precision machining and brazing to charging refrigeration systems. The prototypes presented in this thesis were the result of a team effort and would not have been possible without the other members of the project: Teresa Peters, Martin Cleary, Wayne Staats, Daniel Hanks, Alonso Dominguez-Espinosa, Nicholas Roche, Kai Cao, David Jenicek, Ari Umans and our collaborators at Lockheed Martin as well as the financial support from the Defense Advanced Research Projects Agency (grant number W31P4Q-09-1-0007).

I would equally like to thank my family and friends in Bellflower, Mie and elsewhere around the world for their support and for keeping me in touch with the non-academic world.

I dedicate this dissertation to my mother and father.

(This page intentionally left blank)

Table of Contents

(This page intentionally left blank)

List of Figures

List of Tables

(This page intentionally left blank)

Nomenclature

Abbreviations

CC	Compensation chamber
COP	Coefficient of performance
CPL	Capillary pumped loop
DARPA	Defense advanced research projects agency
HTHE	High temperature heat exchanger
LHP	Loop heat pipe
LTHE	Low temperature heat exchanger
LTHP	Loop-type heat pipe
MCP	Multiple-condenser prototype
RPM	Revolution per minute
SCP	Single condenser prototype

Symbols

A	Area
A_{chan}	Surface area of a vapor channel
$A_{evap\ conv}$	Air-cooled surface area of the evaporator
β	non-dimensional number comparing the convective and conductive effects
C_P	Specific heat
C	Constant
D_h	Hydraulic diameter
f	Friction factor
g	Gravitational acceleration
h	Convective heat transfer coefficient
h_{fg}	Latent heat of vaporization
Δh	Height difference
I_o	Zero-order modified Bessel function of the first kind
I_1	First-order modified Bessel function of the first kind
k	Thermal conductivity
K	Loss coefficient
K_o	Zero-order modified Bessel function of the second kind
K_1	First-order modified Bessel function of the second kind
κ	Permeability
$\dot{m}$	Mass flow rate

m''	Mass flux
μ	Dynamic viscosity
n	Number (of)
P	Pressure, Perimeter
ΔP	Pressure drop
$\Delta P_{cond\ cap}$	Capillary pressure of the condenser wick,
$\Delta P_{evap\ cap}$	Capillary pressure of the evaporator wick
$\Delta P_{max\ cap}$	Maximum capillary pressure
Φ	Non-dimensionalized temperature
Q	Heat
Q_{leak}	Heat leak
Q_{load}	Heat load
r	Radius
R	Thermal resistance
R_{HS}	Thermal resistance of heat sink
R_{INT}	Thermal resistance across the interface between the heat source and heat sink base
R_{TOT}	Thermal resistance between heat source and ambient air
Re	Reynold's number
ρ	Density
t	Thickness
T	Temperature
ΔT	Temperature drop
v	Velocity
W	Distance between the centers of the vapor channels
X	Half-width of the vapor channel cross sectional area
Z	Distance between the evaporator base and the vapor channels

Subscripts

AMB	Ambient
avg	Average
BASE	Base
CC	Compensation chamber
c_case	Condenser case
c_wick	Condenser wick
chan	Vapor channel
cond	Condenser
e_case	Evaporator case
e_wick	Evaporator wick
fin	Fin

inverted	Inverted
l	Liquid
l_line	Liquid line
r	Radial
RES	Reservoir
SAT	Saturation
SOURCE	Source
TOTAL	Total
v	Vapor
v_line	Vapor line
wick	Wick

Chemical Elements

Ag	Silver
Au	Gold
Cu	Copper
Pb	Lead
Sn	Tin

(This page intentionally left blank)

1 Introduction

1.1 Overview

This thesis reports the development of a multiple-condenser, loop-type heat pipe for a high performance air-cooled heat sink. The heat sink is designed to meet a set of required thermal performance metrics. This chapter introduces the layout of the heat sink and its implications on the heat pipe design. Current heat sink technologies are described, and the rationale for selecting a loop-type heat pipe for the heat sink is discussed. The developmental goals for the heat pipe are outlined with respect to the integration into the air-cooled heat sink as well as to address the critical shortcomings of current loop-type heat pipe technology.

1.2 Motivation

Thermal management of modern electronics with rapidly increasing computational performance has become a significant challenge in the past two decades. The heat generated by integrated circuit chips increases with increasing performance, such that heat dissipation is one of the key bottlenecks in performance. In addition to removing significant levels of heat, heat sinks need to maintain the chip within a tolerable temperature range to ensure functionality and minimize degradation over time. As electronics are typically cooled by ultimately transferring the heat to the ambient air, the thermal resistance (R) between the heat source (electronics) and the ambient air is used to characterize the performance of the air-cooling. The total thermal resistance (R_{TOT}) between the source and ambient is defined as:

$$R_{TOT} = \frac{(T_{SOURCE} - T_{AMB})}{Q_{load}} = R_{INT} + R_{HS} \qquad 1.1$$

where T_{SOURCE}, T_{AMB} and Q_{load} are the source and ambient air temperatures and the heat load. The total resistance is the combination of the interface resistance between the electronics and heat sink base and the heat sink thermal resistance between the base and the ambient air, annotated respectively by the subscripts "*INT*" and "*HS*." These components are defined similarly, as:

$$R_{INT} = \frac{(T_{SOURCE} - T_{BASE})}{Q_{load}} \qquad 1.2$$

$$R_{HS} = \frac{(T_{BASE} - T_{AMB})}{Q_{load}} \qquad 1.3$$

where the subscript "*BASE*" refers to the base of the heat sink. The maximum total resistance allowable for the next generation of high performance electronics is predicted by the International Technology

Roadmap for Semiconductors to decrease from 0.11 °C/W in 2013 and 0.07 in 2018 (Figure 1.1) [1]. For reference, the thermal resistance of current commercially-available heat sinks range from 0.1 and 0.3 °C/W and that of commercially available interface materials range between 0.05 and 0.2 °C/W, for a 1600 mm^2 area. To keep pace with the increasing performance of electronics, advanced thermal management solutions are required to decrease the interface and heat sink resistances.

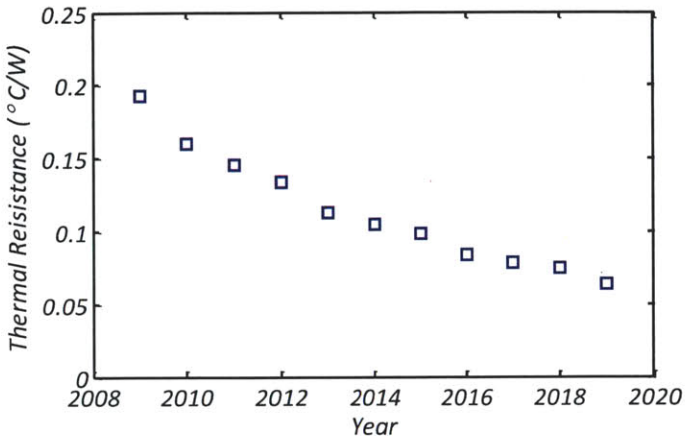

Figure 1.1. Prediction of the allowable thermal resistance for cooling high-performance integrated chips [1]. The decreasing trend is due associated with the increase in heat generation due to the increase in processing speeds.

1.3 Heat Sink Technologies

To achieve the required heat sink thermal resistances in the near future, it is instructive to understand the current heat sink technology. Common air-cooled heat sinks include metal fins, refrigeration systems, single-phase liquid cycles and two-phase cycles. These technologies differ considerably both in the thermal resistance in transferring the heat to the air-cooled surface and the required power input for operation. Table 1.1 shows a comparison of the performance of commercially available heat sinks utilizing some of these technologies. The coefficient of performance (COP) is defined as the removed heat load divided by the power (electrical) required to operate the heat sink. Refrigeration systems are not included in the table as the definition of thermal resistance is not directly applicable.

Table 1.1. Comparison of commercially available air-cooled heat sinks.

Heat Sink (Type)	*Volume / Heat (cm^3/W)*	*Thermal Resist. (°C/W)*	*Coefficient of Performance*
Aluminum Fin	*2.89*	*0.32*	*57.9*
Liquid circulation + Radiator	*10.42*	*0.09*	*41.7*
2 Heat Pipes + Plate Fins	*4.27*	*0.28*	*83.3*
5 Heat Pipes + Plate Fins	*25.97*	*0.10*	*53.6*

1.1.1 Metal Fins

Copper or aluminum fins are commonly used in low heat load applications or on the air-cooled section of refrigeration, single-phase or two-phase systems. The fin structure is typically milled, cast or pressed to achieve a large surface area for a given footprint area, and is integrated with a fan for forced air-flow. Table 1.1 shows that compared to the other technologies, a smaller volume is required to remove the same level of heat because the heat is accepted and rejected by the same body. The thermal resistance is limited by the fin efficiency, which can be improved by increasing the thermal conductivity of the fin structure and by enhancing the convective heat transfer coefficient.

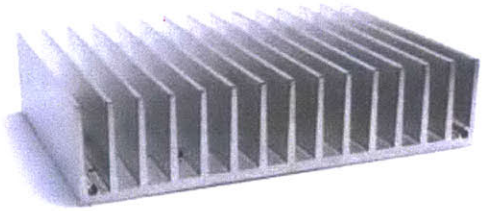

Figure 1.2. Metal fin heat sink, shown without a fan [2].

1.1.2 Refrigeration Systems

Refrigeration systems include fluidic cycles (*i.e.* vapor compression cycle) and solid state systems. Both allow for sub-ambient cooling, at the cost of additional energy input. Even in an ideal system, sub-ambient cooling results in a greater inflow of entropy from the heat source than the outflow to the ambient air. The difference requires an energy input, which in the fluidic cycle is the energy required at the pump (compressor), and in a solid state system, the energy required to induce the thermoelectric effect. As a result, the air-cooled side of refrigeration systems must remove a greater amount of heat than that which enters the system from the heat source (electronics). Thus, while sub-ambient cooling is possible, these systems are typically large, with a low COP.

1.3.1.1 Fluidic cycles

Fluidic refrigeration cycles use a working fluid, typically a fluorocarbon, to extract the heat through evaporation at a sub-ambient temperature. The heat is removed from the working fluid by a heat exchanger to the ambient air. A mechanical pump actively increases the fluid pressure for circulation through a throttle, and accounts for a large portion of the energy cost. The requirement for a pump and heat exchanger results in a sizable device: the size of a miniature refrigeration cycle for CPU cooling developed by Trutassanawin *et al.* was predominantly the pump (85 cm diameter x 166 mm height) and the heat exchanger (45 mm x 18 mm x 25 mm) [3]. The COP of the device ranged from 3 to 6.

1.3.1.2 Solid State Systems

Solid state systems use the thermoelectric (Peltier-Seebeck) effect to transfer the heat from the electronics to the air. A temperature gradient is produced in the thermoelectric, and the hot side is cooled by a heat exchanger. However, the COP of typical thermoelectrics lies between 0.3 and 1 [4-6],

and are therefore primarily used for cooling only specialty equipment such as optical detectors and lasers.

1.1.3 Single-Phase Liquid Cycles

Single-phase liquid cycles connect heat transfer with mass transport, *via* a circulating liquid flow. The liquid circulates from a high temperature heat exchanger (HTHE) at the heat source to an air-cooled, low temperature heat exchanger (LTHE) where it is cooled (Figure 1.3). The HTHE can be designed independently of the LTHE. Circulation is driven by a pump, which is typically mechanical. As shown in Table 1.1, an advantage of the liquid circulation cycle is the low thermal resistance. Once the heat enters the working fluid though the HTHE, the thermal energy can be transported through long distances with little temperature drop. The resistance to this transport is fluidic in nature, and can be overcome by the pump. Thus, the temperature drop between the HTHE and the LTHE is a function of the flow rate, or the pumping power.

The past two decades has seen significant research in the field of high heat flux (> 100 W/cm^2), low heat load (< 200 W) removal, focusing on the design of the HTHE, which in this case becomes a noticeable constriction in the heat transfer [7, 8]. With large gains in (liquid) convective heat transfer through micro-channels, heat fluxes of up to 790 W/cm^2 have been achieved by Tuckerman and Pease using a pumping pressure of 214 kPa [9]. Methods of spray and jet-impingement cooling have also been implemented to increase the local heat transfer coefficient. Fabbri, Jiang and Dhir demonstrated a heat removal of up to 300 W/cm^2 through liquid water impingement [10]. However, as substantial viscous losses occur across micro-channels and nozzles, the high heat flux is removed at the cost of high pumping power. Additionally, as shown in Table 1.1, these systems characteristically have a large volume to heat ratio; over 80% of the size is attributed to the pump and radiator.

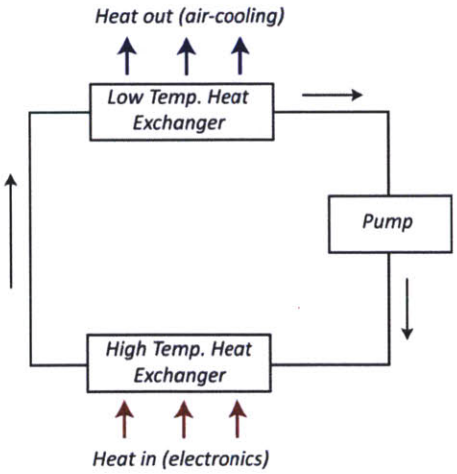

Figure 1.3. Circulation cycle of single-phase liquid cooling. The circulation, marked by the black arrows, is driven by a pump. A similar cycle is used for two-phase cooling.

1.1.4 Two-Phase Cycles

Two-phase cycles share the same advantages and cycle layout as the single-phase cycles. Heat enters and leaves the fluid at the HTHE and the LTHE respectively, with boiling/vaporization occurring in the HTHE. Two-phase cycles can be simplified into two types: cycles driven by an active pump and cycles driven by passive pumping. Various designs for passively pumped cycles exist depending on the mechanism of pumping and circulation.

1.3.1.3 Pumped Two-Phase Cycles

In a pumped cycle, the vapor quality at the exit of the HTHE is dependent on the heat load and flow rates. The use of the latent heat increases the effective heat capacity for a given mass flow. Due to the potential of high heat flux removal from two phase flows in mini and micro-channels, much work has been documented in characterizing the thermal and fluidic properties of flow boiling in small scales [7, 8, 11, 12]. Mini and micro-channels and pin fin arrays have demonstrated the removal of heat fluxes up to 250 W/cm^2 [13-15]. Sung and Mudwar used two-phase jet impingement to remove a heat flux of 1127 W/cm^2 with a pumping pressure of 159 kPa [16, 17].

1.3.1.4 Thermosyphons and Heat Pipes

Passively pumped cycles typically contain the working fluid with a hermetic seal, with little or no non-condensable gases. Unlike flow boiling cycles, the mass flow rate of the fluid is directly coupled to the heat removal rate though the latent heat, and only vapor exits the HTHE. Due to this discrete phase change before and after the HTHE, the HTHE is referred to as the "evaporator" and the LTHE is the "condenser." These cycles are categorized by the mechanism of pumping, as thermosyphons or heat pipes. Thermosyphons use gravity to return the condensate to the evaporator (Figure 1.4A). Hence the condenser must be elevated above the evaporator for functionality [18, 19]. Heat pipes circulate the working fluid using capillary pressure, generally from a micro-porous wicking structure (Figure 1.4B). The wick connects the evaporator and condenser, and evaporation and condensation occur on the surface of the wick. The capillary pressure generated upon evaporation pushes the vapor to the condenser and pulls the condensate through the wick [18-21]. The menisci formed on the surface of the wick separate the vapor and liquid phases. Thermosyphons and heat pipes characteristically have negligible temperature gradient, as the hot vapor has access to the entire chamber volume.

In addition to the heat pipe described above (hereon "conventional heat pipe"), capillary pumping is also used in different geometries. Loop-type heat pipes (LTHPs) also utilize passive capillary pumping with a modified version of the heat pipe cycle, in which the vapor and liquid flow through separate lines. While conventional heat pipes require a wick to separate the vapor and liquid phases in the countercurrent flow, the liquid line in LTHPs can be un-wicked. A wick is required only in the evaporator for capillary pumping. Figure 1.5 shows a LTHP developed at Thermacore [22]. The evaporator and condenser are separate components, connected by two lines to form a circulation loop. This configuration results in less viscous pressure loss in the cycle and thus an significant improvement in the capillary and viscous limits before failure, and also eliminates the entrainment limit seen in conventional heat pipes [18, 19, 23].

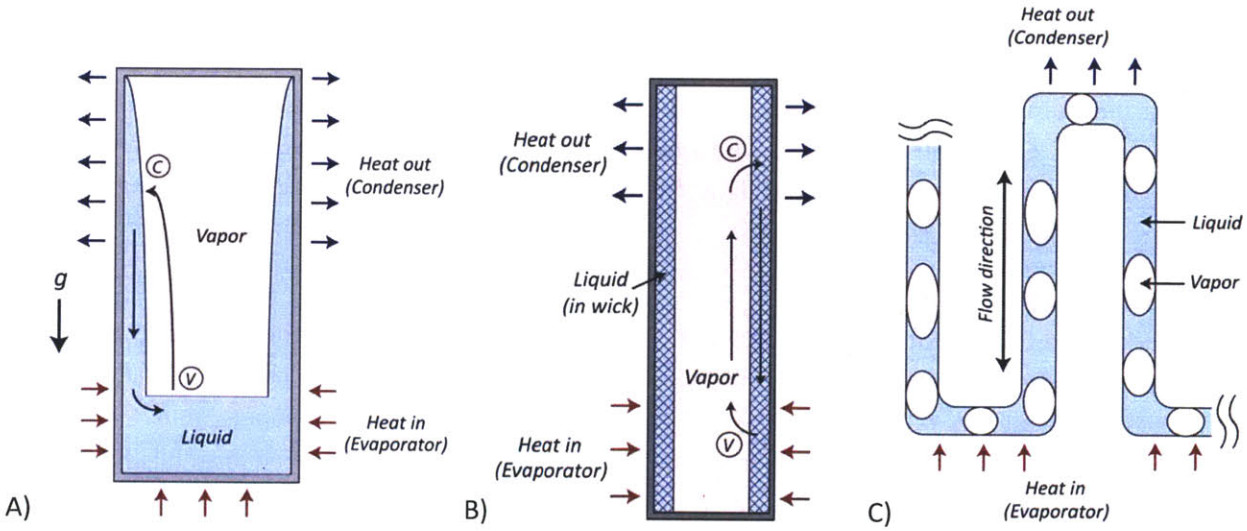

Figure 1.4. Schematics of two-phase cycles. A) shows the thermosyphon cycle, with gravity-fed circulation. B) shows the heat pipe cycle, with circulation driven by the capillary pressure from a porous wick (shown hatched). C) shows the pulsating heat pipe, with the vapor plugs. Heat enters the evaporator section and leaves from the condenser section. The black arrows trace the circulation path and "V" and "C" indicate vaporization/boiling and condensation, respectively.

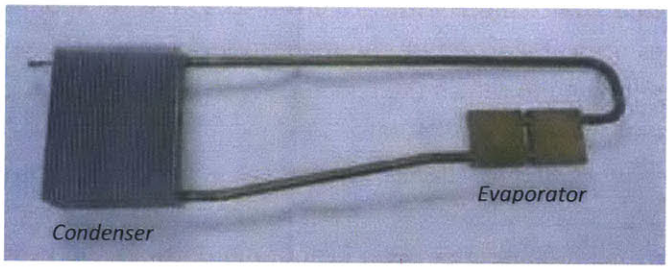

Figure 1.5. Photograph of a LTHP (loop heat pipe), developed at Thermacore Europe. The labels were added for this figure [22].

Pulsating heat pipes also use capillary pressure for circulation, but without a wick [21, 24-26]. A narrow tube with a diameter near (or smaller than) the capillary length is bent in a switchback configuration, as shown Figure 1.4C. The length of each straight section is at least an order of magnitude longer than the diameter. When one set of bends is heated (evaporator), a mix of plugs/slugs of vapor and liquid is generated. The other set of bends is cooled (condenser) to remove the heat. A series of capillary menisci is formed in the tube, resulting in vapor lock. When one of the heated bends generates a high vapor pressure in a vapor plug, the vapor lock is temporarily disrupted, causing a pulse of fluid movement. Since this can be caused by any heated bend, the direction of the pulse is random. Pulsating heat pipes inherently have a larger thermal gradient than thermosyphons and heat pipes because the high temperature vapor is confined to the local vapor plugs.

Due to the ability to utilize the latent heat of the working fluid for heat removal without a mechanical pump, conventional heat pipes have recently become incorporated with metal fin heat sinks to serve as efficient thermal conductors to decrease the overall thermal resistance. A conventional heat sink with heat pipes is shown in Figure 1.6. The evaporator is attached to a base plate, which is mounted to the heat source. An array of thin aluminum or copper fins is attached onto the condenser at the opposite end of the heat pipe. With this layout, the heat pipes are used to transfer heat to a greater number of fins for a larger air-cooled surface area. The performance of two such heat sinks is shown in Table 1.1. The size of the fins scales with the number of heat pipes. The heat sink with two heat pipes shows modest improvement over the aluminum fin heat sink, and the use of five heat pipes significantly improves the thermal resistance (0.1 °C/W) while maintaining a high COP (53.6). However, the increase in surface area is achieved at the cost of a larger heat sink size. This is due to the inefficiency of the LTHE, specifically the conductive resistance inherent in the thin plate fins.

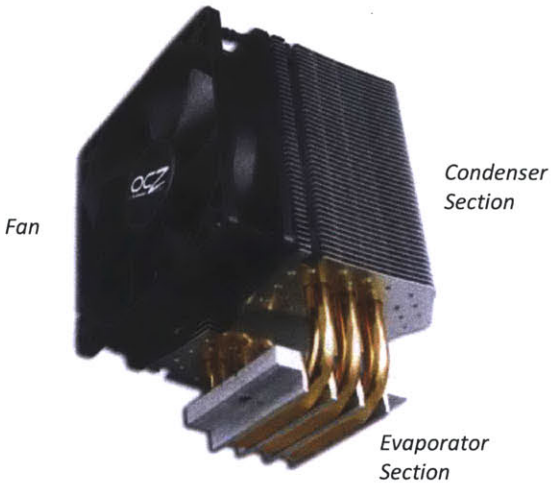

Figure 1.6. Conventional heat pipe heat sink [27]. In this heat sink, the heat pipes are bent in a U shape, with the heat applied at the bend (evaporator). Aluminum fins are attached to the ends of the heat pipe (condensers). A fan is used to blow air into the fin array. The labels were added for this figure.

1.4 Advancement of Heat Sink Technology

To advance heat sink technology, Defense Advanced Research Projects Agency (DARPA) has developed a program soliciting new technology to meet a set of metrics to improve the performance of air-cooled heat sinks, which includes a thermal resistance of 0.05 °C/W [28]. The metrics (hereon, "DARPA metrics") are shown in Table 1.2. The solicited heat sink is to remove 1000 W using 33 W of input power while fitting within a cube with a side dimension of 101.6 mm. The heat must enter through one face (101.6 mm x 101.6 mm) of the cube and the entire volume can be used for the air-cooled heat removal. As a reference, the predicted performance of a comparable heat sink utilizing current technology, as included in the DARPA call, is also shown in the table. The COP of this heat sink is markedly lower (10) than the other commercially available heat sinks in Table 1.1 due to the larger air flow required for heat

removal from a compact volume (1 cm^3/W); it is predicted that the fan will occupy 75% of the heat sink volume. Thus, the call solicits a compact, high heat load heat sink with a 75 % lower thermal resistance and 67% higher COP than the current state-of-the-art.

Table 1.2. DARPA metrics, shown with the metrics for the state-of-the-art heat sink reported in the call. While the dimensions are reported in inches, the equivalent in millimeters will be referenced in this thesis.

Metric	*DARPA Targets*	*DARPA Predicted State-of-the-Art*
Thermal Resistance	*0.05 °C/W*	*0.2 °C/W*
Total Size	*4" x 4" x 4"*	*4" x 4" x 4"*
Coefficient of Performance	*30*	*10*
Heat Removal	*1000 W*	*1000 W*
Volume / Heat	*1 cm^3/W*	*1 cm^3/W*

1.5 The Air-cooled, Multiple-Condenser Heat Pipe

Based on the prior review of cooling technologies, the single and two-phase cycles demonstrate that efficient heat transfer is possible by coupling heat transfer with mass transfer. The thermal resistance of these systems is strongly affected by the air cooling of the LTHE. The critical challenge to meet the DARPA metrics is therefore the development of a fluidic cycle with a LTHE that has low thermal resistance and capable of removing high levels of heat with a compact volume. Passively pumped two-phase cycles are ideal for this application, as heat is transferred through the latent heat of vaporization with little temperature drop and passive pumping conserves space by eliminating the need for a mechanical pump.

To fulfill the DARPA metrics, a heat sink with a LTHP and a custom-designed fan is proposed. The design is shown in Figure 1.7. The LTHE is an interdigitated, or alternating, stack of fan impellers and planar fins; the planar fins serve as the condensers of the two-phase cycle. Heat enters at the evaporator base and is transferred to the condensers by mass transport through two vapor and two liquid pipes. The thermal gradient on the air-cooled surface is minimized as the majority of the condenser area is maintained at approximately the vapor temperature. The impellers are mounted on a central shaft driven by a planar, three-phase brushless motor with an electrical-to-mechanical conversion efficiency greater than 90% [29]. Rotation of the impellers draws air from the top of the device and into the central core. The air then enters into the rotation space of the individual impellers, cooling the condensers and exiting radially outwards. Heat transfer with the air is improved in the following ways:

1) The fins (condensers) are nearly isothermal at the vapor temperature, ensuring that the air-cooling occurs at the highest temperature possible. Use of multiple condensers increases the surface area available for air cooling.
2) All of the air flow generated by the fan is used for cooling the condensers, minimizing the mechanical work required. This is in contrast to the heat sink shown in Figure 1.6, where the fan

is used to blow air at the heat sink. A fraction of the air does not flow through the fins and mechanical energy is wasted.

3) The impellers are placed in close clearance to the condensers so that the impeller blades intermittently disrupt the thermal boundary layer and induce mixing. The convective heat transfer coefficient is enhanced as the heat transfer locally resembles that of turbulent flow. The details are explained in references [30, 31]

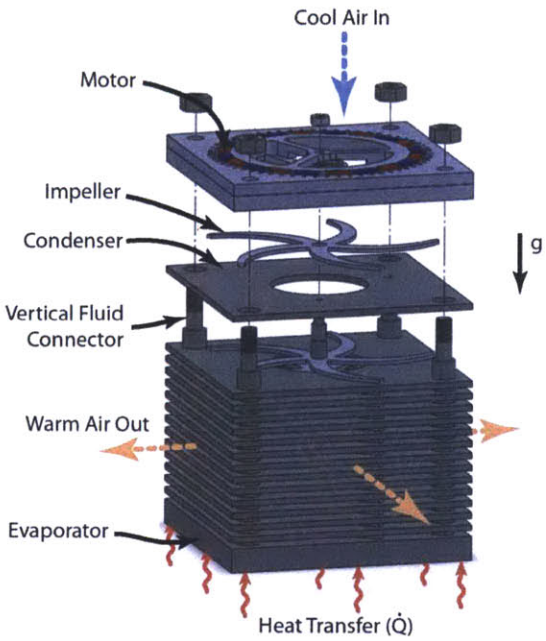

Figure 1.7. Schematic of the air-cooled heat sink design [30]. The layered structure constitutes the heat pipe. The thick bottom plate is the evaporator, and the multiple thin plates stacked above are the condensers. A low-profile motor is mounted on top of the structure, driving a shaft that spins the impellers that rotate between the condensers.

The heat sink layout requires a single evaporator and multiple condensers. This configuration prevents the use of a conventional heat pipe: while a single evaporator can be connected to an intersection with multiple legs for condensers, the large liquid flow rates through the wick between the intersection and the evaporator will lead to the viscous or capillary limit of failure [18, 19, 23]. The multiple-condenser configuration is instead achieved with a LTHP. However, due to the absence of a wick to guide the liquid transport, the liquid pressure in LTHPs becomes an important factor in determining the distribution of the liquid as well as the operating temperature. The different mechanisms of liquid pressure control leads to two types, the "loop heat pipe" (LHP) and "capillary pumped loop" (CPL) [21, 32-34].

1.1.5 Operation of Loop-type Heat Pipes

The LHP cycle is shown schematically in Figure 1.8. With the application of heat to the evaporator, the working fluid is vaporized from the surface of the wick (1). The vapor exits the evaporator through the vapor channels and flows through the vapor lines to the condenser (2), undergoing a pressure drop in the process. Upon entering the condenser, the vapor is cooled and releases the latent heat of

vaporization (3). The condensate is sub-cooled (4) and returns to the liquid-side of the evaporator (5), undergoing a noticeable temperature increase. The viscous pressure loss in the liquid return line is typically negligible. Finally, the liquid flows across the wick (6) undergoing a viscous pressure drop and temperature increase, and the cycle is repeated.

LHPs have two distinct features. First, circulation is driven by the capillary pressure of the evaporator wick. The capillary pressure is the difference between the pressures at (1) and (6), and must overcome the cumulative pressure losses in the cycle. Secondly, thermodynamic saturation occurs at three locations: in the vapor channels, in the condenser and in the open liquid space in the evaporator (5), conventionally called the "compensation chamber" (CC) [23, 32-35]. These three locations effectively determine the operating (vapor) temperature of the LHP, and as a result, much research is directed at controlling the CC temperature to actively modulate the LHP temperature [36]. The CPL can be considered to be a derivative of the LHP, in which the location of saturation is relocated from the CC to a heated tank (5') attached to the liquid return line for greater temperature control (Figure 1.9). This tank is conventionally called a "reservoir" [32, 34]. By maintaining saturation, the CC and reservoir are typically two-phase, and compensate for the volume change (thermal expansion) of the working fluid by expanding and contracting the size of the vapor region [23, 33].

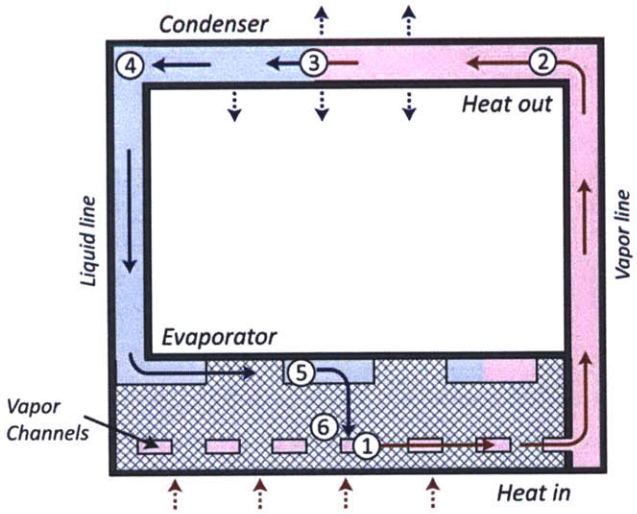

Figure 1.8. Loop heat pipe cycle. The pink and blue regions indicate vapor and liquid. The hatched region represents the wick. Note the presence of vapor at (5)

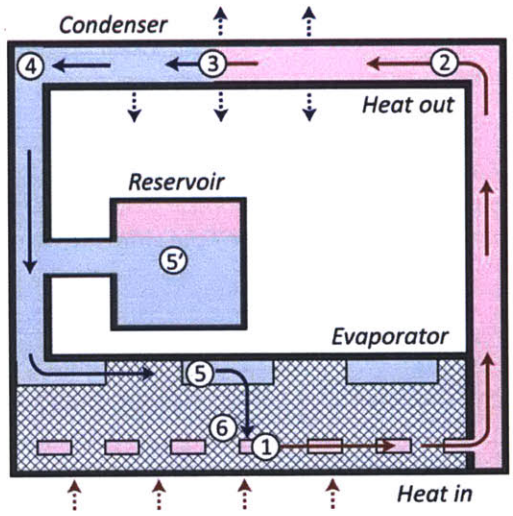

Figure 1.9. Capillary pumped loop cycle. The pink and blue regions indicate vapor and liquid. The hatched region represents the wick. Note the presence of vapor at (5'), in the reservoir.

Due to the physical separation of the evaporator and condenser as well as the improvement in the operating limits, LTHPs offer significantly greater flexibility in design than conventional heat pipes. LHPs have been used in large-scale applications, such as frost prevention of exposed water pipelines in sub-zero climates, and capillary pumping has been demonstrated for LTHPs of up to 10 meters in length [37].

Meter-scale LTHPs have been tested to remove 1000-1500 W of heat [21, 33, 35]. Multiple-condenser, multiple-evaporator LHPs and CPLs have been developed for aerospace applications in order to maintain multiple heat sources at similar temperatures [33, 38-42]. With the greater demand of thermal management for electronics in the past decade, miniature, or sub-meter, LTHPs have been developed for cooling electronics [43, 44]. While most of these heat pipes consist of liquid-cooled condensers for high heat removal, some have focused on air-cooled condensers for practical applications. Pastukhov *et al.* characterized multiple air-cooled LHP heat sinks for heat loads up to 120 W [37]. More recently, Singh *et al.* demonstrated an air-cooled LHP operating with a heat load between 20 and 70 W [45]. While the LHPs were shown to have thermal resistances as low as 0.3 °C/W and 0.17 °C/W, respectively, the total thermal resistances were substantially higher due to the convective thermal resistance at the condenser, at 1.7- 4 °C/W and 1-2 °C/W, respectively. The high thermal resistance in both cases was due to the simplicity of the condenser and fan designs.

1.6 Objective of Work: Development of a Loop-Type Heat Pipe with Multiple Condensers

The LTHP is utilized in the heat sink as a near-isothermal body. The dominant temperature drop, or thermal resistance, occurs between the condenser surface and the ambient air. It is therefore critical that the each condenser reliably operates at the vapor temperature and dissipates the maximum (and thus the same amount of) heat for a given operating condition. Furthermore, the LTHP must start automatically with the application of heat to prevent overheating the electronics.

However, in contrast to conventional heat pipes, in which the location of the vapor and liquid are physically defined, the location of the vapor and liquid in LTHPs are dependent on the initial and operating conditions. CPLs generally require a priming procedure prior to startup to correctly distribute the phases in the heat pipe, which can take up to multiple hours [32, 34]. Due to the lack of vapor-liquid phase separation in the non-wicked condenser, the vapor and liquid can occupy different locations of the condenser depending on the orientation. This affects the condensation behavior and therefore the thermal resistance of the LTHP [35, 46]. In a multiple-condenser system, this can cause the vapor and liquid distribution among the condensers to change, staggering the performance of individual condensers. As a result, the integration of LTHPs is currently limited to particular applications such as large scale or high heat generation systems, or those that necessitate multiple-condensers or multiple-evaporators with relatively small orientation changes.

This thesis reports the development of a novel LTHP layout that addresses the shortcomings described above, in order to produce a multiple-condenser LTHP that is easy-to-use, robust, and low in thermal resistance. Specifically, the heat pipe is designed to:

1) Start immediately upon the application of heat, without operator involvement.
2) Operate with equal and optimal performance in all condensers. Wicks are integrated into the condensers and mechanisms of operator control of liquid pressure in both LHP and CPL modes

are developed for this purpose. Previous studies of multiple-condenser LTHPs do not detail the performance of the individual condensers.

3) Operate with a low heat pipe thermal resistance (<< 0.05 °C/W), with the option of higher thermal resistances, as set by the operator. Mechanisms of operator control of vapor pressure in CPL mode are developed for this purpose.
4) Operate in a range of angles with constant thermal resistance.

This development therefore is not confined to a device-specific study, but is a step towards bringing LTHPs from unique and research-grade uses to a more practical and diverse range of applications.

1.7 Thesis Outline

This thesis begins with the evaluation of the total heat pipe design and follows with a detailed design study of the evaporator. Single-condenser and six-condenser prototype heat pipes are then developed and characterized to show that the above goals are fulfilled.

Chapter 2 introduces the thermal-fluidic cycle of the multiple-condenser heat pipe with wicks integrated in the condensers. The relationships between the temperatures and pressures are outlined, and the fundamental requirements for operation with equal condenser performance are derived.

Chapter 3 reports an analytical model to understand the operating behavior of the multiple condenser heat pipe. The model is used to evaluate the effect of the wick properties, and the wicks for the evaporator and condenser are selected based on their ability to fulfill the requirements developed in Chapter 2.

Chapter 4 describes the development of the evaporator. The wick selected in Chapter 3 is used as the basis of two and three dimensional modeling to design the evaporator to meet the DARPA metrics. The fabrication procedure is then described, and the results from experimental testing are presented. The results are compared with the predictions from the modeling to confirm evaporator functionality to the required specifications.

Chapter 5 presents the construction and characterization of an air-cooled, single-condenser version of the heat pipe. The results of the testing are used to analyze the parameters that affect the total thermal resistance as well as confirm that the requirements developed in Chapter 2 are met. The heat pipe is operated in two modes, as a LHP and a CPL, and operator control of the liquid and vapor pressures are demonstrated.

Chapter 6 presents the construction and characterization of an air-cooled, six-condenser version of the heat pipe. The operating limits for equal condenser performance and the parameters that affect the thermal resistance are described. Modes of operator control of liquid and vapor pressure are presented and compared with those observed for the single-condenser version in Chapter 5. The characterization serves as the proof-of-concept of the air-cooled multiple-condenser heat pipe for meeting the DARPA metrics.

Chapter 7 summarizes the heat pipe development. Key factors that affect the operating characteristics are highlighted.

1.8 Impact of Work

This development leads to the following advancements in heat pipe technology that have not been previously documented in literature:

1) Utilization of a wick in the condenser to ensure equal condenser performance in a multiple-condenser layout. This enables multiple modular condensers to be used in LTHPs to increase heat load capacity.
2) Operation of a LTHP in both LHP and CPL modes, with a seamless transition between the modes.
3) Operator control of liquid and vapor pressures to actively adjust the condenser performance.

(This page intentionally left blank)

2 Thermal-fluidic Cycle of the Multiple-Condenser Heat Pipe

2.1 Overview

This chapter describes the operation of the multiple-condenser loop-type heat pipe and outlines the fundamental requirements for developing the condenser and evaporator. The temperature and pressure relationships are described for the LHP cycle, and requirements for forming capillary pressure in the condenser and maintaining stable liquid pressure are derived. The analysis for the LHP cycle is then extended to derive the requirements for the CPL cycle. For the remainder of this thesis, all reference to "heat pipes" will assume loop-type heat pipes.

2.2 Thermal-fluidic Cycle of the Multiple-Condenser Heat Pipe

The modular nature of the LHP components allows for flexibility in design. Multiple evaporator systems allow for multiple heat sources to be maintained at equal temperatures and multiple condensers allow for an increase in heat removal area. However, unlike the vertically stacked multiple condenser layout developed in this study, past studies have documented the operation of multiple-condenser LHPs with equal condenser heights or have not reported on the individual performances of the condensers [38-42, 47]. A stacked configuration results in unequal liquid pressures in the condensers due to a gravitational pressure head. While the vapor pressures are approximately equal in the condensers, the lower condenser will have a higher liquid pressure, which can cause it to flood with liquid.

To prevent flooding, the multiple condenser heat pipe developed in this study integrates a wick in the condenser. A cross sectional schematic is shown in Figure 2.1. The wick lines the inner surfaces of the condenser and separates the vapor (pink) and liquid (blue) spaces. Condensation occurs on the surface of the wick, and the condensate flows through the wick to exit the condenser and return to the evaporator. The wick fixes the area for condensation by removing the condensate from the vapor space and maintaining an interface between the vapor and liquid. The interface menisci supply the capillary pressure required to compensate for the gravitational pressure head in the liquid. As a result, the liquid pressure is decoupled from the vapor pressure and condensation behavior.

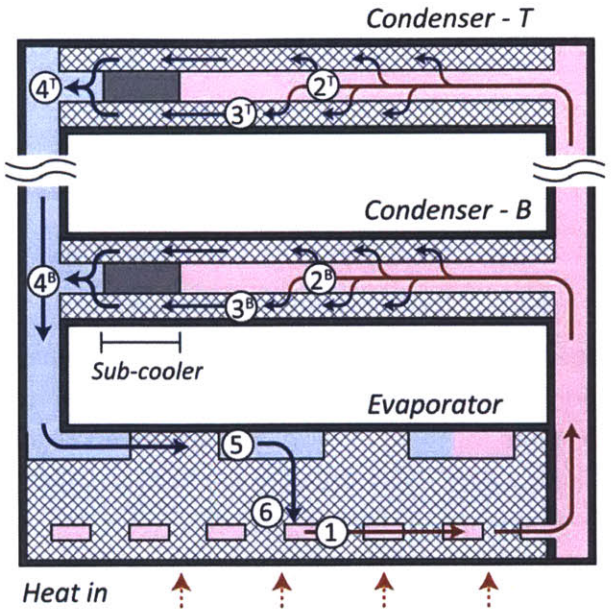

Figure 2.1. Multiple-condenser loop heat pipe cycle. The pink and blue regions indicate vapor and liquid, which are physically separated by the wicks (shown hatched) in the evaporator and condenser. Menisci are formed at the interface between the vapor and the wicks, which are saturated with liquid. The phase separation allows for identical condensation behavior in each of the condensers regardless of different liquid pressures. The schematic shows the upright orientation.

To achieve proper phase separation in the condenser and form menisci on the wick surface, the vapor and liquid pressures need to be modulated. To understand the operating conditions of the cycle, the pressures and temperatures for a dual-condenser LHP are shown in Figure 2.2 for both the upright (evaporator at the bottom) and inverted (evaporator at the top) cases. Water is used as the working fluid, due to the high latent heat of vaporization and capillary pressure, as well as a two-phase temperature range that matches that which is required for cooling electronics [18-20]. The vapor and liquid lines are approximated as adiabatic to simplify the description. "T" and "B" indicate the top and bottom condensers, respectively, where the bottom condenser is located at the same height as the evaporator. In this discussion, "top" and "bottom" will refer to the particular condensers, and "lower" and "upper" will refer to the condensers relative to orientation (effect of gravity). Furthermore, the wicks in the evaporator and condenser will be referred to having an average "meniscus" instead of "menisci." The cycles in Figure 2.2 illustrate the case just prior to the onset of flooding, where the liquid and vapor pressures become equal for the lowest condenser for the upright and inverted orientations. The upper condenser operates at lower liquid pressures, by the amount of the gravitational pressure head between the condensers.

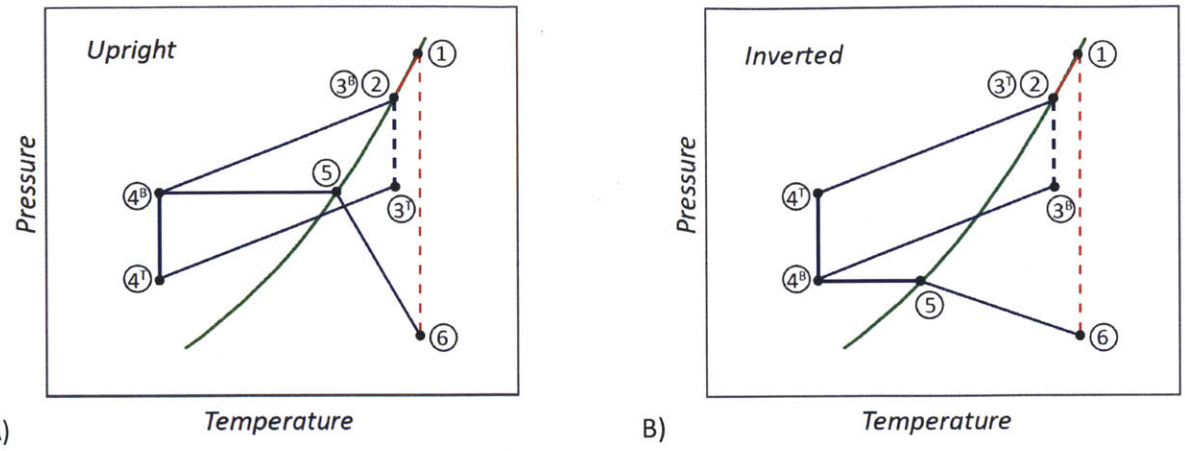

Figure 2.2. Pressures and temperature of the multiple-condenser LHP cycle, plotted schematically for A) upright and B) inverted orientations. The solid red and blue lines correspond to the vapor and liquid phases, respectively, and the green line indicates the saturation curve. The dashed lines represent the capillary pressure differentials.

Analyzing the upright case, the cycle starts with vaporization at saturation (1):

$$T_1 = T_{SAT}@P_1 \qquad 2.1$$

The vapor incurs a pressure drop as it exits the evaporator through the vapor channels and enters the condenser (2) through the vapor line:

$$P_2 = P_1 - \Delta P_{1-2} \qquad 2.2$$

Condensation occurs at the saturation temperature of the local pressure:

$$T_2 = T_{SAT}@P_2 \qquad 2.3$$

Following the circulation through the bottom condenser, the temperature and pressure are the same before (2) and after condensation (3), and thus a capillary pressure differential is not present across the condenser wick surface:

$$P_{3B} = P_2 \qquad 2.4$$

$$T_{3B} = T_2 \qquad 2.5.$$

This condition represents the limit before flooding occurs. An actual cycle will utilize a capillary pressure differential ($P_2 > P_3$) in every condenser as a precautionary safety factor against flooding. The condensate flows through the wick and undergoes a viscous pressure decrease and temperature decrease (sub-cooling) in the process. Sub-cooling is defined here as the temperature decrease from that of the vapor.

$$P_{4B} = P_{3B} - \Delta P_{3-4} \quad 2.6$$

$$T_{4B} = T_{3B} - \Delta T_{3-4} \quad 2.7$$

The subscript "3-4" indicates a change; for example, ΔP_{3-4} is equivalent to $P_3 - P_4$. Upon exiting the condenser (4^B), the liquid is heated as it returns to the evaporator CC (5), which is at saturation. The viscous pressure drop in this flow is negligible due to the slow velocity.

$$T_5 = T_{4B} - \Delta T_{4-5} \quad 2.8$$

$$T_5 = T_{SAT}@P_5 \quad 2.9$$

$$P_5 = P_{4B} \quad 2.10$$

The liquid then flows across the evaporator wick towards the vapor channels (6), undergoing a pressure drop and a temperature increase. The liquid here is a metastable superheated liquid, with phase change suppressed by capillary pressure.

$$T_6 = T_5 - \Delta T_{5-6} \quad 2.11$$

$$P_6 = P_5 - \Delta P_{5-6} \quad 2.12$$

Vaporization at the meniscus in the vapor channel results in a capillary pressure rise to the saturation pressure at the local temperature,

$$P_1 = P_5 - \Delta P_{6-1} = P_5 - \Delta P_{evap\ cap} \quad 2.13$$

$$T_6 = T_1 \quad 2.14$$

where $\Delta P_{evap\ cap}$ indicates the capillary pressure at the evaporator wick. It is important to note that with capillary menisci (pressure discontinuities) in both the evaporator and condenser, the vapor pressures are set by the saturation temperatures at (1) and (2), and the liquid pressure is set solely by the CC temperature (5). Thus, if the CC temperature is decreased, the pressures at (3-6) (blue section in Figure 2.2) will decrease and the capillary pressures at the evaporator and condenser (dashed lines in Figure 2.2) will increase.

In contrast to the bottom condenser, the top condenser experiences a lower liquid pressure due to the gravitational pressure head,

$$P_{4T} = P_{4B} - \rho g \Delta h_{T-B} \quad 2.15$$

where Δh_{T-B} represents the height difference between the two condensers. Due to the slow velocity of the flow, the viscous pressure drop in the liquid line is neglected. With equal mass flow in the condensers, the thermal and fluidic relationships between state (3) and (4) are equal. The liquid pressure and temperature immediately after condensation ($3^{\top}$) in the top condenser are therefore as follows:

$$P_{3T} = P_{4T} + \Delta P_{3-4} = P_5 - \rho g \Delta h_{T-B} + \Delta P_{3-4} \qquad 2.16$$

$$T_{3B} = T_{4T} + \Delta T_{3-4} = T_{4B} + \Delta T_{3-4} \qquad 2.17.$$

Combining Equations 2.4, 2.6 and 2.16, the capillary pressure in the top condenser is determined. The difference in the liquid pressures is directly translated into a difference in the condenser capillary pressures. In this example, since the capillary pressure at the bottom condenser is zero, the capillary pressure at the top condenser is the gravitational pressure head. A positive capillary pressure indicates a receding meniscus.

$$\Delta P_{cond\ cap} = P_2 - P_{3T} = P_{3B} - (P_{4B} - \rho g \Delta h_{T-B} + \Delta P_{3-4}) = \rho g \Delta h_{T-B} \qquad 2.18$$

Due to the low liquid pressure, the liquid is thermodynamically superheated in the condenser wick. Through a similar analysis, the capillary pressure at the bottom condenser can be calculated for the inverted case to be as follows:

$$\Delta P_{cond\ cap\ (inverted\ )} = P_2 - P_{3B} = \rho g \Delta h_{T-B} \qquad 2.19.$$

2.2.1 Design Requirements for Functionality

In order for the cycle to function as described, four critical requirements must be met.

1) (Evaporator) The wick must be able to sustain sufficient capillary pressure to drive the circulation and suppress the vaporization of superheated liquid. As the superheat scales with the capillary pressure, both are accomplished with high capillary pressure.
2) (Condenser) The wick must be able to sustain a capillary pressure of at least the maximum gravitational pressure head between the condensers.
3) (Evaporator) Since the temperature at the CC sets the liquid pressures, the CC must be maintained at a sufficiently low temperature to ensure that the liquid pressure does not exceed the vapor pressure at the lowest condenser. A detailed analysis is below (Section 2.2.2).
4) (Condenser) The condensate in the condenser with a receding capillary meniscus is a superheated liquid. Although vapor flashing is suppressed within the wick by capillary pressure, sufficient sub-cooling is required to prevent flashing at the exit of the wick. Flashing will lead to saturated vapor in the liquid line, which will transfer the saturation zone from the CC to the liquid line. Subsequently, the vapor region in the CC will collapse, and liquid pressure control will be lost. A detailed analysis is below (Section 2.2.3).

2.2.2 CC Temperature to Prevent Condenser Flooding

To form a criterion for the maximum temperature allowable in the CC before flooding occurs, the pressure of the CC is related to the pressures in the lowest condenser. Flooding is avoided by preventing the liquid pressure (3) from exceeding the vapor pressure (2), which for the upright orientation, is:

$$P_2 \geq P_{3B} \qquad 2.20.$$

Substituting Equations 2.6 and 2.10 into 2.20, this can be expressed in terms of the CC pressure:

$$P_2 \geq P_5 + \Delta P_{3-4} \qquad 2.21$$

The vapor pressure in the condenser is related to the vapor pressure in the evaporator vapor channels with Equation 2.2. In order to prevent flooding in the bottom condenser, the difference in the pressures between the vapor in the evaporator and the CC must be:

$$P_1 - P_5 \geq \Delta P_{3-4} + \Delta P_{1-2} \qquad 2.22.$$

Since (1) and (5) are at saturation, the pressure difference can be translated to a temperature difference using an approximation of the Clausius-Clapeyron relation. This saturation temperature difference must occur across the thickness of the evaporator, and imposes a critical design requirement.

$$T_1 - T_5 \geq \frac{\Delta P_{3-4} + \Delta P_{1-2}}{\left[\frac{dP}{dT}\right]_{SAT}} \qquad 2.23$$

Through a parallel analysis of the inverted case, the saturation temperature difference required to prevent flooding in the top condenser can be calculated to be the following:

$$T_1 - T_5 \geq \frac{\Delta P_{3-4} + \Delta P_{1-2} + \rho g \Delta h_{T-B}}{\left[\frac{dP}{dT}\right]_{SAT}} \qquad 2.24.$$

Thus, a greater temperature difference is required for the inverted case, in which the height (pressure) difference between the lower condenser and the CC is the greatest. Also, a larger temperature difference will result in a larger capillary pressure in the condensers. While this may allow for a greater safety factor against flooding, the temperature difference cannot be excessively large, or the maximum capillary pressure of the condenser wick will be exceeded. A maximum temperature difference can be calculated for the upright case by analyzing the condition in which the maximum capillary pressure ($\Delta P_{max\ cap}$) is generated in the upper condenser and calculating the corresponding temperature difference between the CC (5) and the vapor (1). Combining Equations 2.2, 2.16 and 2.18, the maximum capillary pressure required at the upper condenser is related to the pressures of the CC and vapor in the evaporator as:

$$\Delta P_{max\ cap} \geq P_2 - P_{3T} = (P_1 - \Delta P_{1-2}) - (P_5 - \rho g \Delta h_{T-B} + \Delta P_{3-4}) \qquad 2.25$$

$$\Delta P_{max\ cap} \geq (P_1 - P_5) - (\Delta P_{1-2} - \rho g \Delta h_{T-B} + \Delta P_{3-4}) \qquad 2.26.$$

Rearranging and translating the saturation pressures to temperatures, the maximum saturation temperature difference is calculated.

$$T_1 - T_5 \leq \frac{\Delta P_{max\ cap} + \Delta P_{1-2} - \rho g \Delta h_{T-B} + \Delta P_{3-4}}{\left[\frac{dP}{dT}\right]_{SAT}} \qquad 2.27$$

A parallel analysis can be performed to determine the maximum saturation temperature difference for the inverted case.

$$T_1 - T_5 \leq \frac{\Delta P_{max\ cap} + \Delta P_{1-2} + \Delta P_{3-4}}{\left[\frac{dP}{dT}\right]_{SAT}} \qquad 2.28$$

Thus, to prevent condenser flooding for both upright and inverted orientations, the temperature difference between the CC and the vapor (vapor channels) must be maintained within the following range.

$$\begin{aligned} \frac{\Delta P_{3-4} + \Delta P_{1-2} + \rho g \Delta h_{T-B}}{\left[\frac{dP}{dT}\right]_{SAT}} &\leq T_1 - T_5 \\ &\leq \frac{\Delta P_{max\ cap} + \Delta P_{1-2} - \rho g \Delta h_{T-B} + \Delta P_{3-4}}{\left[\frac{dP}{dT}\right]_{SAT}} \end{aligned} \qquad 2.29$$

Equation 2.29 sets forth a design requirement that must be met in the evaporator to prevent condenser flooding in the multiple-condenser heat pipe.

2.2.3 Sub-cooling to Prevent Condensate Flashing

To prevent vapor flashing in the condenser, the condensate must be a thermodynamically stable liquid at the exit of the wick. In Figure 2.2, (4) must lie to the left of the saturation curve. A criterion is developed by analyzing state (4) for the upper condenser, which has the most superheated (lowest pressure) condensate. From Equations 2.16 and 2.18, the pressure at the exit of the wick for the upright case is:

$$P_{4T} = P_{3T} - \Delta P_{3-4} = P_2 - \Delta P_{cond\ cap} - \Delta P_{3-4} \qquad 2.30.$$

Also, the sub-cooling required between (2) and (4) can be related to the corresponding pressures.

$$T_2 - T_4 \geq \frac{P_2 - P_{4T}}{\left[\frac{dP}{dT}\right]_{SAT}} \qquad 2.31$$

Using Equation 2.30, the sub-cooling can be expressed in terms of the capillary pressure and viscous loss through the wick.

$$T_2 - T_4 \geq \frac{\Delta P_{cond\ cap} + \Delta P_{3-4}}{\left[\frac{dP}{dT}\right]_{SAT}} \qquad 2.32$$

Thus, for a given capillary pressure, a larger viscous pressure loss will require greater sub-cooling. As the capillary pressure in the condenser is set by the saturation pressures in the evaporator, the required sub-cooling is dependent on the evaporator design. Using Equations 2.2, 2.10, 2.16 and 2.18 the capillary pressure in the condenser can be expressed as

$$\Delta P_{cond\ cap} = P_2 - P_{3T} = (P_1 - \Delta P_{1-2}) - (P_5 - \rho g \Delta h_{3-4} + \Delta P_{3-4}) \qquad 2.33.$$

The required sub-cooling is therefore restated as,

$$T_2 - T_4 \geq \frac{P_1 - P_5 - \Delta P_{1-2} + \rho g \Delta h_{3-4}}{\left[\frac{dP}{dT}\right]_{SAT}} = (T_1 - T_5) - \frac{\Delta P_{1-2} - \rho g \Delta h_{3-4}}{\left[\frac{dP}{dT}\right]_{SAT}} \qquad 2.34 \ .$$

assuming a constant $(dT/dP)_{SAT}$ for the temperature range analyzed. Similarly, the required sub-cooling for the inverted case is:

$$T_2 - T_4 \geq \frac{P_1 - P_5 - \Delta P_{1-2}}{\left[\frac{dP}{dT}\right]_{SAT}} = (T_1 - T_5) - \frac{\Delta P_{1-2}}{\left[\frac{dP}{dT}\right]_{SAT}} \qquad 2.35.$$

It can be seen that the requirement for the upright case is more stringent and should be used as the basis of design.

2.3 Thermal-fluidic Cycle as a CPL

A similar operation of the MCHP can be achieved with a CPL cycle, in which a reservoir takes the place of the evaporator CC as the third location of saturation (Figure 2.3). The reservoir must be heated beyond the temperature of the CC to be saturated, and hence the operating liquid pressures are higher and capillary pressures are lower. Temperature control (heating) of the reservoir is therefore analogous to heating the CC. Thus, the basic requirement for saturation in the reservoir is:

$$T_{RES} > T_5 \qquad 2.36$$

The same requirements apply for heat pipe functionality. Equation *2.29* is restated for the CPL in the upright case as:

$$\frac{\Delta P_{3-4} - \Delta P_{1-2} + \rho g \Delta h_{T-B}}{\left[\frac{dP}{dT}\right]_{SAT}} \leq T_1 - T_{RES} \leq \frac{\Delta P_{max\ cap} + \Delta P_{1-2} - \rho g \Delta h_{T-B} + \Delta P_{3-4}}{\left[\frac{dP}{dT}\right]_{SAT}} \qquad 2.37.$$

Similarly, the requirement for condenser sub-cooling is restated as:

$$T_2 - T_4 \geq \frac{P_1 - P_{RES} - \Delta P_{1-2} + \rho g \Delta h_{3-4}}{\left[\frac{dP}{dT}\right]_{SAT}} = (T_1 - T_{RES}) - \frac{\Delta P_{1-2} - \rho g \Delta h_{3-4}}{\left[\frac{dP}{dT}\right]_{SAT}} \qquad 2.38$$

As the requirements must be met for a particular P_{RES}, improper reservoir temperature control will prevent the requirements from being fulfilled. For example, an excessively high reservoir temperature (pressure) will cause the lower condenser to flood. However, as the reservoir heating decreases the capillary pressures, the CPL cycle offers benefits through the alleviation of the upper limit (of exceeding the maximum capillary pressure in the condenser) in the requirement of Equation *2.37*.

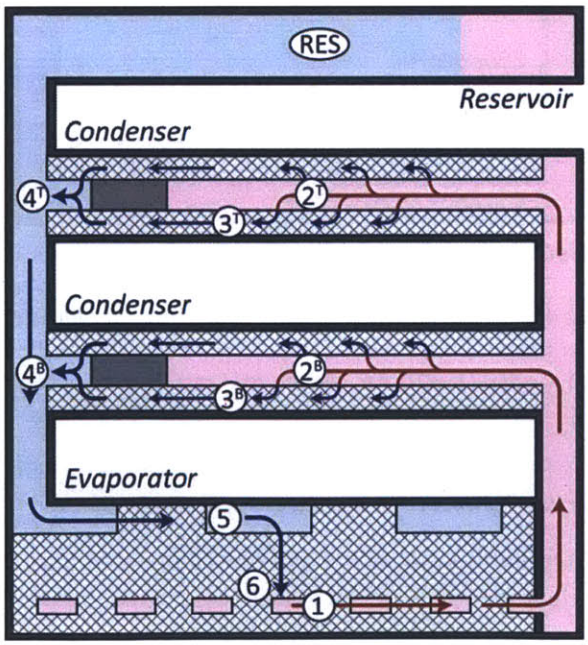

Figure 2.3. Multiple-condenser CPL cycle. In contrast to the LHP cycle, saturation occurs in the reservoir instead of the CC. The circulation remains the same as the LHP cycle as the fluid in the reservoir does not affect the circulation.

2.4 Designing for Low Thermal Resistance

In addition to the above requirements for functionality, since the multiple-condenser heat pipe is developed for a heat sink, designing for low thermal resistance is critical. Figure 2.4 shows the thermal resistance circuit for the main heat transfer path in the heat pipe, with a nodal layout adopted from Figure 2.1. The heat pipe resistance can be separated into three parts: conductive resistance into the evaporator, fluidic losses inside of the heat pipe, and conductive resistance out of the condenser. There are conductive resistances between the evaporator base (B) and vapor channels (1) and between the condensation space (2) and outer surface (S) of the condenser. The fluidic resistance is seen in Figure 2.2 as the saturation temperature drop between (1) and (2) due to the pressure drop (ΔP_{1-2}). It is important to note that the pressure losses that occur after (2) do not affect the thermal resistance of the heat pipe. Although not included within the resistance of the heat pipe, the convective resistance of the fan is dependent on the surface area maintained near the (high) vapor temperature (2); it is thus favorable to maximize the condensation area in the condenser to lower this resistance. Consequently, a flooded condenser results in a higher thermal resistance as the condensation area is decreased.

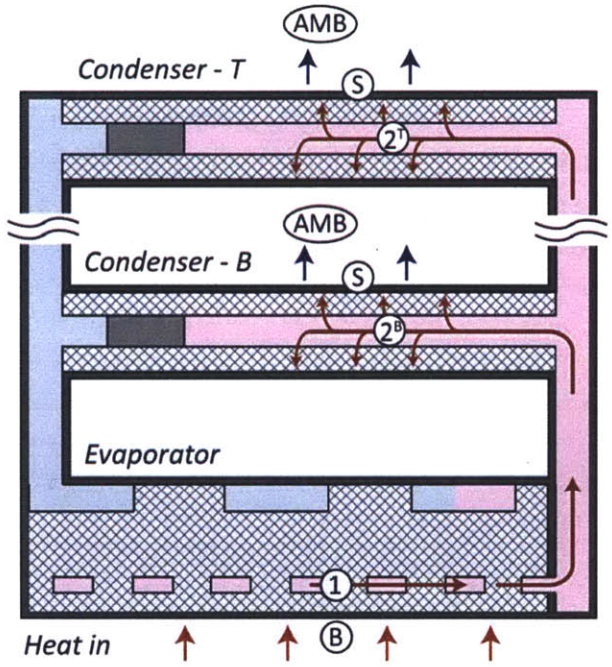

Figure 2.4. Nodal network of the heat transfer path through the heat pipe (heat sink). The heat pipe characteristically has there resistances: conductive resistance in the evaporator (B →1) and condenser (2 →S) and fluidic resistance in the vapor line (1 →2). Air-cooling also results in convective resistance (S →AMB).

2.5 Summary

This chapter details the thermal-fluidic cycle of a novel heat pipe cycle to prevent flooding in a multiple-condenser stack. Flooding degrades the performance of the condenser(s), increasing the thermal resistance. To avoid this, wicks are integrated into the condensers to separate the vapor and liquid phases *via* receding capillary menisci. Two requirements are developed for proper heat pipe operation.

First, maintenance of the receding menisci requires the regulation of vapor and liquid pressures, which in turn requires the temperature of the CC to be held sufficiently below that of the vapor temperature in the evaporator. Second, to prevent vapor flashing at the exit of the condenser wick, the condensate must be a thermodynamically sub-cooled liquid at the exit of the condenser wick. Flashing in the condenser will result in the transfer of the liquid-side location of saturation from the compensation chamber to the condenser, adversely affecting the mechanism of liquid pressure control. Both loop heat pipe and capillary pumped loop cycles can be applied to the multiple condenser layout, with the reservoir replacing the compensation chamber as the location of saturation in a capillary pumped loop. Additionally, to reduce the heat sink thermal resistance, the heat pipe must be designed with minimal conductive resistance in the evaporator and condenser as well as fluidic resistance in the vapor lines. The requirements derived in this chapter are used to evaluate the operating behavior of the MCHP in the following chapter.

(This page intentionally left blank)

3 Analytical Model and Wick Selection

3.1 Overview

This chapter discusses the development of an analytical model to investigate the effect of the wick properties on the operation the ability to meet the requirements of the multiple-condenser heat pipe outlined in Chapter 2. The properties of various sintered metal wicks are evaluated, those for the evaporator and condenser are selected using the results of the model. The selected wicks are then used as the basis of more detailed design analyses of the evaporator and condenser.

3.2 Model Description

LHPs have commonly been modeled using nodal analysis, with the approximation of spatially averaged temperatures and pressures at the nodes [48-52]. Suarte *et al.* developed a closed form solution by separating the analysis for the different operating regimes of the LHP [53]. Several researchers have used nodal analysis to describe the transient behavior in LHPs [54, 55]. Furukawa performed a theoretical design analysis using a spatially averaged nodal model [51]. Due to the simplicity in the formulation and computation, nodal analysis is also used here to understand the operating behavior of the multiple-condenser heat pipe. Since the main novelty of the heat pipe cycle is the formation of a receding meniscus in the condenser wick, this analysis focuses on the vapor and liquid pressure difference at the lowest condenser, which is most susceptible to flooding. It is important to note that the nodal model is used as a preliminary analysis tool for more detailed component (evaporator and condenser) development, not as a tool for predicting the experimental results presented later in Chapters 5 and 6. An accurate prediction requires the consideration of the actual three-dimensional nature of the thermal-fluidic cycle than is not fully captured in the nodal model.

Figure 3.1 shows the nodes used in the analysis of the LHP cycle. While the focus is on a LHP cycle, the results can be applied to understand the CPL cycle as well, since the trends affecting the condenser capillary pressure remain the same. The analysis is simplified with the following assumptions/conditions:

1) Operation is steady state.
2) The CC is always two-phase at the average temperature.
3) Condensation occurs on the entire wick area available for vapor access in the condenser.
4) All condensers function equally and observe equal mass flow rates. Thus, the flow rates in the individual condensers will equal the total mass flow rate divided by the number of condensers.
5) The heat pipe is considered to have two sides – the vapor and liquid sides, separated by the capillary menisci in the evaporator and condenser. In steady state operation, the net mass flow

into the liquid side (or vapor side) is zero, and the capillary pressure at the two wicks prevents the liquid pressure from communicating with that of the vapor.

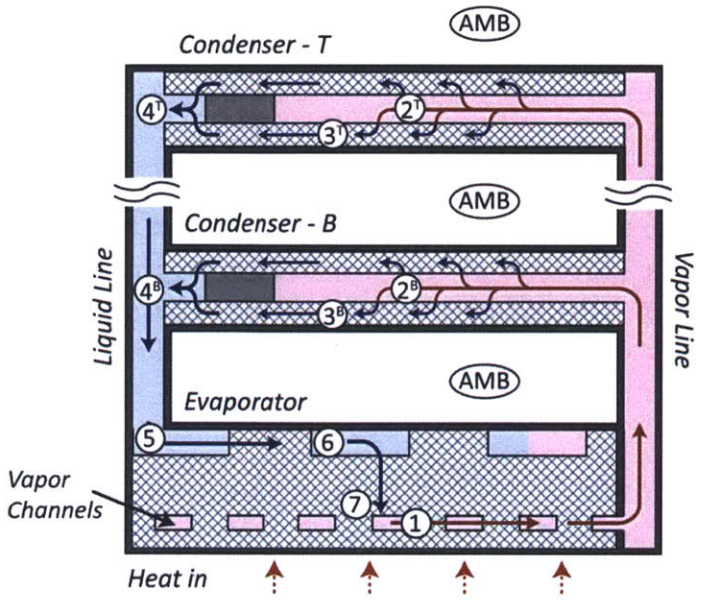

Figure 3.1. Diagram of nodes used in the model. Nodes 7 & 1, and 2 & 3 indicate before and after evaporation and condensation, and are used to calculate the capillary pressure in the evaporator and condenser, respectively. Pink and light blue regions indicate vapor and liquid, respectively. The hatched sections indicate the wicks.

While the modeling of LHPs with non-wicked condensers requires that all temperature and pressure relationships are solved simultaneously, the last assumption greatly simplifies the analysis. Due to the pressure discontinuity (menisci) in the evaporator and condenser, the liquid pressure does not affect the vapor pressure or temperature. As a result, the vapor and liquid pressures can be analyzed separately, using the saturation temperatures in the vapor and liquid sides. The temperatures are therefore solved independently of the liquid pressures, which are solved subsequently using the saturation and pressure drop relations. Calculations were performed with a computational software, MATLAB (Mathworks, Natick, MA, *MATLAB R2011.a*). The code is included in Appendix A.

3.2.1 Temperature Relations

The temperatures in a LHP are related through a series of thermal gradients and the requirement to meet saturation in the evaporator vapor channels (1), condenser (2), and the CC (6). The temperatures at (1) and (2) are related by the saturation pressure drop between the vapor channels and condenser.

$$\Delta T_{1-2} = \frac{\Delta P_{1-2}}{\left[\frac{dP}{dT}\right]_{SAT}} \qquad 3.1$$

where ΔP_{1-2} consists of the viscous and inertial pressure drops associated with the flow through vapor channels (ΔP_{chan}) and vapor lines (ΔP_{v_line}) of square and round cross sections, respectively:

$$\Delta P_{1-2} = \Delta P_{chan} + \Delta P_{v\_line}$$
$$= \left[\frac{1}{2}\rho_v v_{chan}^2 + \frac{1}{2}\rho_v v_{chan\ avg}^2 \left(f_{chan}\frac{L_{chan}}{D_{h\ chan}} + K_{chan}\right)\right] \quad 3.2.$$
$$+ \frac{1}{2}\rho_v v_{v\_line}^2 \left(f_{V\_line}\frac{L_{v\_line}}{D_{h\ v\_line}} + K_{v\_line}\right)$$

where

$$v_{chan} = 2 * v_{chan\ avg} = \frac{\dot{m}}{\rho_v n_{chan} A_{chan}} \quad 3.3$$

and

$$v_{V\_line} = \frac{\dot{m}}{2\rho_v A_{v\_line}} \quad 3.4.$$

The subscripts v, $chan$ and v_line refer to the vapor, vapor channels and vapor line. avg indicates an average value. ρ, v and L refer to the density, velocity and lengths, respectively. D_h and K are the hydraulic diameter and coefficient of pressure loss in a developing flow. The values for K were obtained from [56, 57]. $\dot{m}$, n_{chan} and A are the total mass flow rate, number of vapor channels and cross sectional area of the flow, respectively. f_{chan} and f_{v_line} are the friction factors associated with laminar viscous flow for square and round channels, respectively [56].

$$f_{chan} = \frac{56.9}{Re_{chan}} \quad 3.5$$

$$f_{V\_line} = \frac{64}{Re_{v\_line}} \quad 3.6$$

Re is the Reynolds number, defined as:

$$Re = \frac{\rho v D_h}{\mu} \quad 3.7.$$

where μ is the viscosity of the fluid.

The temperature at (2) is determined by the cooling at the condensers, which consists of the convective cooling of the condensation space and the sub-cooler region. To allocate a large area for condensation, the two regions are modeled as concentric annuli contained by the four vapor and liquid ports at the corners. The geometry is shown with corresponding dimensions in Figure 3.2.

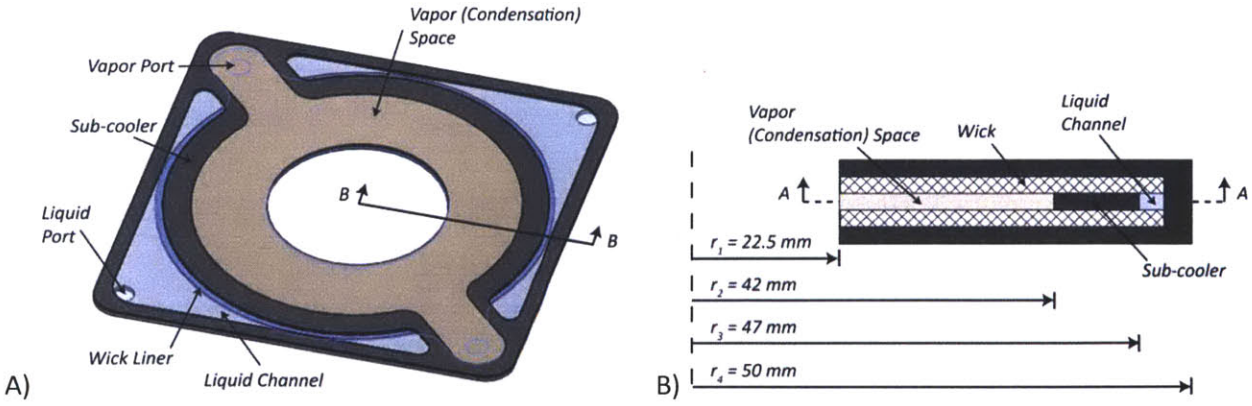

Figure 3.2. Schematic of the condenser geometry used in the modeling, showing cross sectional cuts A) parallel to the condenser surface and B) perpendicular to the condenser surface. The pink and blue regions represent the vapor and liquid space.

The temperatures before and after condensation are equal:

$$T_2 = T_3 \tag{3.8}$$

The latent heat of condensation (h_{fg}) is removed by the convective cooling of the condensation space (A_{cond}) between r_1 and r_2, as well as the heat removal that occurs through the radial conduction from r_2 to r_4. While the condensation space remains isothermal at the condensation temperature (T_2), a thermal gradient is present between r_2 and r_4, and is thus modeled as a radial fin (Q_{fin}).

$$\dot{m}h_{fg} = hA_{cond}\,(T_2 - T_{AMB}) + Q_{fin} \tag{3.9}$$

where

$$A_{cond} = \pi({r_2}^2 - r_1^2) \tag{3.10.}$$

h is the convective heat transfer coefficient that acts on the surfaces of the condenser and evaporator. This radial, axial-symmetric analysis does not include the heat transfer at the corners. The conductive resistance between (2) and the outer surface of the condenser is approximated as negligible due to the small thickness of the wick and the condenser case/frame. The heat transferred from the fin is calculated through the integration of a differential energy equation along the radial length of the fin, using the boundary conditions of a prescribed base temperature (T_2) and an adiabatic fin tip [58]:

$$Q_{fin} = k_{fin}(4\pi r_2 t)(T_2 - T_{AMB})\beta[C_2K_1(\beta r_2) - C_1I_1(\beta r_2)] \tag{3.11}$$

where t_{fin}, k_{fin} and β are respectively the thickness and effective thermal conductivity of the fin and the non-dimensional number analogous to the Biot number, defined as:

$$\beta = \frac{h}{t_{fin}\,k_{fin}} \tag{3.12.}$$

The effective conductivity is estimated as the spatial average of the conductivities of the wick and condenser case at r_2,

$$k_{fin} = \frac{t_{c\_wick}\, k_{c\_wick} + t_{c\_case}\, k_{c\_case}}{t_{fin}} \qquad 3.13$$

where the subscripts *c_wick* and *c_case* refer to the condenser wick and case, respectively. To simplify the calculation, this effective conductivity is used for the entire fin length. The coefficients of Equation 3.11 are defined as the following:

$$C_1 = \frac{K_1(\beta r_4)}{I_0(\beta r_2)K_1(\beta r_4) + I_1(\beta r_4)K_0(\beta r_2)} \qquad 3.14$$

and

$$C_2 = \frac{I_1(\beta r_4)}{I_0(\beta r_2)K_1(\beta r_4) + I_1(\beta r_4)K_0(\beta r_2)} \qquad 3.15$$

where I_0 and K_0 are the zero-order modified Bessel functions of the first and second kinds, and I_1 and K_1 are the first-order modified Bessel functions. The functions can be found tabulated in [58]. As a simplification, the heating of the condensate between (2) and (4) is not included in the calculation of (Q_{fin}), since conduction plays a significantly larger role in the heat transfer. This comparison can be approximated as a ratio of the conductive and capacitive resistances

$$\frac{\left(\frac{\ln\left[\frac{r_4}{r_2}\right]}{2\pi k_{fin}\, t_{fin}}\right)}{\left(\frac{1}{\dot{m}/n_{cond}\, C_p}\right)} \ll 1 \qquad 3.16$$

where C_P is the specific heat of the liquid and n_{cond} is the number of condensers. Using the same analysis, the temperature at (4) is calculated as

$$T_4 = (T_2 - T_{AMB})[C_1 I_0(\beta r_3) - C_2 K_0(\beta r_3)] + T_{AMB} \qquad 3.17.$$

The temperature drop between (4) and (5) in the convectively cooled liquid tube is calculated by integrating a differential energy equation along the half-length of the tube [58].

$$T_5 = T_{AMB} + (T_4 - T_{AMB})e^{-\frac{L_{l\_line}/2\, h_{l\_line}\, P}{\dot{m}_{avg}\, C_P}} \qquad 3.18$$

$L/2$ and P are the half-length and perimeter, where the subscript *l_line* indicates the liquid line. Since the condensers are located at staggered heights along the liquid line, the half-length is used as the average travel distance of the liquid flow. $\dot{m}_{avg}$ is the average (half of the total) mass flow rate in each liquid tube,

$$\dot{m}_{avg} = \frac{\dot{m}}{4} \qquad 3.19.$$

In the evaporator, the temperatures at (5), (6) and (7) are related to the ambient temperature by performing the thermal analog of Kirchhoff's law at (6),

$$Q_{leak} = \dot{m}C_P(T_7 - T_6) + \frac{T_7 - T_6}{R_{6-7}} = hA_{evap\_conv}(T_6 - T_{AMB}) + \dot{m}C_P(T_6 - T_5) \qquad 3.20$$

where A_{evap_conv} is the convectively cooled area of the evaporator. The heat transfer across the evaporator, from the vapor channels to the CC, is defined as the heat leak, Q_{leak}. R_{6-7} is the effective conductive resistance between (6) and (7), consisting of the conductive resistances of the evaporator wick and the case in parallel.

$$R_{6-7} = \frac{1}{\frac{k_{e\_wick}A_{e\_wick}}{t_{e\_wick}} + \frac{k_{e\_case}A_{e\_case}}{t_{e\_case}}} \qquad 3.21$$

The subscripts *e_wick* and *e_case* indicate the evaporator wick and case, respectively. The heating of the liquid between (6) and (7) may have little contribution to the heat leak, and is neglected when:

$$\frac{R_{6-7}}{\left(\frac{1}{\dot{m}C_P}\right)} < 0.1 \qquad 3.22$$

Additionally, the temperatures before and after evaporation are equal:

$$T_7 = T_1 \qquad 3.23$$

Lastly, the applied heat load is equated to the cumulative heat losses of the cycle:

$$Q_{load} = hA_{cond}(T_2 - T_{AMB}) + Q_{fin} + Q_{leak} \qquad 3.24.$$

By solving the eight Equations of 3.1, 3.8, 3.9, 3.17, 3.18, 3.20, 3.23, and 3.24 simultaneously for a given heat load, the seven temperatures and the mass flow rate are obtained.

3.2.2 Pressure Relations

The pressure drop relations for the vapor are necessary for calculating the vapor temperatures, and are described above. Those for the liquid flow between (3) and (7) consist of viscous pressure drops and gravitational pressure differences. The pressure drop through the condenser wick, from (3) to (4), is calculated using the Darcy equation in the radial direction assuming an axial-symmetric flow.

$$\frac{dP}{dr} = -\frac{\mu_l}{\kappa_{c\_wick}} v_r \qquad 3.25$$

where κ the wick permeability and v_r the radial velocity of the liquid flow in the wick. The subscript l indicates liquid properties. The analysis is separated into two parts: 1) between r_1 and r_2, with a radially changing mass flow rate due to the condensation, and 2) between r_2 and r_3, with a constant mass flow rate. The radial velocity in the wick between r_1 and r_2 ($v_{r_1-r_2}$) is calculated using mass conservation and a uniform mass influx (m''_{cond}) from condensation:

$$v_{r_1-r_2} 2\pi r t_{c\_wick} = \frac{m''_{cond}}{\rho}\pi(r^2 - r_1^2) \qquad 3.26.$$

Each condenser has two wicks, which cover the inner surfaces of the top and bottom sides. The condensing mass flux per condenser wick is therefore related to the total mass flow rate as:

$$m''_{cond} = \frac{\dot{m}}{2n_{cond}\, A_{cond}} \qquad 3.27.$$

Similarly, the radial velocity between r_2 and r_3 ($v_{r_2-r_3}$) is calculated as:

$$v_{r_2-r_3} 2\pi r t_{c\_wick} = \frac{m''_{cond}}{\rho}\pi({r_2}^2 - r_1^2) \qquad 3.28.$$

Using Equation 3.26 and 3.28 in Equation 3.25, the pressure drop between (3) and (4) is solved as:

$$\Delta P_{3-4} = \frac{m''_{cond}\ \mu_l}{2\pi\rho t_{c\_wick}\ \kappa_{c\_wick}}\left[\frac{1}{2} - \frac{r_1^2}{{r_2}^2 - r_1^2}\ln\left(\frac{r_2}{r_1}\right) + \ln\left(\frac{r_3}{r_2}\right)\right] \qquad 3.29.$$

The pressure drop through the liquid return line consists of the viscous pressure drop associated with a laminar flow through a tube and the gravitational pressure head,

$$\Delta P_{4-5} = \frac{1}{2}\rho_l v_{l\_line}^2\left(f_{L\_line}\frac{L_{l\_line}}{D_{l\_line}} + K_{l\_line}\right) + \rho_l g L_{l\_line} \qquad 3.30.$$

f_{l_line} is defined as

$$f_{l\_line} = \frac{64}{Re_{l\_line}} \qquad 3.31$$

where Re_{l_line} is the Reynolds number associated with the average mass flow rate in the liquid line calculated from Equation 3.19 [56]. Negligible pressure drop occurs as the liquid exits the liquid line (5) and enters the evaporator CC (6).

$$P_5 = P_6 \qquad 3.32$$

The viscous pressure drop across the evaporator wick is calculated using the Darcy equation. The wick is modeled as planar, and the three-dimensional flow pattern near the vapor channels is not included in the analysis.

$$\Delta P_{6-7} = \frac{\mu_l \, t_{e\_wick} \, \dot{m}}{\kappa_{e\_wick} \, A_{e\_wick} \, \rho_l} \qquad 3.33$$

The vapor pressures in the evaporator (1) and condenser (2) are calculated as the saturation pressures of the corresponding temperatures. The saturation pressure is similarly obtained for the CC (6). The CC pressure is then used to calculate the pressures at (3), (4), (5) and (7) using Equations 3.29, 3.30, 3.32 and 3.33. Finally, the capillary pressures at the evaporator and condenser are calculated as:

$$\Delta P_{evap\ cap} = P_1 - P_7 \qquad 3.34$$

and

$$\Delta P_{cond\ cap} = P_2 - P_3 \qquad 3.35.$$

3.3 Results

The model was used to investigate the effects of the thermal conductivity and permeability of the evaporator and condenser wicks on the operation of the heat pipe. Specifically, the effects on the capillary pressures and sub-cooling were investigated as they relate to the requirements of Equations 2.29 and 2.35. The range of thermal conductivities and permeabilities was selected as those feasible with sintered metal wicks. Both upright and inverted cases were considered; the condenser capillary pressure was analyzed in each case for the lowest condenser. Key dimensions are shown in Table 3.1 and Figure 3.2B; a full tabulation of dimensions is included in Appendix B. The properties of water were taken at the local temperatures of the cycle. The ambient air temperature was fixed at 30 °C and a heat transfer coefficient of 100 W/m^2-K was used for the heat transfer surfaces.

Table 3.1. Key dimensions of the modeled heat pipe

	Dimension (mm)
Footprint Area (Evap. & Cond.)	*101.6 x 101.6*
CC Height	0
Condenser Height - B	*0.5*
Condenser Height - T	*90*
Sub-cooler Length	*5*
Evap. Wick Thickness	*4*
Cond. Wick Thickness	*0.5*

3.3.1 General Characteristics

Following the design goals outlined in Chapter 1, the number of condensers was determined by the requirement to remove 1000 W at a vapor temperature of approximately 80 °C and an ambient air temperature of 30 °C. This criterion was met with 14 condensers. The number of condensers is dependent on the geometry of the condensers and the level of convective cooling, and largely independent of the parameters varied in this study. Figure 3.3 shows the vapor temperature in the evaporator plotted against applied heat load for different wick properties. The linear behavior of Figure

3.3 is due to the higher heat pipe temperatures required for the removal of higher heat loads at a given convective heat transfer coefficient through Equations 3.9 and 3.11.

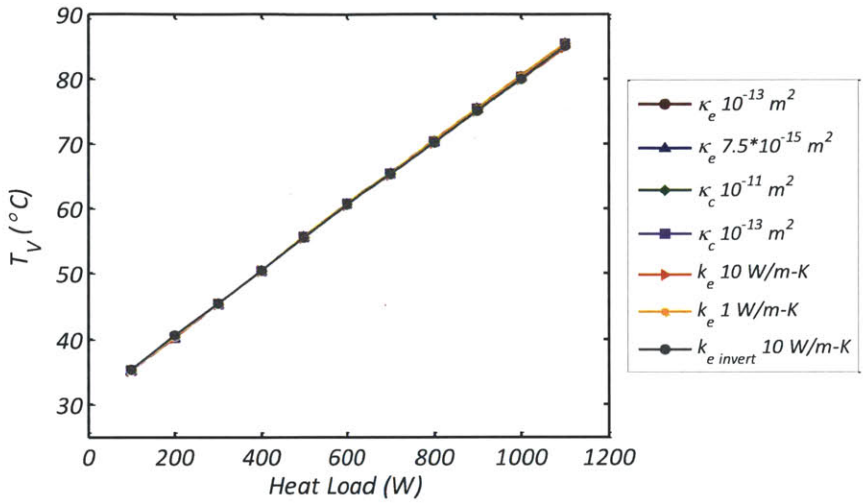

Figure 3.3. Vapor temperature at (1) plotted against heat load, for various wick properties and an ambient air temperature of 30 °C. The subscripts "e" and "c" refer to the evaporator and condenser, and "invert" refers to the inverted case.

Figure 3.4 and Figure 3.5 show the temperatures and pressures of the heat pipe cycle, plotted against the nodal positions and the saturation curve, respectively. Both upright and inverted orientations are shown for operation at 1000 W. The plots follow the circulation through the lowest condenser. It can be seen that a negligible temperature drop occurs between the evaporator (1) and condenser (2), evidencing the high effective thermal conductivity of LHPs. The largest temperature drop of the cycle occurs across the sub-cooler, between (3) and (4). This cooling ensures that the condensate is a thermodynamically sub-cooled liquid at the exit of the condenser wick, meeting the requirement of Equation 2.35. For the modeled conditions, the inertial and viscous pressure losses of the cycle are small; the main pressure drop occurs due to the capillary pressure differential at the condenser (2-3). As a result, much of the driving pressure generated at the evaporator wick is used to establish the capillary pressure at the condenser. A sufficient capillary pressure is present in the condenser to prevent flooding that occurs from the liquid pressure (3) exceeding the vapor pressure (2), for both upright and inverted cases. This indicates that the requirement of Equation 2.29 is met. It must be noted, however, that the capillary pressure at the condenser is highly dependent on the wick properties and heat load, as will be described in the following sections. Nonetheless, the trends illustrated in Figure 3.4 and Figure 3.5 show that the integration of a wick in the condenser can have a substantial influence on the heat pipe pressures.

The effect of orientation (inversion) can also be seen in Figure 3.4 and Figure 3.5. Inversion only affects the liquid pressures through a gravitational pressure head, which is seen in the upwards shift of the pressures at (3) and (4). Due to the vapor-liquid pressure separation, the vapor pressures (and temperatures) are unaffected. As a result, the thermal performance is also unaffected, and the temperatures of the cycle are equal for both upright and inverted cases.

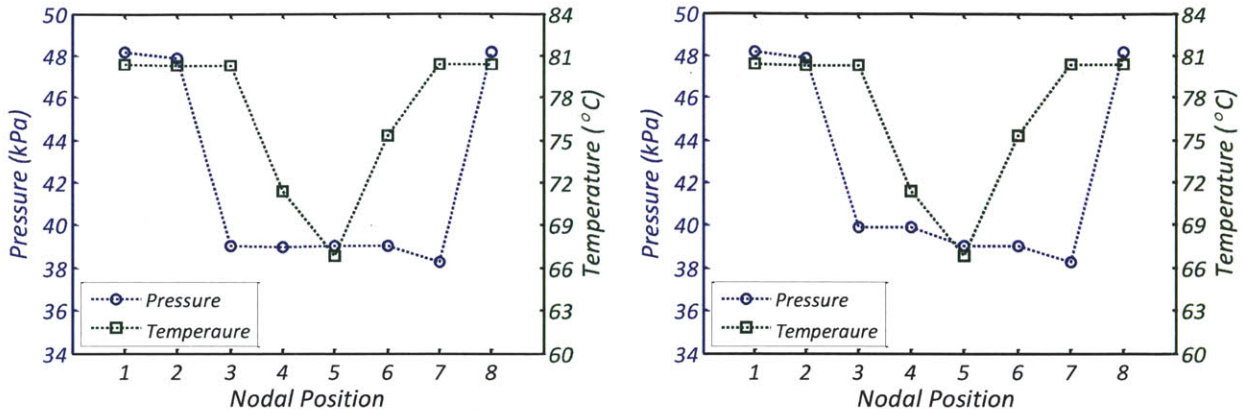

Figure 3.4. Temperatures and pressures of the heat pipe cycle, plotted against nodal position, for the A) upright and B) inverted cases. Position 8 is equivalent to position 1. Modeled conditions: 1000 W, k_{e_wick}=2 W/m-K, $\kappa_{e\_wick}=10^{-13}$ m^2, k_{c_wick}=15 W/m-K, $\kappa_{c\_wick}=10^{-11}$ m^2.

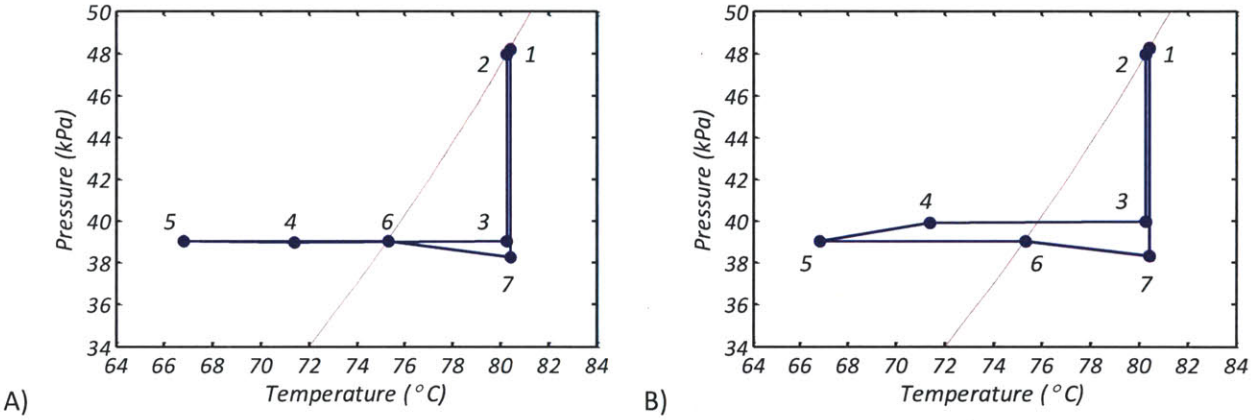

Figure 3.5. Temperatures and pressures of the heat pipe cycle, plotted against the saturation curve, for the A) upright and B) inverted cases. The nodes are annotated. Modeled conditions: 1000 W, k_{e_wick}=2 W/m-K, $\kappa_{e\_wick}=10^{-13}$ m^2, k_{c_wick}=15 W/m-K, $\kappa_{c\_wick}=10^{-11}$ m^2.

3.3.2 Effect of the Evaporator Wick Thermal Conductivity

The thermal conductivity of the evaporator wick influences the saturation temperature of the CC and therefore affects the liquid pressures. As a result, changes in the wick conductivity are reflected in the condenser capillary pressure. Figure 3.6 shows capillary pressure of the lowest condenser plotted against the heat load and thermal conductivity of the evaporator wick. As defined in Equation 2.35., a positive capillary pressure indicates a receding meniscus. Two trends can be seen: an increase in the capillary pressure through 1) a decrease in the thermal conductivity, and 2) an increase in the heat load.

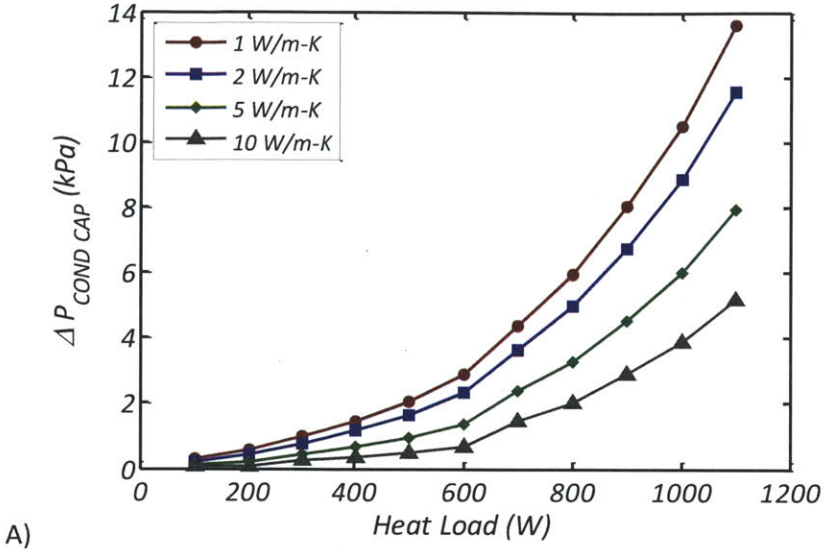

Figure 3.6. Capillary pressure at the lowest condenser, plotted against head load for different evaporator wick thermal conductivities, for A) upright and B) inverted orientations. Modeled conditions: $\kappa_{e\_wick}=10^{-13}$ m^2, $k_{c\_wick}=15$ W/m-K, $\kappa_{c\_wick}=10^{-11}$ m^2.

A lower thermal conductivity results in a higher thermal resistance to the heat leak across the evaporator, resulting in a greater separation of the CC and vapor temperatures. The heat leak transfers heat from the vapor channels to the ambient air, through the CC. Since the CC and vapor temperatures are separated by the wick thermal resistance, increasing this resistance causes the temperature difference to increase. This increase is reflected a larger saturation pressure difference between the vapor and CC, increasing the condenser capillary pressure.

Similarly, the increase in vapor temperature from an increased heat load also results in a greater temperature difference across the wick as the heat leak increases. Furthermore, the condenser capillary pressure increases more rapidly at higher heat loads due to the characteristic shape of the saturation curve of water. Higher temperatures allow for a greater difference in saturation pressure for a given temperature difference. This can be seen mathematically as $\left(\frac{dP}{dT}\right)_{sat}$ increases with temperature. Consequently, the observed increase in the condenser capillary pressure with heat load is two-fold: 1) the saturation temperature difference between the vapor channels and CC increases with higher vapor temperature, and 2) this temperature difference results in a greater pressure difference at the higher temperatures.

Figure 3.6 shows that in the upright orientation, the condenser capillary pressure approaches zero at 100 W. Flooding will be avoided for all heat loads greater than 100 W, and this threshold is roughly independent of the wick thermal conductivity. Near 100 W, the temperature difference between the CC and vapor is more sensitive to the effect of the low vapor temperatures than the wick conductivity. In the inverted orientation, the onset of flooding occurs at noticeably higher heat loads, as the capillary pressure of the lowest condenser is lower than that of the upright case by approximately the gravitational pressure head (85 mm) between the condensers. The onset of flooding (hereon "threshold heat load") in the inverted case is dictated by both vapor temperature (heat load) and wick thermal conductivity. Lower wick conductivities allow for a lower threshold heat load and a wider operating range with un-flooded condensers. However, little difference is seen between 1 and 2 W/m-K as the low vapor temperature at the threshold heat load becomes the limiting factor in forming the capillary pressure.

Due to the increase in capillary pressure with increasing heat load, the selection of an evaporator wick that prevents condenser flooding at low heat loads results in a substantially higher capillary pressure at higher heat loads. As a consequence, the condenser wick must be able to supply a capillary pressure that is significantly higher than the gravitational pressure difference between the condensers in order to ensure stable condenser operation for a wide range of heat loads. Alternatively, a CPL cycle can be used with a dynamically changing reservoir temperature so that the saturation temperature difference between the vapor and reservoir does to result in a large saturation pressure difference.

3.3.3 Effect of the Evaporator Wick Permeability

Although the permeability of the evaporator wick does not affect the capillary pressure in the condenser, it has a direct effect on the pressure drop of the cycle and therefore capillary pressure requirement in the evaporator. Figure 3.7 shows the viscous pressure drop through the evaporator wick, plotted against the heat load for different wick permeabilities. Two trends are observed: the pressure drop increases with 1) a decrease in the permeability and 2) an increase in heat load. Due to the inverse relationship between the pressure drop and the permeability (Equation 3.33), the pressure drop rapidly increases with decreasing permeability. Although a substantial increase in pressure drop occurs between 10^{-14} and $5*10^{-14}$ m^2, wicks with lower permeabilities can still be used if the required capillary pressure for circulation can be supplied. The heat load, in contrast, increases the pressure drop primarily through the mass flow rate. However, as the higher temperatures result in substantially lower

liquid viscosities, the increase in pressure drop is less at high heat loads. This is seen in Figure 3.7 through the decrease in slope at high heat loads.

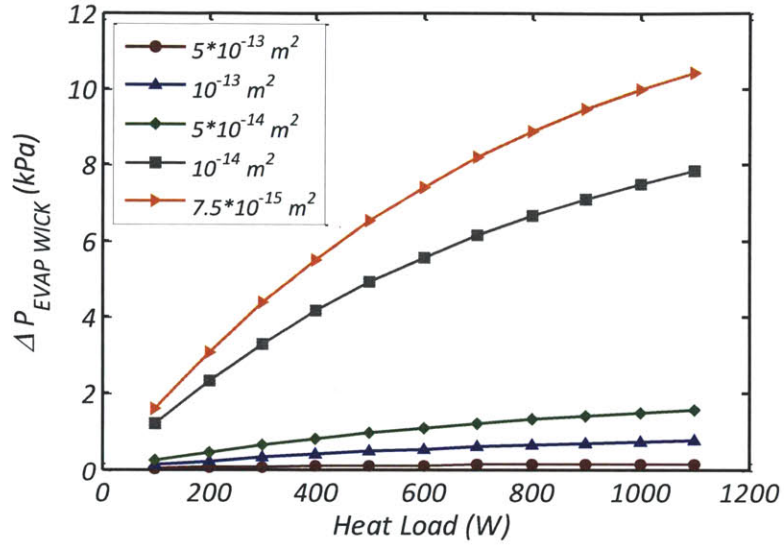

Figure 3.7. Viscous pressure loss through the evaporator wick, plotted against heat load for different wick permeabilities. Modeled conditions: upright, k_{e_wick}=2 W/m-K, k_{c_wick}=15 W/m-K, κ_{c_wick}=10^{-11} m^2.

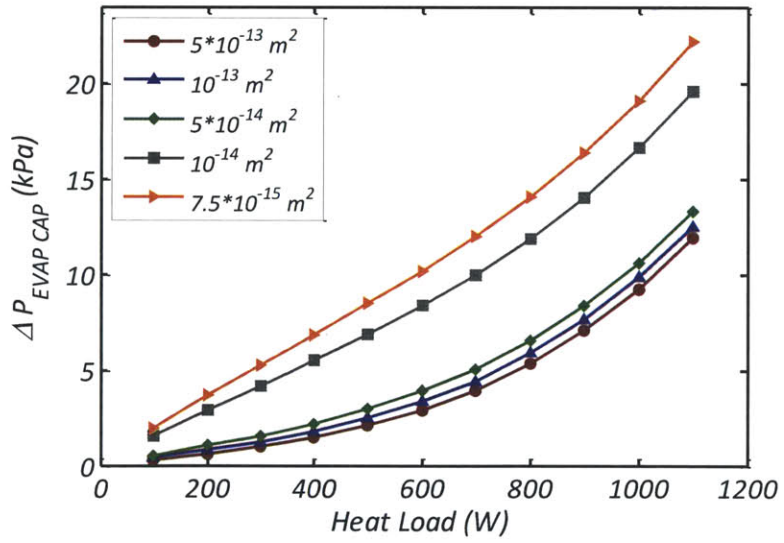

Figure 3.8. Capillary pressure at the evaporator wick, plotted against heat load for different wick permeabilities. Modeled conditions: upright, k_{e_wick}=2 W/m-K, k_{c_wick}=15 W/m-K, κ_{c_wick}=10^{-11} m^2.

Figure 3.8 shows the effect of the permeability and heat load on the evaporator capillary pressure. The capillary pressure required at the evaporator at the higher permeabilities (>5*10^{-14} m^2) is similar to the capillary pressure at the condenser (Figure 3.6), as the latter dominates the other pressure drops of the circulation. Lower permeabilities, however, result in a significantly greater viscous pressure drop in the evaporator. This effect is seen Figure 3.8 as the increase in capillary pressure is greater at low heat

loads. This initial increase in capillary pressure with an increase in heat load is due to the pressure drop across the evaporator wick. As the heat load is increased further, the capillary pressure in the condenser begins to dominate. For a permeability of $7.5*10^{-15}$ m^2, the transition between the two regimes can be seen in the inflection that occurs at 600 – 700 W.

3.3.4 Effect of the Condenser Wick Permeability

The permeability of the condenser wick determines the viscous pressure drop through the wick and affects the capillary pressure in the condenser. Figure 3.9 shows the pressure drop through the condenser wick, plotted against the heat load for different condenser wick permeabilities. As the underlying relationships between the permeability and heat load and the pressure drop are the same as for the evaporator wick, the trends in Figure 3.7 and Figure 3.9 are identical. Figure 3.10 shows the capillary pressure at the lowest condenser, plotted against the heat load for different condenser wick permeabilities. It can be seen that the capillary pressure decreases as the permeability decreases. For a given CC pressure, an increase in the pressure drop through the wick increases the liquid pressure at the condensation interface through Equation 2.16. For low permeabilities ($<2*10^{-13}$ m^2), this initially causes an increasingly negative capillary pressure (advancing meniscus) as the heat load is increased. At lower heat loads and temperatures, the viscous pressure drop in the condenser is greater than the saturation pressure difference between the CC and vapor, and leads to a negative capillary pressure. As the heat load is increased, the increase in the former dominates that of the latter, causing the capillary pressure to decrease further. The capillary pressure begins to increase when the latter begins to dominate due to higher vapor temperature.

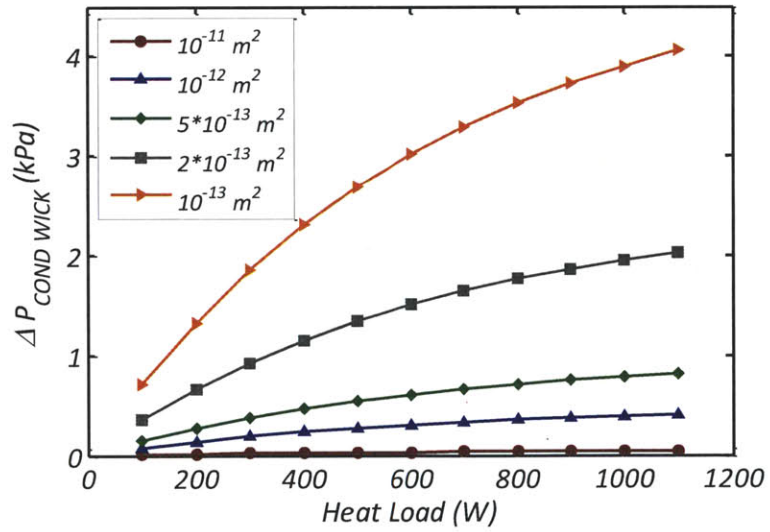

Figure 3.9. Pressure loss through the condenser wick, plotted against heat load for different condenser wick permeabilities. Modeled conditions: upright, k_{e_wick}=2 W/m-K, $\kappa_{e\_wick}=10^{-13}$ m^2, k_{c_wick}=15 W/m-K.

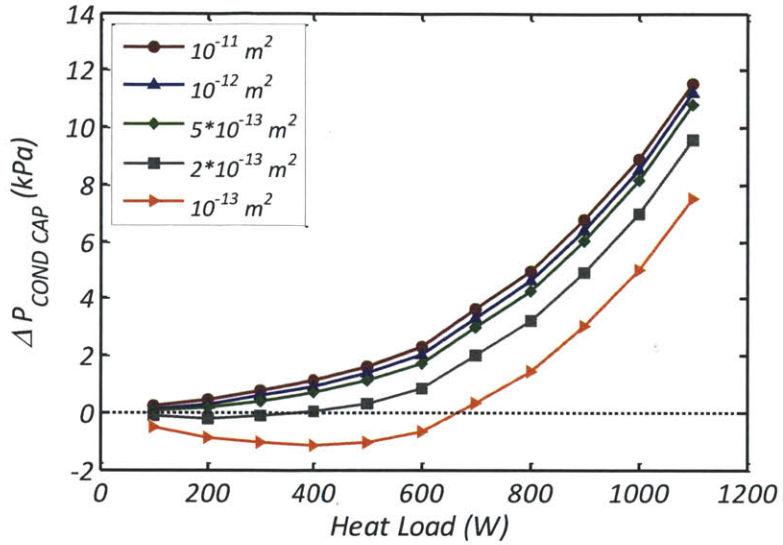

Figure 3.10. Capillary pressure at the lowest condenser, plotted against heat load for different condenser wick permeabilities. Modeled conditions: upright, k_{e_wick}=2 W/m-K, κ_{e_wick}=10^{-13} m^2, k_{c_wick}=15 W/m-K.

3.3.5 Effect of the Condenser Wick Thermal Conductivity

The thermal conductivity of the condenser wick affects the effective thermal conductivity of the sub-cooling section of the condenser and in turn affects the temperature of the condensate leaving the condenser Figure 3.11 shows the degree of sub-cooling for different wick thermal conductivities, plotted against the sub-cooler length. To quantify the sub-cooling, a non-dimensionalized temperature, Φ, is used. Φ is defined as:

$$\Phi = \frac{T_4 - T_{AMB}}{T_2 - T_{AMB}} \qquad 3.36$$

The actual temperature is also shown on the right axis, for the case when the vapor and ambient temperatures are 80 °C and 30 °C, respectively. Figure 3.11 shows that due to the high convective heat transfer coefficient and low ambient temperatures, significant sub-cooling can be achieved for both thermal conductivities. Consequently, there is flexibility in the selecting a condenser wick for sufficient sub-cooling, and the length of the sub-cooler can be designed accordingly to maximize the condensation area.

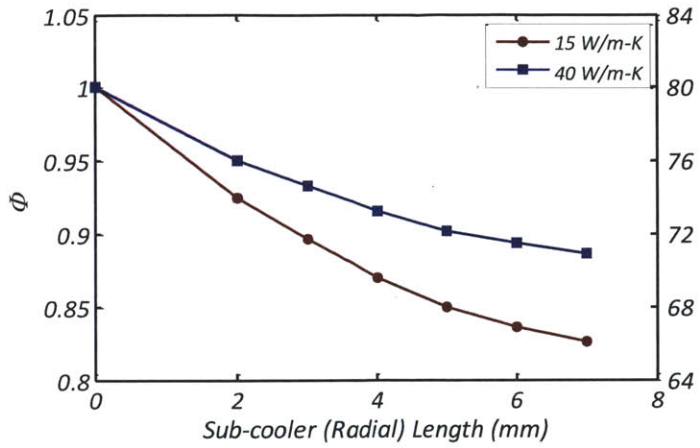

Figure 3.11. Sub-cooling plotted as a function of the sub-cooler length, for different thermal conductivities of the condenser wick. Two y-axes are shown, with ϕ, a non-dimensional number, and the corresponding temperature when the vapor temperature in the condenser is 80 °C and the ambient temperature is 30 °C.

3.4 Wick Selection

The results of the model were used to select the evaporator and condenser wicks. Various sintered metal wicks were fabricated and measured for thermal conductivity, permeability and capillary pressure. The properties were compared to the model results and the wicks were selected on the basis of their ability to maintain a wide range of operation (heat load) with a receding capillary pressure in the lowest condenser and sufficient sub-cooling.

3.4.1 Wick Fabrication and Characterization

Fabrication was focused on two types of wicks: coarse, high permeability wicks for the condenser, and fine, high capillary pressure wicks for the evaporator. All wicks were fabricated by loose-sintering commercially available metal powders in an atmosphere-controlled, 150 mm diameter tube furnace (Lindberg-Blue/Thermo Fisher Scientific, Waltham, MA, *HTF55667C*). Care was taken to remove and prevent oxidation, which inhibits sintering. The furnace tube was flushed with nitrogen gas to displace the oxygen prior to heating; flushing was performed by flowing a volume of nitrogen at least 10 times the volume of the tube. The temperature profile for the heating process is shown in Figure 3.12 and consists of three phases: heating at 600 °C/hour, sintering, and cooling. The sintering time is defined for this study as the dwell time at the peak temperature. The cooling rate was limited by the heat transfer from the furnace; the furnace was turned off for the cooling. All heating was performed in a reducing atmosphere (5% H_2, 95% N_2, at 3 L/min) to remove the existing surface oxides. The reducing gas flow was continued through the cooling process until the temperature decreased to approximately 150 °C, at which time an inert gas flow (100% N_2) was employed for the remainder of the cooling process. This was done to conserve the reducing gas. Sintered wicks were fabricated using copper, nickel, stainless steel, and Monel 400. The sintering temperatures were differed depending on the material.

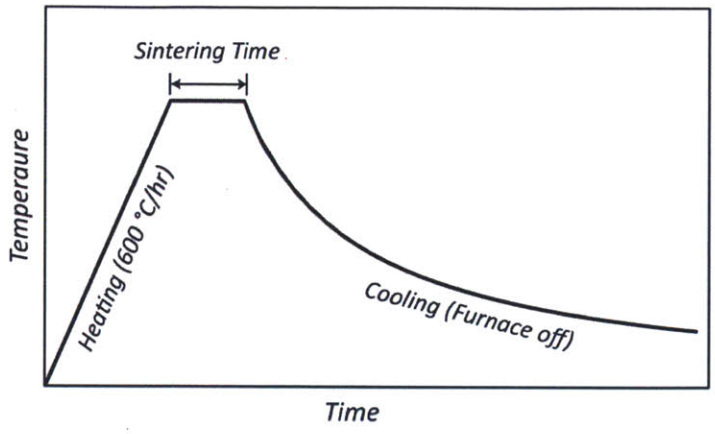

Figure 3.12. Temperature profile for sintering, showing the three phases: heating, sintering and cooling. The sintering time is defined as the dwell time at the peak temperature.

The thermal conductivity was measured using a laser-flash machine (Netzsch, Selb, Germany, *LFA 457*). The process uses a laser to temporarily irradiate one side of the wick sample, which is fabricated as a 12.5 mm diameter, 1-2 mm thick puck. The transient thermal response is determined optically from the other side of the puck by an infrared detector to measure the thermal diffusivity. The volume-averaged specific heat and density are used to calculate the thermal conductivity from the measurement.

Figure 3.13. Wick samples. A) shows a sintered puck (copper powder) used in the laser-flash machine, with a diameter of 12.7 mm. B) shows a plug of wick (copper powder) sintered in a copper tube with an outer diameter of 6.35 mm.

The permeability and capillary pressure were measured using a setup shown schematically in Figure 3.14. A pressurized tank is used to drive the flow of liquid water through a pressure regulator, flow meter (Alicat Scientific, Tuscon, AZ, *L-5CCM-D*) and finally a sample of wick fabricated into 6.35 mm (outer diameter) tube. A thermocouple (Omega Engineering, *TMQSS-125U-2*) and a leg of a differential pressure transducer (Honeywell, Morristown, NJ, *FDW1AT*) are connected to the flow path between the sample and the flow meter. The other leg of the pressure transducer is open to the atmosphere, where the water is expelled after flowing through the sample.

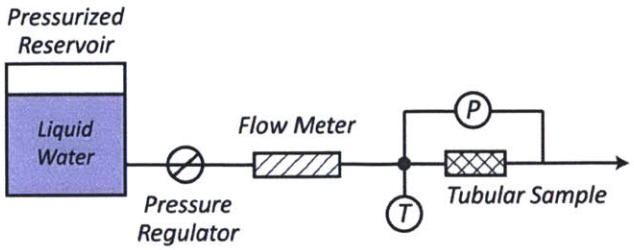

Figure 3.14. Setup for measuring the permeability and capillary pressure of wick samples.

The permeability (κ) was calculated by using Darcy's equation with the measured pressure differential across the wick and the corresponding liquid flow rate

$$\kappa = \frac{\mu_l \, L_{wick} \, \dot{m}}{A_{wick} \, \rho_l \, \Delta P} \qquad 3.37$$

where L_{wick}, A_{wick}, $\dot{m}$ and ΔP are the length and cross sectional area of the wick, the mass flow rate of the liquid and pressure drop, respectively.

The capillary pressure of the receding meniscus was measured by first introducing a pocket of air in the flow path, between the flow meter and the wick sample, which was saturated with liquid. The process is shown in Figure 3.15. The pressure at the regulator was then increased, inducing a slow flow to move the air pocket towards the wick (A). When the air pocket contacted the wick, an air-liquid meniscus was formed, which stopped the flow *via* capillary pressure (B). The regulator pressure was gradually increased until the air pocket was forced through the wick and a flow rate was measured (C). The regulator pressure at breakthrough was determined to be the capillary pressure. It is important to note that with this measurement procedure, the air pocket can be stopped anywhere inside of the wick; *i.e.*, the greatest capillary pressure may be measured with the air pocket halfway into the wick.

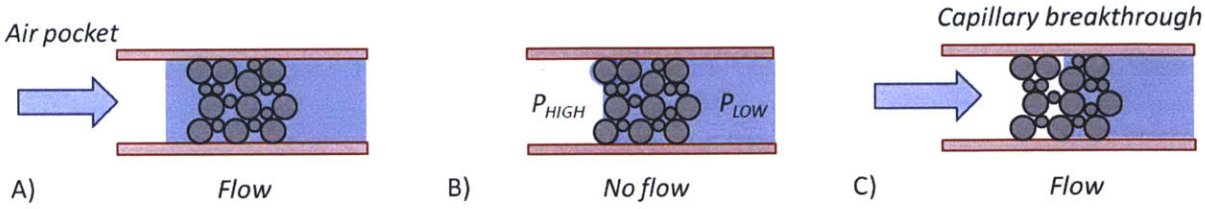

Figure 3.15. Procedure for measuring the receding capillary pressure. A) An air pocket is first transported to the wick plug by a slow flow. B) A capillary meniscus is formed between the air pocket and the wick, and the capillary pressure stops the flow. C) As the pressure at the air pocket is increased, the maximum capillary pressure is exceeded and the flow resumes.

The procedure for measuring the capillary pressure of the advancing meniscus is shown in Figure 3.16. The wick sample was first saturated with liquid (A). A liquid-air meniscus was formed at the open, atmospheric end of the wick and the flow was stopped by the capillary pressure (B). The regulator pressure was then increased until the liquid was forced out of the wick and a flow rate was measured (C). The pressure at the onset of the flow was determined to be the capillary pressure. Since the advancing capillary pressure is dependent only on the surface pores, low capillary pressure is correlated with surface defects. Due to the defects inherent in the manufacturing process, the advancing capillary pressure was found through initial tests to be substantially less than the receding capillary pressure, so that measurements for the advancing capillary pressure were not taken for most of the samples.

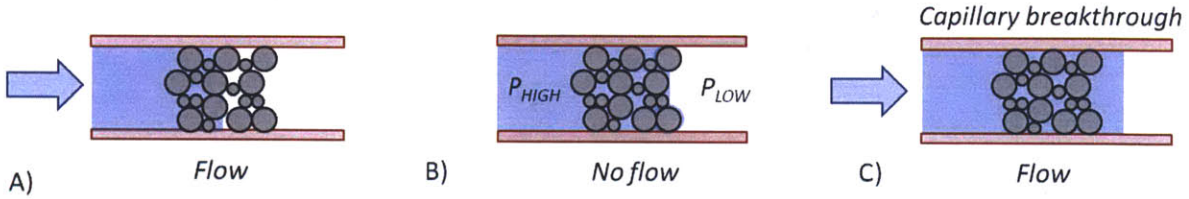

Figure 3.16. Procedure for measuring the receding capillary pressure. A) With a slow flow, the wick sample is saturated with liquid. B) A capillary meniscus is formed at the interface of the saturated wick and air, and the capillary pressure stops the flow. C) As the pressure of the liquid is increased, the maximum capillary pressure is exceeded and the flow resumes.

3.4.2 Application of Wick Properties to Heat Pipe Performance

Table 3.2 shows the sintering parameters and measured properties of the wicks. A) lists the fine powder wicks for the evaporator and B) lists the coarse powder wicks for the condenser. In general, the thermal conductivity of a sintered sample is a fraction of that of the solid. Fine powder results in smaller effective pores and larger capillary pressure, but at a cost of lower permeability. A wider powder size range results in a compromise, in which the receding capillary pressure is decreased but the permeability is increased. The advancing capillary pressure is significantly lower than the receding capillary pressure, and is not a viable option to prevent condenser flooding. The copper and stainless steel powders were purchased from Alfa Aesar (Ward Hill, MA, *42689, 43385, 10160* and *45516*). The 40-75 μm and 75-100 μm powders were hand-sieved from 40-90 μm and < 100 μm stocks, respectively. The nickel powder was purchased from Novamet (Wyckoff, NJ, *Type 123*) and the Monel powder from Micron Metals Inc. (Bergenfiled, NJ, *ML-100*).

Table 3.2. Sintering parameters and properties of A) fine-powdered and) coarse-powdered wicks. "S" and "NS" indicate spherical and non-spherical, respectively. (*) indicates data from a colleague, Dominguez-Espinosa [59]

A)

Powder	Copper (S) 5-15 μm	Nickel (NS) 3-7 μm	Stainless Steel (NS) 5-15 μm	Monel 400 (NS) < 44 μm
Sintering Temp. (°C)	550	850	850	850
Sintering Time (min)	30	30	30	30
Permeability (m^2)	$0.96*10^{-13}$	$0.9*10^{-14}$	$0.72*10^{-13}$	$1.5*10^{-12}$
Thermal Cond. (W/m-K)	59.1*	9	1.1	2.4
Rec. Cap. Pressure (kPa)	72	29	67.6	18.7
Adv. Cap. Pressure (kPa)	0.77	0.48		

B)

Powder	Copper (S) 40-90 μm	Copper (S) 40-75 μm	Copper (S) 75-100 μm
Sintering Temp. (°C)	850	850	850
Sintering Time (min)	30	30	30
Permeability (m^2)	$3.6*10^{-12}$	$1.9*10^{-12}$ *	$8.3*10^{-12}$
Thermal Cond. (W/m-K)	32.4*	27.5*	22.1*
Rec. Cap. Pressure (kPa)	10.2	12.4*	5.4
Adv. Cap. Pressure (kPa)	0.38		0.3

3.4.3 Evaluation of the Fine Powder Wicks for the Evaporator.

The results of the analytical model were used to evaluate the thermal conductivity, permeability, and capillary pressure of the fine powder wicks for integration in the evaporator.

Thermal conductivity: Due to the high thermal conductivity of the copper wick, it is difficult to create the necessary thermal gradient in the evaporator. While the nickel wick has a sufficiently low thermal conductivity to prevent condenser flooding, Figure 3.6 shows that the range of heat loads in which flooding is prevented is noticeably smaller than that of the stainless steel or Monel wicks.

Permeability: As shown in Figure 3.7, a significant increase in viscous pressure loss occurs between the permeabilities of 10^{-14} and $5*10^{-14}$ m^2, and thus the stainless steel and Monel wicks are preferable to the nickel wick.

Capillary pressure (receding): The nickel, stainless steel, and Monel wicks have a higher maximum capillary pressure than the required capillary pressures predicted in Figure 3.6 and Figure 3.8 for operation at 1000 W. While the nickel wick results in a high viscous pressure loss in the evaporator (7 kPa), the capillary pressure in the condenser is not large (3-4 kPa), and the cumulative pressure drops of the cycle are not expected to exceed the maximum capillary pressure (29 kPa). The stainless steel wick can sustain high capillary pressure (68 kPa), allowing for circulation despite the high condenser capillary pressure (9-10 kPa) and moderate viscous pressure loss (2-3 kPa) in the evaporator. The permeability of the Monel wick is sufficiently low so that the viscous pressure drop in the evaporator can be neglected in comparison to the capillary pressure in the condenser. The cumulative pressure drop of the cycle is predicted to be

predominantly due to the condenser capillary pressure (8-9 kPa), which is approximately a half of the maximum capillary pressure (19 kPa).

3.4.4 Evaluation of the Coarse Powder Wicks for the Condenser.

The properties of the coarse powder wicks were also evaluated using the analytical model for integration in the condenser. The effects of the thermal conductivity on the sub-cooling and the permeability on the condenser capillary pressure were analyzed.

Thermal conductivity: The thermal conductivities of the three wicks are within the range of conductivities shown in Figure 3.11, and are low enough to allow sufficient sub-cooling with a sub-cooler length of less than 10 mm.

Permeability: Figure 3.9 indicates that a noticeable increase in viscous pressure loss occurs at a permeability of approximately $2*10^{-13}$ m^2. As a consequence, a larger range of heat loads results in condenser flooding (Figure 3.10). Figure 3.10 also shows that permeabilities of greater than $2*10^{-13}$ m^2 have a small effect on the condenser capillary pressure. The permeability of the 40-75 μm wick approximately matches this threshold value, whereas higher permeabilities were obtained for the 40-90 μm and 75-100 μm wicks. While the latter two are preferable, all three wicks can be integrated into the condenser.

Capillary pressure (receding): The capillary pressure of the 75-100 μm wick is lower (5.4 kPa) than the 40-90 μm and 40-75 μm wicks (10.2 and 12.4, respectively). Use of the 75-100 μm wick requires an evaporator wick with a thermal conductivity greater than 5 W/m-K to limit the condenser capillary pressure at 1000 W. While this can be achieved by use of the nickel wick, the heat pipe must be operated above 550 W to prevent condenser flooding in the inverted orientation. The higher capillary pressures of the 40-90 μm and 40-75 μm wicks allows the use of evaporator wicks with thermal conductivities as low as 1 W/m-K.

3.4.5 Summary of Wick Evaluation

For the evaporator, the stainless steel and Monel wicks are best suited to generating a high capillary pressure in the condenser and maintaining a low cumulative pressure drop. To ensure a wide heat load range without condenser flooding, a high capillary pressure is required in the condenser at 1000 W. The 40-90 μm and 40-75 μm wicks are suitable for the condenser, with the 40-90 μm wick resulting in a slightly higher condenser capillary pressure due to the higher permeability. Since the permeabilities of the Monel < 44 μm and the copper 40-75 μm wicks are similar, the Monel wick can also be used in the condenser.

In addition to assessing the theoretical performance that can be achieved with these wicks, the effects of the wick materials on the heat pipe longevity must also be considered. Heat pipes that use water as the working fluid are generally constructed with copper and operate for several thousands of hours without change in thermal resistance. In contrast, previous studies have shown that hydrogen gas generation occurs in stainless steel-water heat pipes after extended operation [60-63]. Although the

thermal resistance of Monel-water heat pipes has been found to rise with prolonged operation, the magnitude of the rise was considered to be insignificant in comparison to the total thermal resistance [60, 63].

The most appropriate combination for a production-version of the heat pipe is therefore: the Monel wick in the evaporator, with the 40-90 μm, 40-75 μm or Monel wick in the condenser. Although this results in the largest heat load range with multiple-condenser functionality, flooding of the lowest condenser is expected below 100 W and 300 W in the upright and inverted orientations respectively.

3.5 Summary

An analytical nodal model was developed to investigate the effects of the wick properties on the multiple-condenser heat pipe. The effects of the evaporator wick thermal conductivity and condenser wick permeability on the condenser capillary pressure were evaluated to understand the limits before flooding occurs in the lowest condenser. A lower evaporator wick thermal conductivity results in a higher capillary pressure in the condenser due to a greater separation of the CC and vapor temperatures. Through a similar mechanism, an increase in heat load also increases the capillary pressure. A higher condenser wick permeability allows less viscous losses and results in higher condenser capillary pressure. As a result, the combination of a low evaporator wick thermal conductivity and high condenser wick permeability prevents condenser flooding for a wide range of heat loads, allowing for minimal thermal resistance. However, as the condenser capillary pressure increases with heat load, the condenser wick must be able to supply a significantly higher capillary pressure than the gravitational pressure head between the condensers. Alternatively, a CPL cycle can be used with an actively heated reservoir to decrease the condenser capillary pressure, alleviating the requirement for a high capillary pressure wick in the condenser.

The effects of the evaporator wick permeability and condenser wick thermal conductivity on the cumulative pressure loss and sub-cooling were also evaluated. For high evaporator wick permeabilities, the dominant pressure drop of the cycle is the capillary pressure in the condenser, whereas for low permeabilities, the viscous pressure drop in the evaporator dominates. A high thermal conductivity of the condenser wick requires a longer sub-cooler length, which decreases the area available for condensation.

Sintered wicks were fabricated from various metal powders, and the capillary pressures and sub-cooling expected from the measured permeabilities and thermal conductivities were evaluated using the results of the model. The combination of wicks in the evaporator and condenser that results in the largest range of heat loads with multiple condenser functionality (>100 W, upright) and the smallest cumulative pressure losses (~10 kPa) was determined to be: Monel <44 μm wick in the evaporator, with a copper 40-90 μm, copper 40-75 μm or Monel <44 μm wick in the condenser. These wicks are used as the basis of detailed design studies of the evaporator and condenser. The design, fabrication, and testing of the evaporator follows in Chapter 4.

4 Development of the Evaporator

4.1 Overview

This chapter reports the development of the evaporator, which consists of the design, fabrication, and experimental characterization. The results of Chapter 3 are used as the basis of a series of two-dimensional and three-dimensional modeling to design the evaporator. The modeling focuses on the reduction of the evaporator thermal resistance and liquid superheat, as well as the management of the CC temperature to prevent condenser flooding. The fabrication procedure is then described, and the results of the thermal-fluidic testing performed on a custom heat pipe cycle are discussed. The experimental results are compared with the model predictions to demonstrate the functionality of the evaporator for integration into the heat pipe.

4.2 Design Requirements

To ensure proper operation of the proposed heat pipe cycle, the evaporator must be designed to provide the necessary capillary pumping as well as to control the temperature of the CC. The evaporator wick needs to be able to supply enough capillary pressure to overcome the pressure drops in the system and suppress vaporization of the superheated liquid to prevent dry-out of the wick. Dry-out can locally prevent the fluid circulation, leading to heat pipe failure. The CC must be maintained within the prescribed temperature window of Equation 2.29 to prevent condenser flooding. The requirement is restated below.

$$\frac{\Delta P_{3-4} + \Delta P_{1-2} + \rho g \Delta h_{T-B}}{\left[\frac{dP}{dT}\right]_{SAT}} \leq T_1 - T_5 \leq \frac{\Delta P_{max\ cap} + \Delta P_{1-2} - \rho g \Delta h_{T-B} + \Delta P_{3-4}}{\left[\frac{dP}{dT}\right]_{SAT}} \quad 4.1$$

Furthermore, since the heat pipe is developed to achieve a low effective thermal resistance, the thermal resistance contribution of the evaporator must be kept to a practical minimum. Consequently, the requirements of the evaporator are as follows.

1) *Provide sufficient capillary pumping.* From Chapter 3, pumping requirement is not expected to exceed 15 kPa for operation at 1000 W. If the pumping requirement exceeds the maximum capillary pressure of the wick, the meniscus will recede into the wick, causing dry-out.
2) *Tolerate steady-state operation with a superheated liquid in the wick.* The generation of capillary pressure results in a low liquid pressure in the wick, rendering it a superheated liquid. Due to this, the magnitude of superheat is the same as the capillary pressure. Sustaining this

metastable state occurs due to capillary suppression of vapor nucleation [18-20, 23]. The maximum suppression is expected to be equivalent to the maximum capillary pressure. Thus, this requirement will be assumed to be automatically fulfilled when requirement 1) is met.

3) *Maintain a low thermal resistance.* The temperature difference between the base of the evaporator and the vapor should be less than 5 °C at 1000 W. This metric is independent of the heat pipe functionality and is focused on its performance for heat sink integration.
4) *Sustain an appropriate liquid-side (CC) temperature.* The temperature range of Equation 4.1 is calculated using the model described in Chapter 3 for compatibility with condensers using 40-90 μm (copper), 40-75 μm (copper) or < 44 μm (Monel 400) wicks. Thus the lower limit is calculated using the lowest condenser permeability of the three wicks for the highest $\Delta P_{3\text{-}4}$. Similarly, the upper limit is calculated using the lowest maximum capillary pressure of the three wicks and the corresponding permeability. At 1000 W and 80 °C, the resulting range is:

$$0.4\,°C < T_V - T_{CC} < 6.0\,°C \qquad 4.2.$$

It should be noted that since the condenser capillary pressure increases with heat load, the prevention of flooding at lower heat loads results in a high capillary pressure at 1000 W. The temperature difference between the vapor and the CC at 1000 W should therefore be closer to the upper limit to ensure a wide operating range with un-flooded condensers. It is likewise advantageous to operate near the upper limit if the evaporator is integrated into a CPL, for reasons discussed in Chapter 2, Section 2.3.

4.3 Evaporator Layout

The wick determines the thermal-fluidic operation of the evaporator. The design of the evaporator is therefore predominately focused the design of the wick. While the wick may be designed first for the desired properties and the evaporator case/frame designed afterwards to fit the wick, in this case, constraints were initially imposed on the evaporator shape. Due to the requirement that the heat sink needs to fit in a 101.6 mm x 101.6 mm x 101.6 mm cubic volume, the base of the evaporator was required to match the 101.6 mm x 101.6 mm footprint. In order to allow the integration of multiple condensers in the prescribed volume, the desired thickness of the evaporator was set to be approximately 10-15 mm. Furthermore, in order to improve the robustness of the device, the fabrication and construction was to be performed through the high temperature processes of sintering, welding, brazing and soldering.

Figure 4.1 shows a cross sectional schematic of the evaporator, where the wick is shown with hatched lines. The evaporator is separated into three sections: the vapor channels (vapor), the wicking structure (liquid, shown hatched in the figure), and the CC (liquid and vapor). To meet the four requirements described above, sintered metal wicks of three different thermal and fluidic properties are used. This is in contrast to the evaporator modeled in Chapter 3, as the analysis focused on maintaining a temperature difference between the vapor and the CC (fourth requirement), for which only an insulating wick was necessary. The properties of the wicks are tabulated in Chapter 3 (Section 3.4.2);

they are also shown in Table 4.1 for reference. To meet the first and second requirement, a wick with high capillary pressure is used at the base of the evaporator to interface with the vapor channels. Furthermore, to meet the third requirement, a high thermal conductivity material is used for this vapor channel wick. A fine copper wick (5-15 μm powder size) is used for this layer. For the fourth requirement, a second wick with low thermal conductivity is used to thermally insulate the CC from the vapor channel wick. Through the analysis performed in Chapter 3, the Monel 400 wick (< 44 μm) is used for this layer. High capillary pressure is also required in this insulating layer, since the vaporization of the superheated liquid must be suppressed. By utilizing a separate, high thermal conductivity wick to interface with the vapor channels, thermal insulation of the CC does not result in a high conductive resistance from the base to the vapor channels. Additionally, a high permeability wick (coarse copper, 40-75 μm) is used to ensure liquid transport from the two-phase CC to the insulating wick. This wick provides a liquid flow path around the vapor region in the CC to prevent local dry-out of the wick, and serves the same purpose as the high permeability "secondary" wick mentioned in previous studies [33, 64, 65]. This secondary wick also facilitates the heat transfer from the reservoir to the convectively cooled top surface of the evaporator. Figure 4.1B shows the heat transfer pathways in the evaporator.

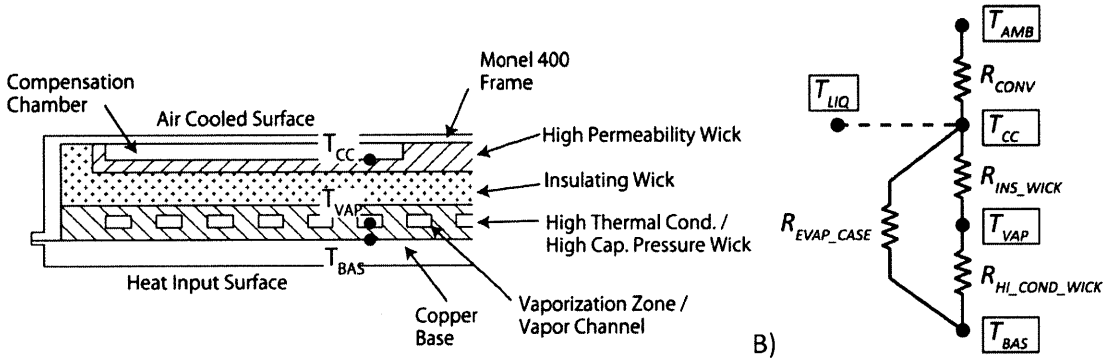

Figure 4.1. Schematic of the evaporator, showing A) a cross-sectional cut and B) the thermal pathways in the evaporator. In B) the conductive resistance from the high permeability wick is neglected, since the convective resistance is significantly larger.

Table 4.1. Wick specifications. Due to the use of a different sintering procedure, the properties of the 5-15 μm copper wick is different than that tabulated in Chapter 3. The 5-15 μm wick was sintered twice at 550 °C for 30 minutes each.

Wick Material	*Powder Size (μm)*	*Thermal Cond. (W/m-K)*	*Permeability (m^2)*	*Cap. Pressure (kPa)*
Copper	*5-15*	*69*	*$0.96 * 10^{-13}$*	*72*
Monel 400	*< 44*	*2.4*	*$1.5 * 10^{-12}$*	*18.7*
Copper	*40-75*	*27.5*	*$1.9 * 10^{-11}$*	*12.4*

The evaporator was designed around the pre-selected wicks; this was done due to the limited selection of metal powders. The design process did not consider the maximum capillary pressure; this was assumed to be inherent to the wick material. The process consisted of two parts: a two and three dimensional computational analysis to determine the vapor channel geometry and a three-dimensional computational analysis to determine the shape of the insulating and high permeability wick layers. Modeling was performed with a finite-element software, COMSOL Multiphysics (COMSOL, Stockholm, Sweden, *COMSOL Multiphysics 3.5a*).

4.4 Vapor Channel Design

The vapor channels were designed for low liquid superheat and thermal resistance. The thermal resistance of the evaporator is defined here as the temperature difference between the base and the vapor exiting the evaporator, divided by the applied heat load. The thermal resistance therefore consists of the following two components:

1) Temperature drop between the base and the vapor channels that occurs due to the conductive resistance across the wick.
2) The saturation temperature drop that occurs from the pressure drop through the vapor channels. Since the vapor remains at saturation throughout the flow in the vapor channels, the pressure drop translates to a temperature drop. Unlike the conductive resistance, this temperature drop is dependent on the fluid properties and therefore on the vapor temperature.

4.4.1 Design for Low Conductive Resistance and Superheat

The effect of the shape and location of the vapor channel was analyzed to reduce the conductive resistance across the wick and the liquid superheat. Liquid superheat is defined here as the pressure difference between the local liquid pressure and the saturation pressure of the local temperature.

Two-dimensional modeling was performed on a symmetric cross section of a single vapor channel (Figure 4.2). The thicknesses of the vapor channel, insulating and high permeability wicks were 4.5 mm, 4 mm and 3.5 mm, respectively, and were not changed in the analysis. The CC and vapor channel were modeled as channels inside of the high permeability and high conductivity wicks. As shown in Figure 4.2, The shape and location of the vapor channel was defined by three parameters: the vertical distance from the base (Z), the width of the symmetric section (W), and the ratio of this half-channel width to the width of the symmetric section (X/W). The height of the channel was found to minimally affect the thermal resistance and was not varied. Increasing W has the effect of decreasing the number of channels in the evaporator, as

$$n = \frac{L}{2W} \tag{4.3}$$

where L is the length of the vapor channel network, which is 85 mm. A larger number of channels decreases the mass flow per channel, as

$$\dot{m}_{channel} = \frac{\dot{m}_{total}}{n} \tag{4.4.}$$

where $\dot{m}_{total}$ is the total mass flow rate at the applied heat load. Wick properties from Table 4.1 and water properties at 80 °C were used for the analysis. The bottom and top surfaces of the evaporator were modeled as 1 mm thick copper and Monel plates with thermal conductivities of 400 W/m-K and 25 W/m-K, respectively.

Modeling was performed by setting the base temperature to 80 °C and adjusting the vapor channel temperature, which was modeled as spatially uniform in the channel, so that the heat flux through the base was 10^5 W/m^2, which is the heat flux at 1000 W. The heat transfer into the vapor channel was

equated to the latent heat from the evaporative mass flow. The liquid pressure in the CC was defined as the saturation pressure at a temperature 3, 5 and 6.5 °C below that of the vapor (denoted as $T_{CC}=T_V-X$, where X is the temperature difference). A convective boundary condition of 100 W/m^2-K was applied to the top surface to simulate the cooling from the fan, with an ambient air temperature of 30 °C. The outputs of the model were the vapor temperature and the maximum liquid superheat, which was analyzed for the location marked in Figure 4.2. This location was determined to have the highest superheat in the system, as the pressure is low and the temperature is high (relatively constant at 79.8-79.9 °C). It is useful to note that because the lowest liquid pressure at the evaporation meniscus is approximately equal to the liquid pressure at the location of maximum liquid superheat, the maximum capillary pressure in the vapor channel is approximately equal to the maximum liquid superheat.

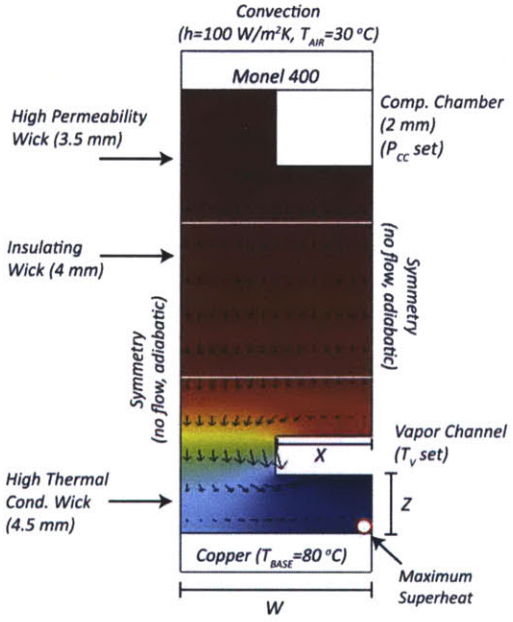

Figure 4.2. Analysis domain of the two-dimensional modeling. The color contour indicates a schematic pressure gradient; the arrows show the flow pattern of the liquid in the wick.

Figure 4.3 shows the effect of the vertical position of the vapor channel, for a X/W ratio of 0.5 and a base temperature of 80 °C. Decreasing the distance from the base (Z) decreases the length of conduction across the wick, allowing for a higher vapor channel temperature for a given base temperature (Figure 4.3A). This translates to a smaller temperature drop across the wick and a lower thermal resistance (Figure 4.3B). For a given X/W, a wider vapor channel has a slightly higher temperature drop due to a longer conduction path.

The viscous pressure drop through the wick decreases with increasing Z as the flow path becomes less constricted and serpentine (Figure 4.3C). The pressure drop is greater for larger values of W, since a greater mass flow must transport through a longer distance in the wick. Most of the pressure drop occurs through the vapor channel wick, since the other two wick layers with higher permeabilities account for approximately 100 Pa. Figure 4.3D shows an increase in superheat with increasing Z, for a CC saturation temperature of $T_{CC}=T_V-5$, which results in a saturation pressure difference between the

vapor and CC of approximately 8 kPa when T_V is 77 °C. Superheat is determined by the liquid pressure, which is affected by the viscous pressure loss through the wick as well as the CC pressure. Although the pressure drop falls with increasing Z, the overall liquid pressures decrease as the CC pressure follows the decrease in the vapor temperature. The latter effect dominates, causing the superheat to rise. Consequently, to minimize the conductive resistance and superheat, Z should be decreased to the manufacturable limit. The effect of the CC pressure on the superheat is shown in Figure 4.3E. As the CC pressure is increased (smaller saturation temperature difference from the vapor), the superheat increases by an equal amount. Any saturation temperature difference between the CC and the vapor therefore results in superheat, in addition to the effect of the viscous pressure drop through the wick.

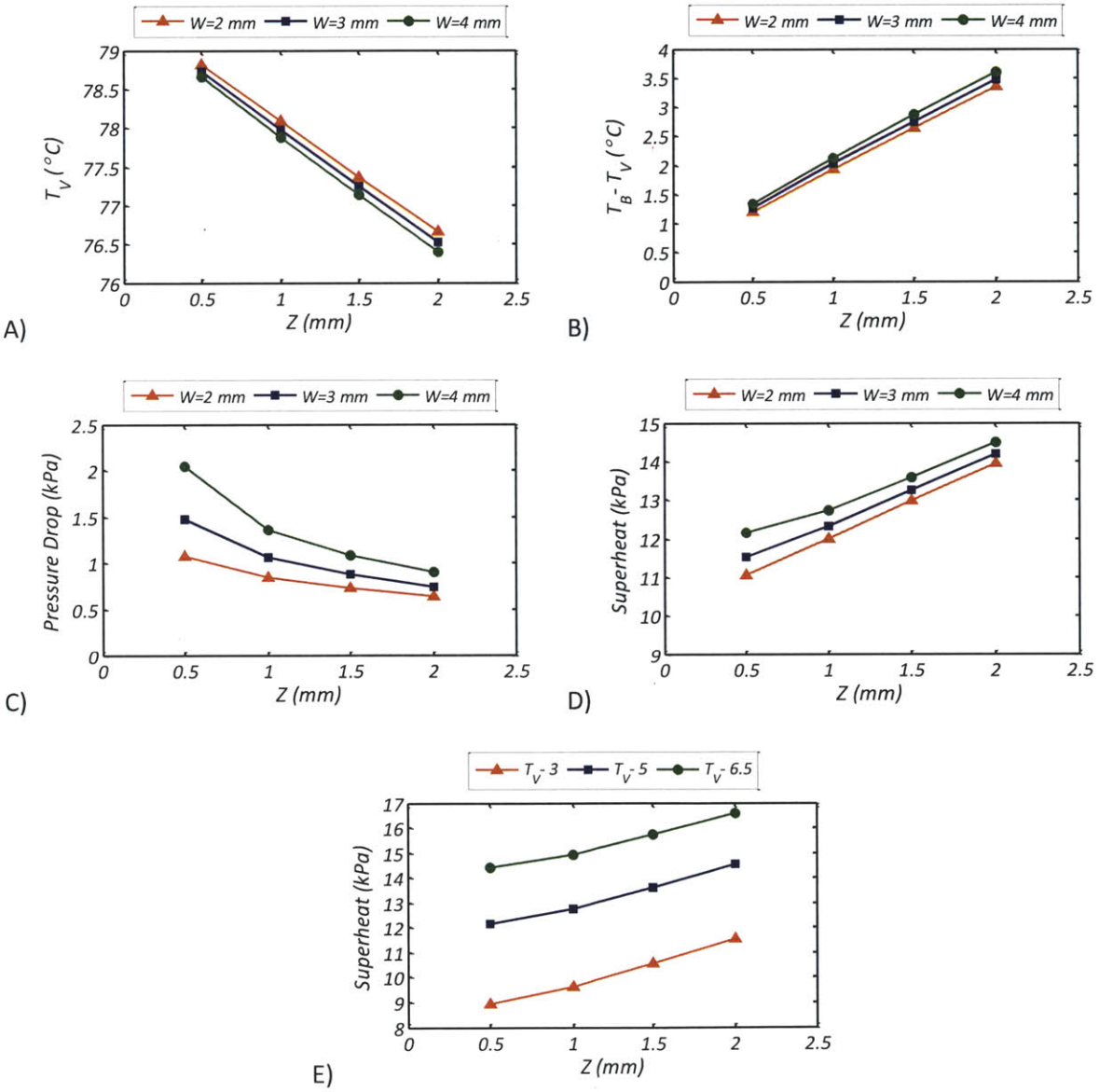

Figure 4.3. Effect of the vertical position of the vapor channel for X/W=0.5; on A) vapor temperature, B) temperature difference between the base and the vapor, C) pressure drop through the wick, and D) superheat, for different channel widths. D) is plotted for a CC saturation pressure at $T_{CC}=T_V-5$. E) shows the effect on the superheat for different CC pressures, for W=4 mm.

Figure 4.4 shows the effect of X/W when the vapor channel is 1.5 mm away from the base, which is held at 80 °C. A larger X/W indicates that a larger percentage of the footprint area is occupied by the vapor channels, where X/W=1 indicates a single vapor channel, spanning the entire area. As this limit is approached, conduction across the vapor channel wick approaches a simple one dimensional case and the conduction path is minimized. As a result, the vapor temperature increases and the conductive thermal resistance decreases (Figure 4.4 A and B). However, as X/W is increased, the fluidic path in the wick between the channels becomes constricted and the flow length increases, causing an increase in the pressure drop (Figure 4.4C). Both vapor temperature and pressure drop affect the superheat, and Figure 4.4D shows the interplay of the two parameters. The CC pressure increases with the vapor temperature (increasing X/W), resulting in an overall increase in the liquid pressures that lowers the superheat. However, the increase in the pressure drop with increasing X/W has the effect of increasing the superheat, and as a result, the superheat has a local minimum at X/W between 0.4 and 0.6.

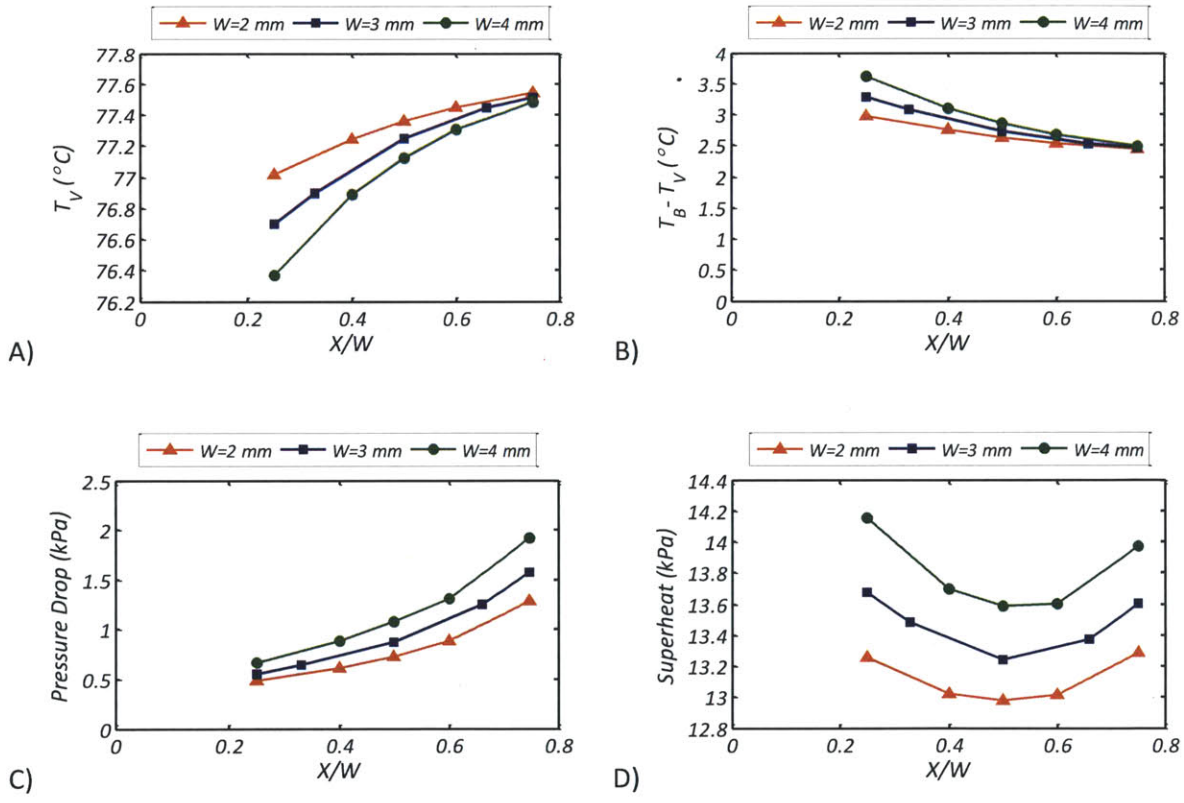

Figure 4.4. Effect of the width of the vapor channel for Z=1.5mm; on A) vapor temperature, B) temperature difference between the base and the vapor, C) pressure drop through the wick, and D) superheat, for different channel widths. D) is plotted for a CC saturation pressure at $T_{CC}=T_V-5$.

4.4.2 **Pressure Drop in the Vapor Channels**

The pressure drop in the vapor channels results in a drop in saturation temperature, which contributes to the thermal resistance of the evaporator. A three-dimensional model was developed to simulate the pressure drop occurring through a single channel to analyze the effects of X/W and W. Figure 4.5 shows

the channel modeled for this analysis. Each channel is connected at the ends to two manifolds which direct the flow to the two vapor exit ports. A uniform mass flux was imposed on the surfaces of the channel, where the mass flux was determined by the following relation:

$$m" = \frac{\dot{m}_{total}}{nA_{channel}} \qquad 4.5$$

where $A_{channel}$ is the surface area of each channel. The channel was modeled to be 80 mm in length with fluid outlets at both ends. The outlets were approximated as open boundaries with equal pressures. Water vapor properties were taken at 80 °C.

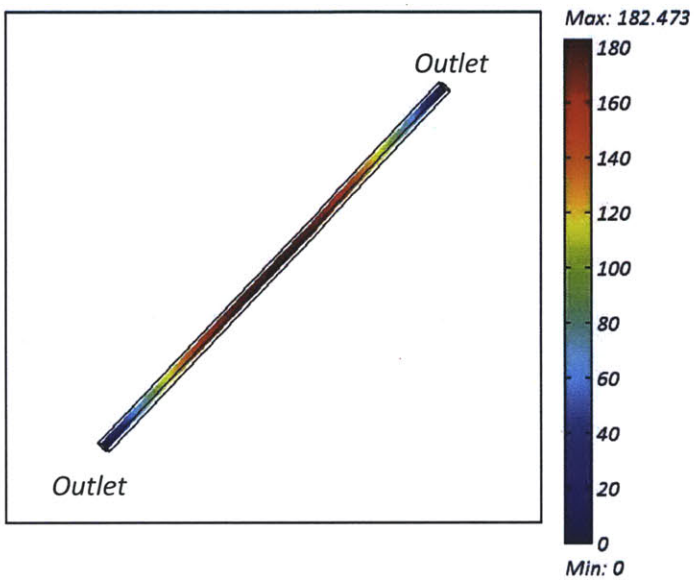

Figure 4.5. Pressure drop (Pa) in a single vapor channel. The results shown for X/W=0.6, W=3 mm.

Figure 4.6 shows the dependence of the pressure drop in the vapor channels on W and X/W. Increasing X/W and W provides a larger cross sectional area of the channel, which decreases the pressure drop through a slower vapor velocity. However, the decrease in pressure drop with increasing W is not as noticeable at larger W, since the mass flow per channel increases due to the decrease in number of channels. The effect of W is less critical for higher values of X/W, such that at X/W of 0.5, the decrease in pressure drop (~100 Pa) with an increase in W from 2 to 5mm results in less than a 0.1 °C saturation temperature difference for a vapor temperature of 77-78 °C.

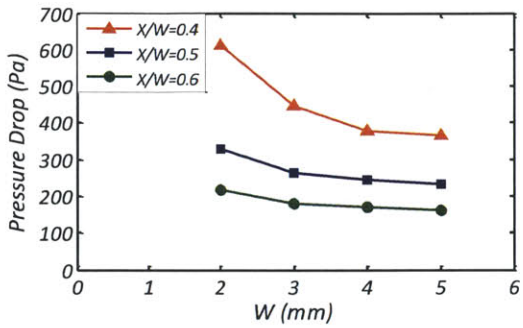

Figure 4.6. Viscous pressure drop in a single vapor channel, for different W and X/W.

Combining the results from Figures 4.3B, D, 4.4B, D and 4.6, X/W of 0.6 and W of 3 mm were selected for the vapor channel. X/W of 0.6 meets a balance of minimizing of the conductive resistance and superheat in the wick and reducing the pressure drop in the vapor channels. While Figure 4.3B and Figure 4.4B suggest that a lower W should be used for minimizing the conductive thermal resistance across the wick, 3 mm was chosen considering the manufacturability of the channels. Similarly, the manufacturable limit for Z was found to be approximately 1.4 mm. For this geometry, the conductive thermal resistance between the evaporator base and vapor channels is 2.6 °C and the vapor pressure drop through an individual channel is 180 Pa. The manifold was also designed for the maximum manufacturable cross sectional area of 2 mm in height and 6 mm in width. The vapor channel and manifold were then integrated into a full channel network and modeled for the total pressure drop using a uniform (evaporative) mass flux boundary condition with two vapor outlets. Figure 4.7 shows the pressure drop profile for operation at 1000 W and a vapor temperature of 77.4 °C. The vapor undergoes a pressure drop of 1380 Pa, for a corresponding saturation temperature drop of 0.8 °C. A significant fraction of the pressure drop occurs near the constricted vapor exit ports.

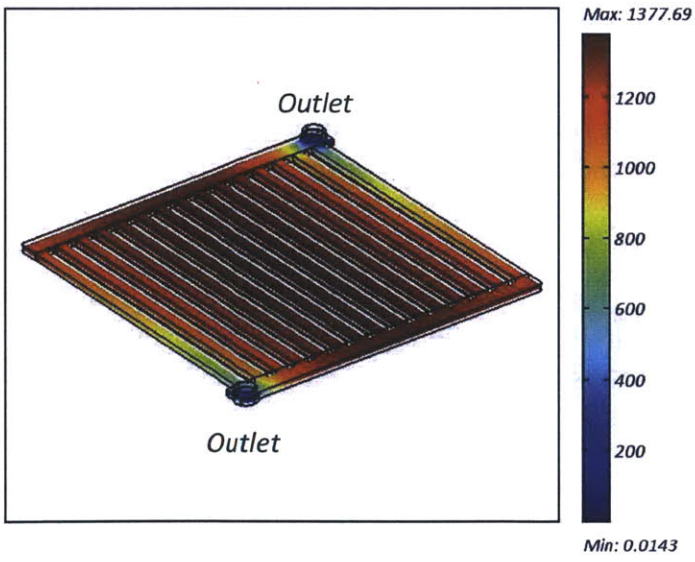

Figure 4.7. Pressures (Pa) in the vapor channel network. Results shown for operation at 1000 W, with a vapor temperature of 77.4 °C.

While the pressure drop analysis above focused on operation at 1000 W with an evaporator base temperature of 80 °C, it is useful to understand the pressure drop in the vapor channel network at other heat loads and temperatures. Figure 4.8 shows the pressure drop as function of the heat load and vapor temperature. For a given temperature, the pressure drop is higher for larger heat loads due to the increase in mass flow rate. For a given heat load, the pressure drop is higher for lower temperatures, due to higher mass flow rates from lower densities. The black curve (marked as "-X-") shows the expected pressure drop in the multiple-condenser heat pipe, which was calculated using the relationship between vapor temperature and heat load developed in Chapter 3 (Figure 3.3). The increase in pressure drop is less at higher heat loads due to the higher temperature.

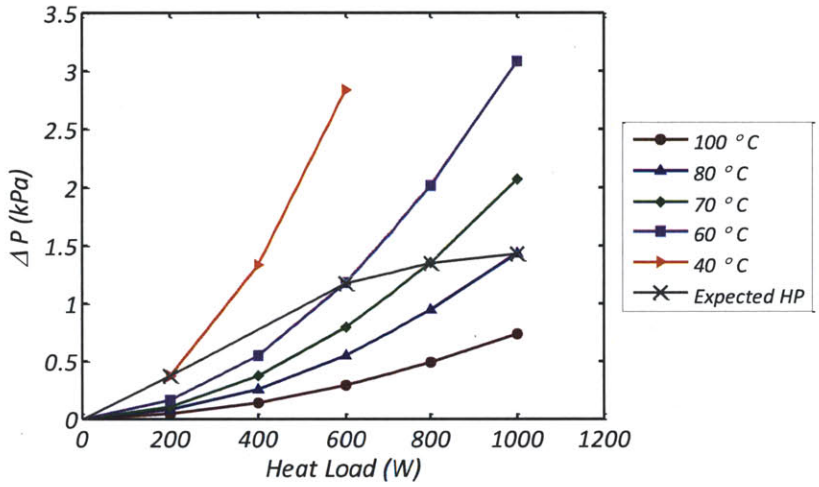

Figure 4.8. The pressure drop in the vapor channel network, as a function of the heat load and the vapor temperature. For a given heat load, the pressure drop decreases as the vapor temperature increased due to a higher density and thus a lower mass flow rate. The black curve labeled with crosses shows the expected pressure drop for the multiple-condenser heat pipe.

4.5 Insulating and High Permeability Wick Design

The shape of the insulating and high permeability wick layers were designed to maintain the CC within the temperature range of Equation 4.2. Three-dimensional modeling was required to take into account the conduction through the walls of the evaporator case (Monel 400), which is a significant local conduction path due to the higher thermal conductivity (25 W/m-K) compared to the insulating wick (2.4 W/m-K). This is in contrast to the modeling of the vapor channel wick, where a two-dimensional analysis is more appropriate due to the significantly higher wick conductivity (69 W/m-K) than the Monel casing.

Figure 4.9 shows the top and cross sectional views of the wicking structure. The two liquid and two vapor ports are located at the corners of the top surface for liquid entry and vapor exit. The vapor flow between the vapor channel manifold and the vapor ports is separated from the liquid side by the evaporator case (Figure 4.10). The CC is shown as a channel network in the high permeability wick. To insulate the CC against the conduction through the casing, the insulating wick layer is designed in a "cup"

form, in which the CC is insulated by the wick on the bottom (base layer) as well as the sides (sidewall). The sidewall also insulates against the heat transfer from the high temperature vapor ports. The case wall is thinner near the liquid port to minimize the heat transfer to the incoming liquid, since a high liquid port temperature may cause the vapor region of the CC to form at the port, preventing the circulation of the fluid. A bearing insert is made at the center of the evaporator for the fan shaft, resulting in the absence of the high permeability wick beneath the insert.

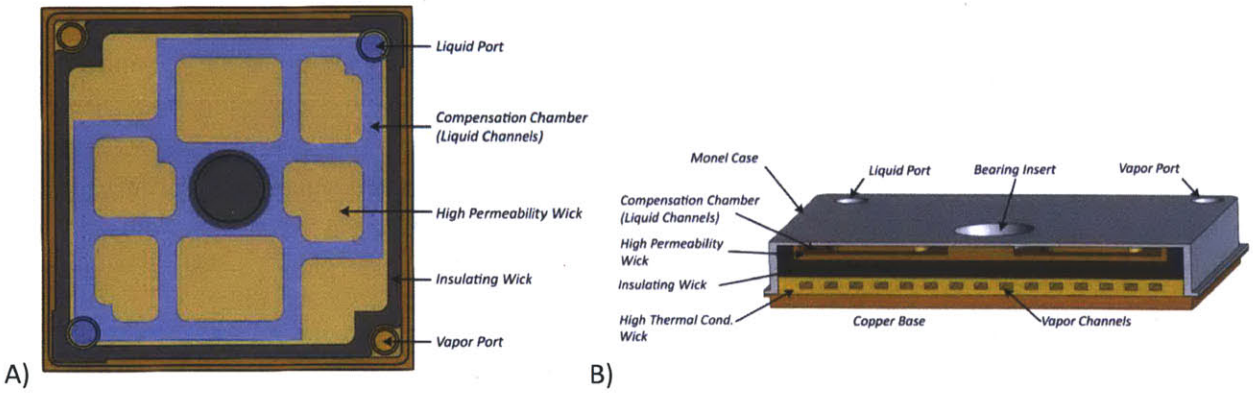

Figure 4.9. Evaporator design. A) Top view of the wicking structure; the Monel case is transparent in this view. The grey wick is the insulating Monel wick, the light orange the high permeability wick, and the dark orange the solid copper base plate. The high permeability wick is absent at the center due to the indentation in the case for the fan bearing. B) Cross sectional view of the wicking structure.

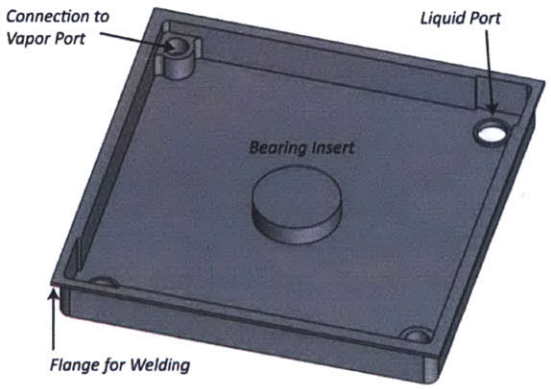

Figure 4.10. Evaporator case. The vapor flow is separated from the liquid side by the case. The case is thinner near the liquid ports to minimize the heat transfer to the liquid entrance.

Figure 4.11 shows the temperature profile of the CC, for an insulating wick with a base layer thickness of 4 mm and sidewall thickness of 3.8 mm. The total thicknesses of the high permeability wick and vapor channel wicks are 3.5 and 4.5 mm. The profile is taken at the lowest plane of the CC and is indicative of the hottest temperatures. Modeling was performed with a base temperature of 80 °C and a vapor channel temperature of 77.2 °C, through the same iterative scheme as in the two dimensional modeling for a heat load of 1000 W. The temperature drop between the base and the vapor channels is slightly higher than that of the two dimensional modeling due to the higher conductive resistance near the large vapor manifolds. Boundary conditions include convective heat transfer at the top surface (100 W/m^2-K)

and side surfaces (20 W/m^2-K) of the Monel case, and a sub-cooled liquid at T_V-5 °C entering the liquid ports. The air temperature was modeled to exponentially rise from 30 °C (ambient temperature) to 40 °C as the air flowed radially across the surface of the evaporator, from the center to the outer corner [31]. The degree of sub-cooling was determined from a separate study on the condenser performance [66]. Figure 4.11 shows that while the sidewall wick provides adequate insulation for most of the CC, the vapor ports cause substantial heating of the CC in the two corners. These corners are filled with the high permeability wick to prevent high temperature vaporization while permitting fluid flow with little pressure drop. Similarly, the high permeability wick fills multiple locations in the CC and forms a thermal connection with the top surface of the evaporator. These regions are shown in Figure 4.9 and Figure *4.11* as rectangular blocks and facilitate the convective cooling of the CC. The non-wicked, open space of the CC is a network of channels between these blocks and is 2 mm in height. Figure 4.11 shows that the hottest locations in the channels occur against the walls as well as near the vapor port corners, and is 72.6 °C for the modeled condition. This results in a T_V-T_{CC} of 4.6, meeting the fourth requirement from Section 4.2 (Equation 4.2.).

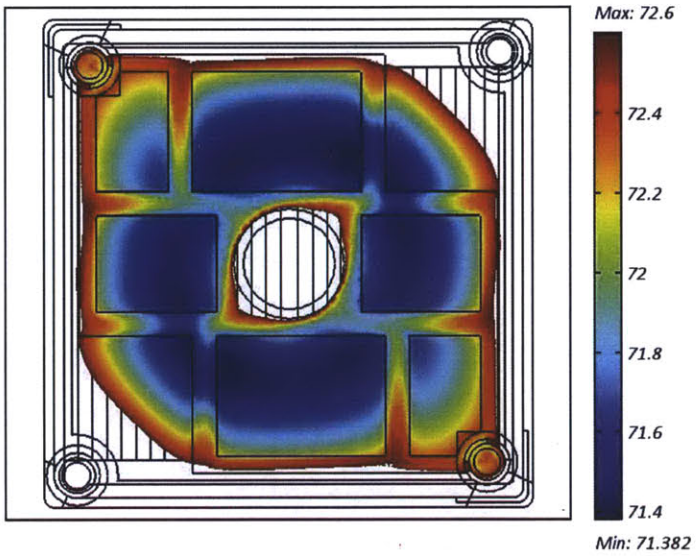

Figure 4.11. Temperature profile (°C) of the lowest (hottest) plane of the CC. The square regions are the high permeability wick that contact the upper surface of the Monel case, and the channels constitute the open space for the CC.

Figure 4.12 shows the pressure drop through the wicking structure at the hottest location in the evaporator, directly above the base plate. The pressure drop at the vapor channels towards the center of the evaporator is approximately 1200 Pa, and matches that of the two-dimensional modeling. The average pressure drop is approximately 1400 Pa. A greater pressure drop occurs below the bearing insert, where there is less wick material to supply a fluid path. Likewise, the pressure drop is larger below the larger manifold channels and the vapor port corners, as the flow path in the wick is longer and more constricted. The larger manifold size facilitates a lower vapor pressure drop, but at the cost of an increase in liquid pressure drop (+500 Pa). The same trends are seen for the liquid superheat in the wick (Figure 4.13), which is also similar to the results of the two-dimensional analysis for the region towards the center of the evaporator (11.5 kPa). Locations with higher pressure drop have higher

superheat. The highest superheat occurs at the vapor port corners due to the low liquid pressures. Partial dry-out in these corners is not expected to noticeably affect the operation and thermal resistance of the evaporator because of the small affected area. Furthermore, since the capillary pressure of the fine (5-15 μm) copper wick around the vapor channels (69 kPa) substantially exceeds the predicted superheat, vapor nucleation in the wick and thus dry-out is not expected to occur. This meets first and second requirements of the evaporator design from Section 4.2.

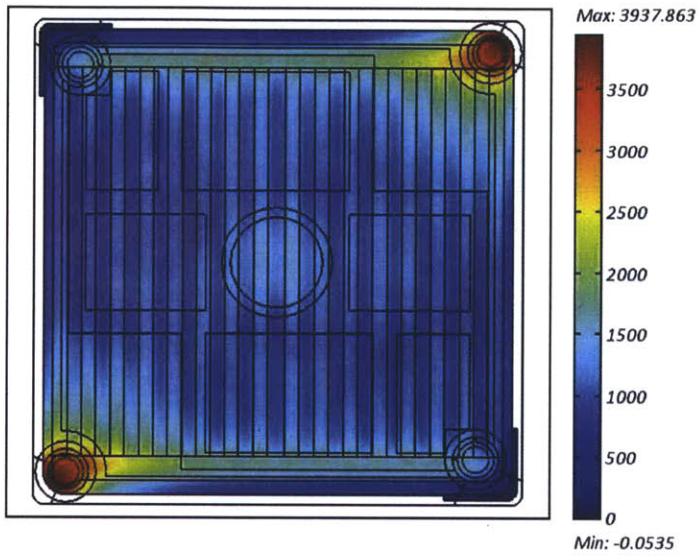

Figure 4.12. Pressure drop (Pa) through the wick, shown for the plane directly above the copper base.

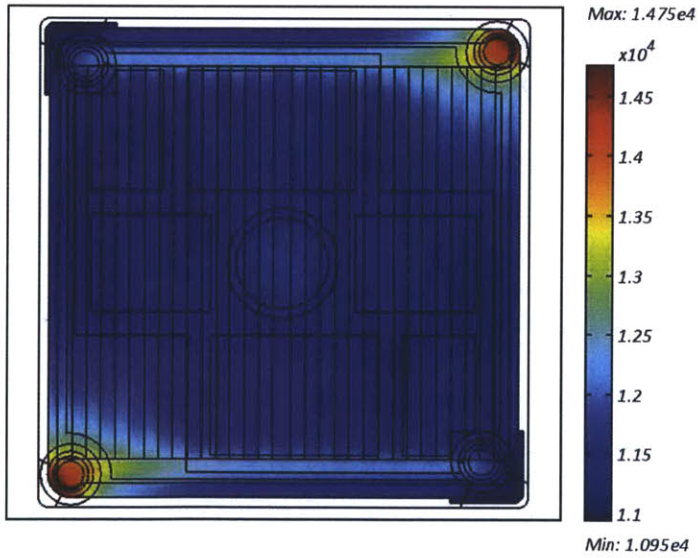

Figure 4.13. Superheat (Pa) in the wicking structure, shown for the plane directly above the copper base, which is the hottest location in the heat pipe. Superheat is calculated as the difference between the saturation pressure at the local temperature and the actual pressure of the liquid.

The results of the three-dimensional modeling can be summarized for operation at 1000 W and a base temperature of 80 °C as follows. The conductive resistance from the base to the vapor channel results in a temperature drop of 2.8 °C and the pressure drop through the vapor channel network results in a 0.8 °C drop, for a total temperature drop of 3.6 °C. Hence a thermal resistance of 0.0036 °C/W is expected at 80 °C. This fulfills the third requirement in Section 4.2. It is important to note, however, that this analysis involves a simplification to avoid the heavy computational requirements of thermal-fluidically modeling the capillary meniscus. The conductive resistance was modeled independently of the vapor channel pressure loss, and used a uniform vapor channel temperature and uniform heat flux as boundary conditions. Similarly, the fluidic analysis of the vapor channel used a uniform heat (mass) flux boundary condition. However, the fluidic analysis assumed that the pressure loss translates to a saturation temperature drop, which results in a thermal gradient in the channel network. The actual operation of the evaporator, in contrast, is expected to have a non-uniform heat flux and a thermal gradient in the vapor channel network, which is caused by the pressure loss in the channel network. The copper base plate will be approximately uniform in temperature, and the areas with lower vapor channel temperature, near the vapor ports, will see a higher heat and mass flux. However, due to this, the regions of the vapor channel network far from the vapor ports will see less heat and mass flux, alleviating the pressure drop in these regions. The modeled conditions can therefore be considered to be an average scenario, in which an average vapor temperature is assumed for calculating the conductive resistance and a high value is calculated for the vapor channel pressure loss due to the uniform mass flux boundary condition.

4.6 Fabrication

The modeled wick design was transferred to a manufacturing process through multiple sintering cycles, resulting in a monolithic, multi-layer wicking structure bonded to the evaporator case. The fabrication steps are shown in Figure 4.14 with the corresponding sintering temperatures and times, and Figure 4.15 shows the components. Since the fabrication process consists of multiple sintering cycles, each subsequent cycle is performed at a lower temperature to avoid excessive shrinkage from over-sintering. All sintering cycles were performed in a 150 mm diameter tube furnace in a reducing atmosphere of 5% hydrogen and 95% nitrogen, with the same temperature profile and process as described in Chapter 3, Section 3.4.1. The fabrication process is as follows.

1) First fabricate the three-dimensional (channel) features of the vapor channels and the CC by sintering in graphite molds (Figure 4.15). These wicks will be referred to as the "pre-sintered structure."
2) Attach the pre-sintered CC channel structure to the Monel case with a sintered film of coarse (40-75 μm) copper powder. The insulating wick is also sintered in the same step; the Monel powder is layered on top of the pre-sintered CC channel structure.
3) Attach the pre-sintered vapor channel structure to the solidified insulating wick by another film of fine (5-15 μm) copper powder. Flaws, or large voids, at the bonding interface between the vapor channel and the insulating wicks can lead to the nucleation of vapor due to the high liquid

superheat. The vapor prevents the liquid from flowing to the vapor channels and increases the thermal resistance.

4) After the pre-sintered vapor channel structure is sintered in place, fill the remaining open volume with the fine copper powder. The copper base plate is then installed as a lid to the case, and sintered together. The thermal contact between the base place and the vapor channel wick is critical for minimizing the thermal resistance.
5) Fusion-weld (gas tungsten arc welding) the base plate to the case for a hermetic seal. The evaporator and base plate have 1 mm thick, 1.5 mm long flanges for the welding. To ensure a non-porous weld, oxygen-free high conductivity (OFHC) copper was used for the base plate and the entire assembly was heated in a vacuum furnace (250 °C, 4 hours) prior to welding to remove any dissolved hydrogen from the sintering cycles. Figure 4.16 shows a completed evaporator with the welded seam, which was tested on a helium leak detector (Adixen, Hingham, MA, *ASM 142*) to be leak tight to $6*10^{-10}$ standard cm^3/sec.

Figure 4.17 shows a cross sectional cut of a prototype evaporator. The precision of the sintered features are 0.2 mm and 0.3 mm in the direction normal and perpendicular to the base plate, respectively.

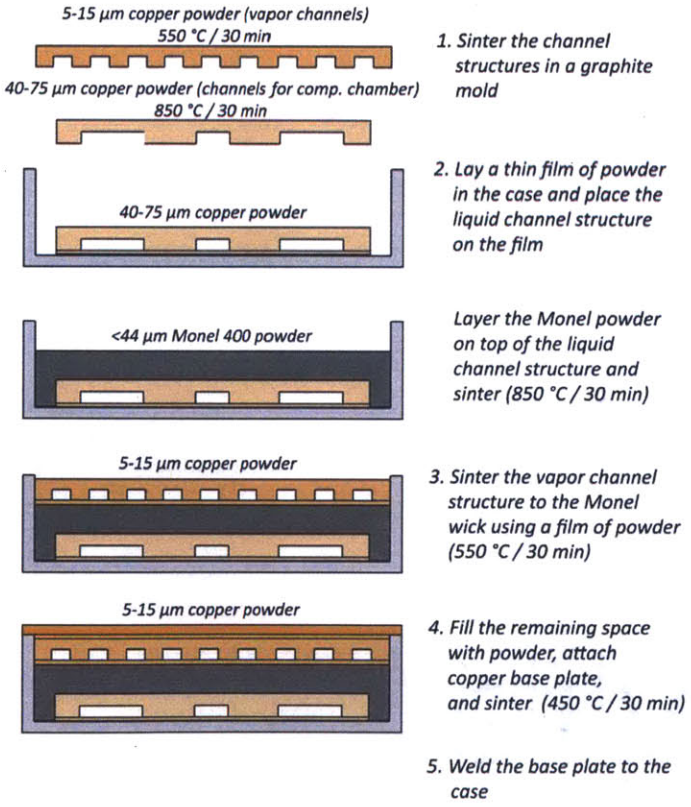

Figure 4.14. Fabrication process of the evaporator.

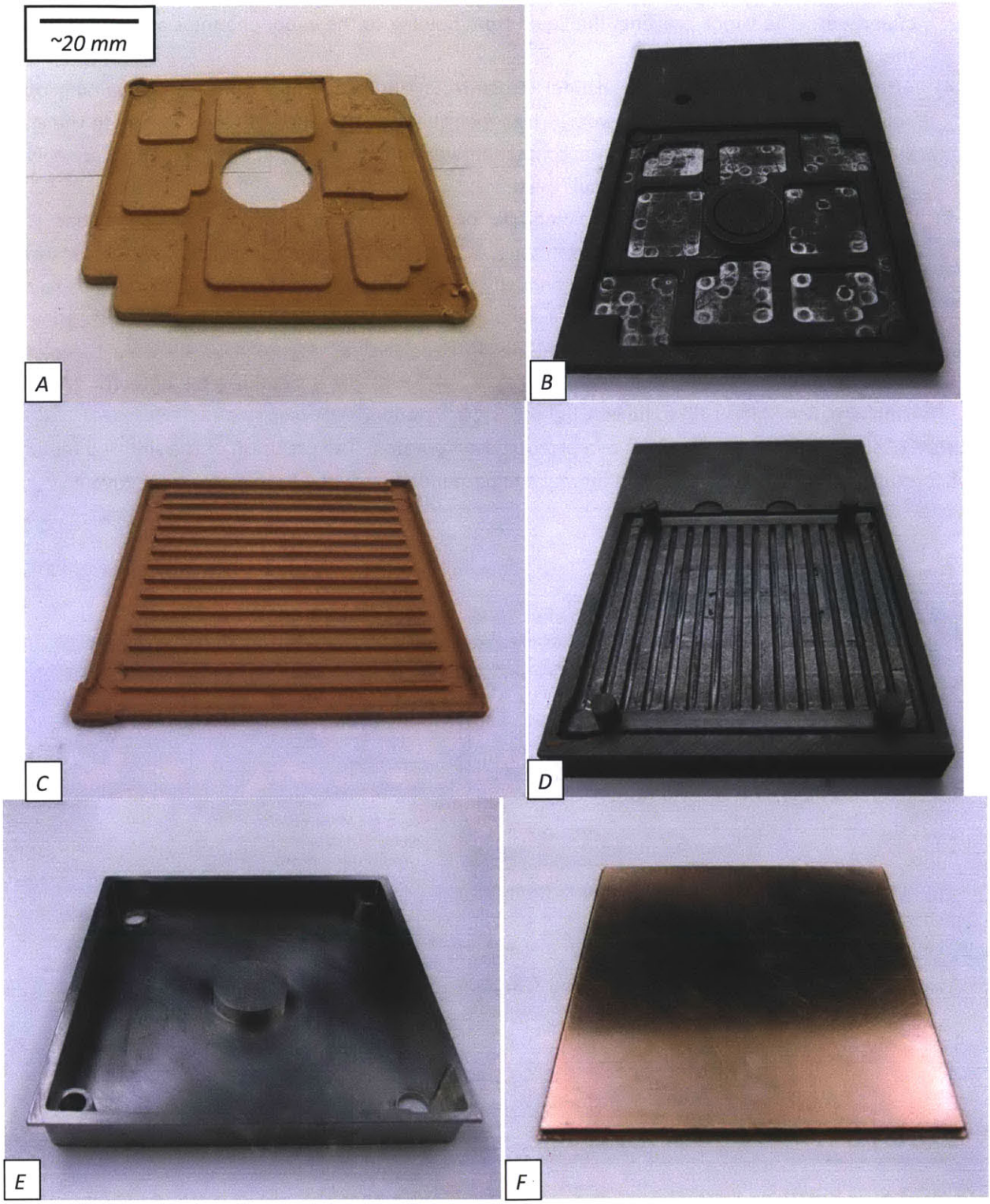

Figure 4.15. Components of the evaporator fabrication: A) high permeability wick for the CC, B) graphite mold for fabricating the CC wick, C) high thermal conductivity/high capillary pressure wick for the vapor channels, D) graphite mold for fabricating the vapor channel wick , E) evaporator case, and F) copper base plate. The mold for the vapor channel wick has a 15-25° draft angle and an integrated set of ejector-pins to facilitate removal of the wick after sintering. The copper base plate is hand-lapped for a flatness of <0.01 mm.

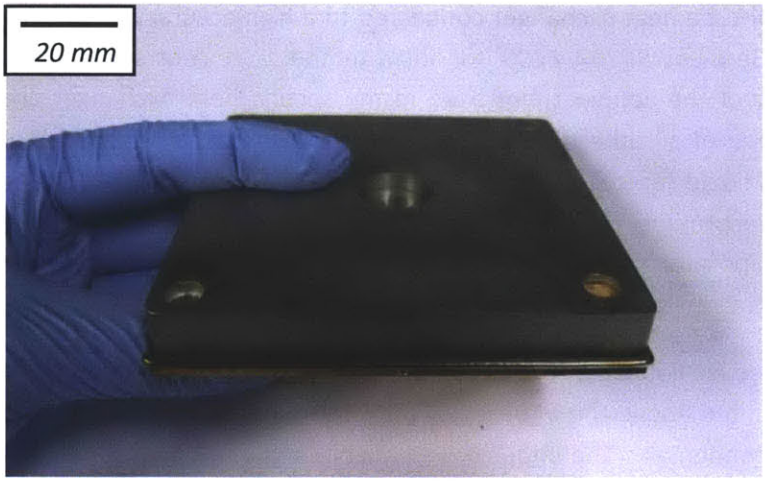

Figure 4.16. Completed evaporator, showing the fusion-welded seam between the Monel 400 case and the copper baseplate.

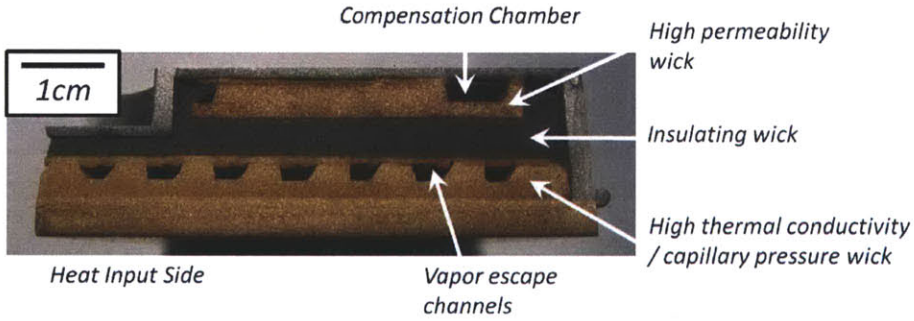

Figure 4.17. Cross sectional cut of a prototypal evaporator. The section shows the bearing insert at the center.

4.7 Evaporator Performance

The evaporator was experimentally tested for the four design requirements. Testing was conducted using two setups. Thermal resistance was measured by applying heat to the evaporator with the vapor ports open to the environment. Water was supplied to the liquid ports manually. The other three requirements of capillary pressure, operation with superheated liquid and regulation of the CC temperature, were tested in a custom loop heat pipe cycle.

4.7.1 Experimental Setup

A custom heat pipe was designed with an integrated throttle valve to adjust the pressure drop through the cycle. The cycle is illustrated schematically in Figure 4.18 and photographs are shown in Figure 4.19. The vapor leaves the evaporator from the two ports, collects into a single pipe, and enters a shell-tube condenser that is cooled by a metered flow of tap water. The inner/outer diameter of the copper vapor piping is 7.90/9.53 mm. The condenser was constructed by concentrically soldering two copper tubes of inner/outer diameters of 14.3/15.8 mm and 11.1/12.7 mm. The condensate flows from the condenser

to another small shell-tube heat exchanger connected to a high-accuracy circulation water bath (Lauda, Lauda Königshofen, Germany *RE207, E200*) for liquid temperature control (sub-cooling or heating). The inner/outer diameter of the copper tubes used in the second heat exchanger are 7.90/9.53 mm and 4.72/6.35 mm; the size of all other liquid piping is 4.72/6.35 mm. The liquid then flows through the throttle valve, past a liquid reservoir, and returns to the evaporator through the two liquid ports. The valve is used to apply a pressure drop to the cycle to stress the capillary meniscus and increase the liquid superheat in the evaporator. The cycle was filled with a custom heat pipe filling station, which is described in Appendix C.

To emulate the convective cooling of the evaporator, a fan impeller was installed above the top surface and a plate was mounted above the impeller to replicate the actual air-flow geometry of the between the evaporator and condenser. The impeller was maintained at an average clearance of 0.6 mm from the evaporator and plate surface. The pressure and temperature measurement locations are shown in Figure 4.18. The liquid and vapor pressures were measured with two pressure transducers (Omegadyne, Sunbury, OH, *PX319-030A5V*), calibrated to an accuracy of 300 Pa. The vapor temperature was measured with a 1.59 mm diameter, 15 mm long T-type thermocouple (Omega Engineering, Stamford, CT, *TMQSS-062U-6*). The evaporator base temperature was measured with a 1 mm diameter, 5 mm long thermistor probe (Redfish, Meridian, ID, *Nano Tube*) with a +/- 0.1 °C interchangeability, inserted into a hole drilled at the side of the copper base. The tap water flow through the condenser was measured by a float-type flow meter (McMaster-Carr, Princeton, NJ, 4351K18) with 3 % accuracy, and the temperatures were monitored with T-type thermocouples (Omega Engineering TC-T-1/8NPT-U-72).

All testing was conducted with the tap water at 11 °C (+/-3 °C) entering the condenser at a metered flow of 1.5 L/min (+/- 0.1 L/min flow oscillation). The fan speed was fixed at 5100 RPM (+/- 100 RPM) and the ambient air temperature was between 22 and 24 °C. Data was collected using a USB data-acquisition board (National Instruments, Austin, TX, *NI USB-6251, SCB-68*) in conjunction with data-acquisition software (National Instruments, *LabVIEW 8.5*). The characteristic curve of the loop heat pipe, showing the vapor temperature dependence on the applied heat load, for these conditions is shown in Figure 4.20.

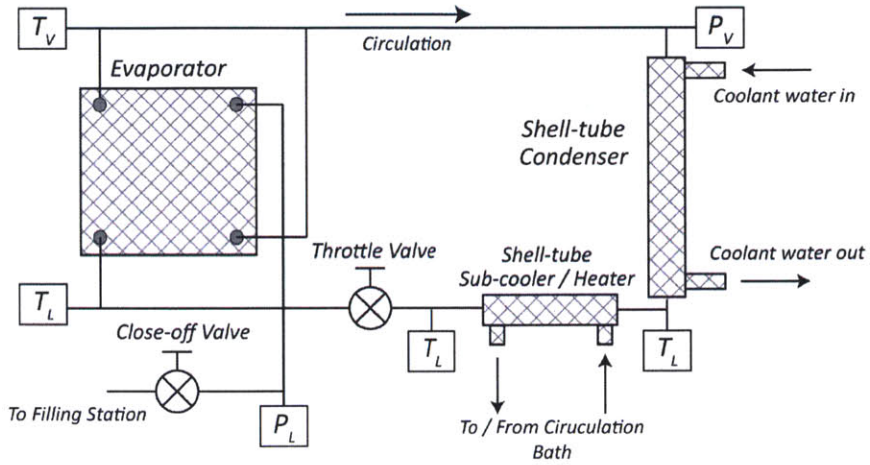

Figure 4.18. Schematic of the heat pipe cycle for evaporator testing

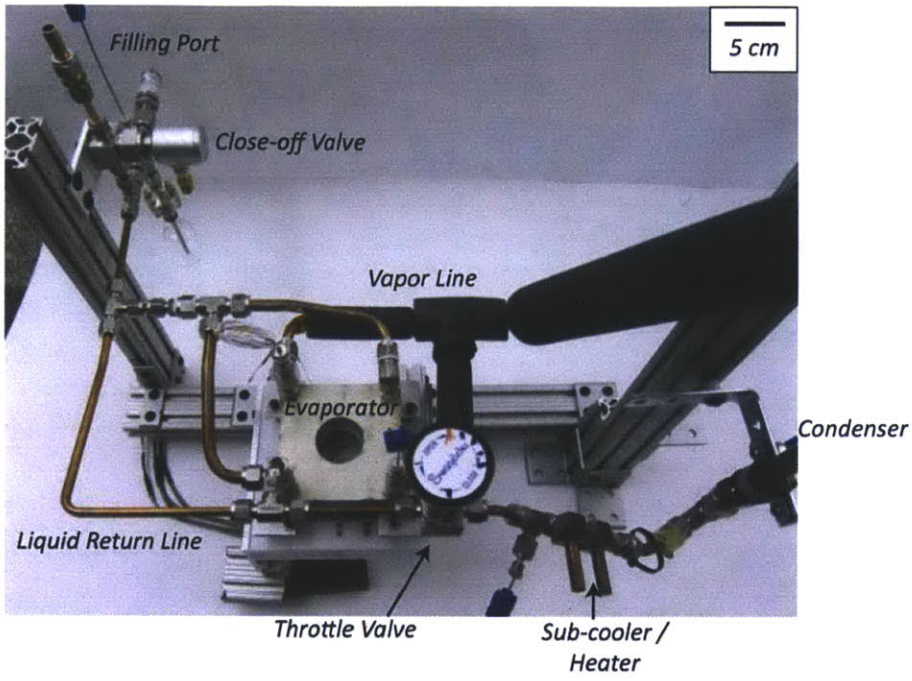

A)

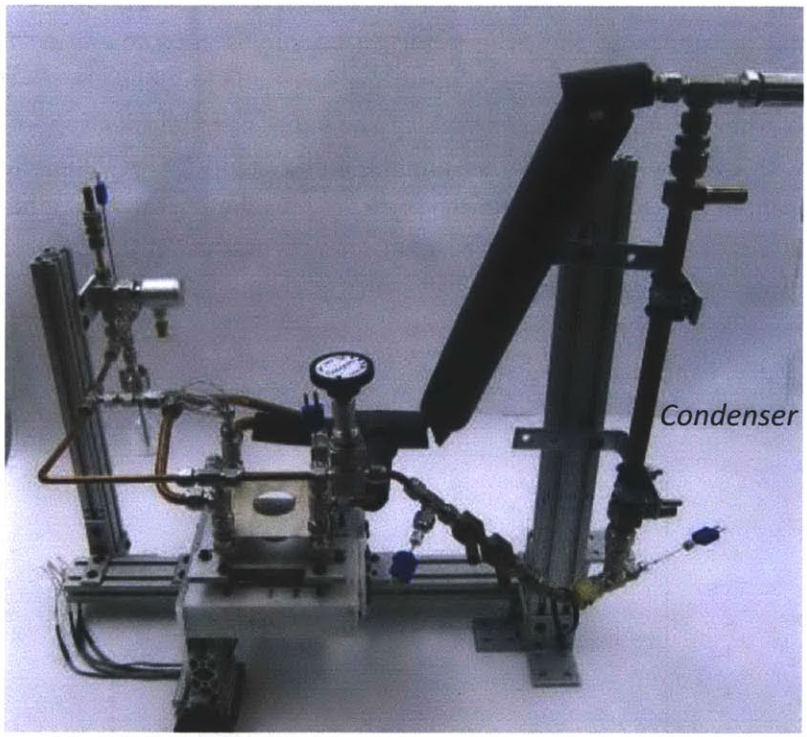

B)

Figure 4.19. Photographs of the heat pipe for evaporator testing. A) shows a labeled top-down view of the components, without the entire condenser, and B) shows the entire cycle. Aluminum framing is used to support the heat pipe.

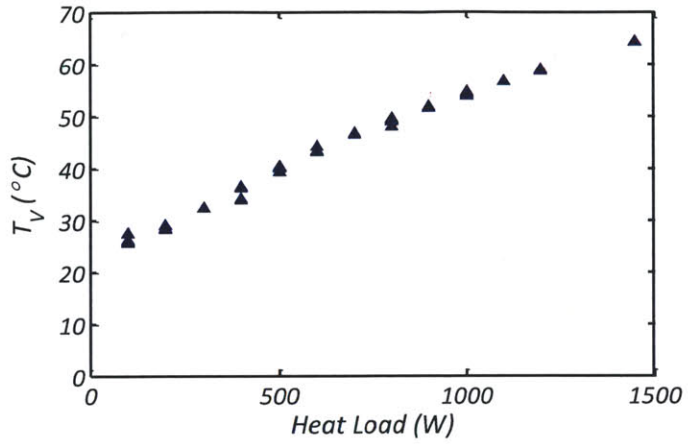

Figure 4.20. Vapor temperature plotted against the heat load to the heat pipe. Measurement error is 0.1 °C.

4.7.2 Thermal Resistance

Figure 4.21 shows the temperature difference between the base and the vapor exiting the evaporator, plotted against the heat load. Both experimental and modeled cases are shown. The slope represents the average thermal resistance of the evaporator. Two curves are shown, of "flooded" and "non-flooded" cases. Flooding occurs when a hydrostatic pressure head is applied to the evaporator by filling the liquid port with a height (4 cm) of liquid water. The vapor channel wick cannot sustain a sufficient capillary pressure with an advancing meniscus, and the liquid drips into the vapor channels. As a result, liquid slugs are present in the vapor channels and pressure must be built to eject the liquid. The ejection of liquid was visually confirmed. The flooded case thus results in a higher temperature difference due to the additional (saturation) pressure drop in the vapor channels. For the non-flooded case, the temperature difference at 1000 W and a vapor temperature of 100 °C is 3.0 °C, and the average thermal resistance is 0.003 °C/W, which agrees with the predictions from the computational modeling at 100 °C.

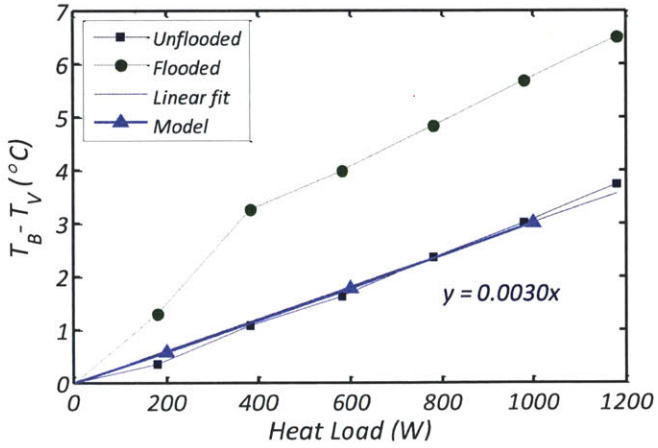

Figure 4.21. Temperature difference between base and vapor exiting the evaporator, plotted against the heat load. Measurement error for the temperature difference is 0.1 °C.

4.7.3 Liquid Superheat and Capillary Pressure

The maximum heat load applicable to the evaporator is limited by dry-out in the wick, which is induced by a high liquid superheat and capillary pressure. Both are caused by low liquid pressure in the wick. Figure 4.22 shows the pressure difference between the vapor and the CC, plotted against heat load. Testing was performed with the heat pipe cycle. Two curves are shown, without throttling and with throttling, where the valve was turned to a set position to increase the flow resistance. A heat removal of 1460 W was demonstrated without throttling. Because the pressure drop through the wick could not be experimentally determined for the particular liquid flow pattern in the evaporator, (*i.e.,* the flow is induced by evaporation across a capillary meniscus, not by an applied pressure gradient) the superheat and capillary pressure were not able to be measured. However, as shown in Figure 4.3E, the pressure difference between the vapor and the CC is directly related to superheat (and capillary pressure), with the effects of the liquid pressure drop through the wick superposed. The liquid superheat and capillary pressure are therefore both greater than the vapor-CC pressure difference shown in Figure 4.22.

The throttled curve confirms that the evaporator can operate with higher vapor-CC pressure differences than those modeled. The pressure difference at 1100 W is 14.8 kPa. In contrast, the highest vapor-CC pressure difference modeled is approximately 12 kPa at a vapor temperature of 77 °C, which is the case with a saturation temperature difference of T_V-T_{CC}=6.5 °C. Furthermore, Figure 4.23 shows that throttling does not result in a dry-out. Dry-out can be identified as an increase in the thermal resistance of the evaporator due the smaller area available for evaporation. The thermal resistance, or the slope of the vapor temperature curve, does not noticeably increase with heat load and therefore does not change with the increase in the vapor-CC pressure difference. The vapor temperature in the throttled case is higher than the non-throttled case due to the higher steady state temperature required to maintain saturation in the CC.

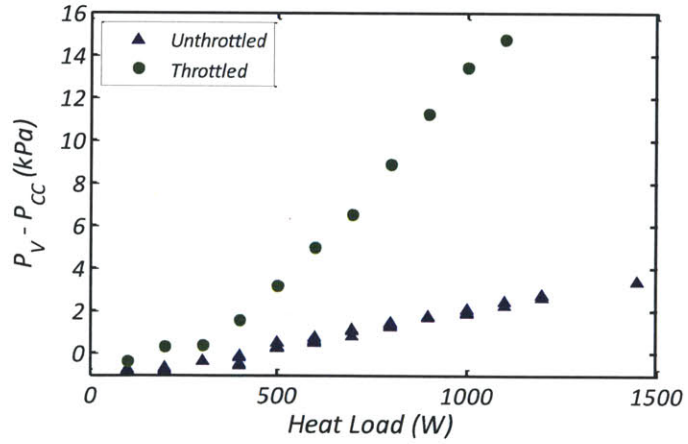

Figure 4.22. Pressure difference between the vapor and the CC, plotted against heat load. Two curves are shown, without throttling and with throttling. Measurement error for the pressure difference is 0.2 kPa.

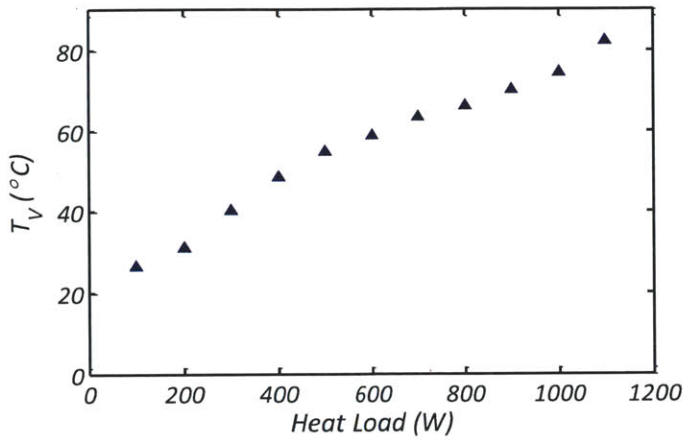

Figure 4.23. Vapor temperature plotted against heat load, for the throttled case. Measurement error for the temperature is 0.4 °C.

4.7.4 Compensation Chamber Temperature

The temperature of the CC was calculated from the liquid pressure at the CC. This calculation required that the CC be maintained at saturation. Furthermore, when the CC is two-phase, the temperature of the vapor-liquid interface of the vapor region determines the saturation pressure [43]. Due to the spatial temperature gradient inside the CC, different saturation pressures may be observed for difference sizes of the vapor region. Experimentation was therefore conducted in a temperature range that resulted in the onset of vapor formation/nucleation in the CC. This ensured that only the hottest temperature in the CC was measured. Since the computationally modeled conditions (multiple condenser heat pipe operation) were not able to be replicated with the test cycle, the measured CC temperatures were compared with those predicted by the model by using the boundary conditions measured in the experiment. The throttle valve was held completely open and the sub-cooler was used cool the liquid returning to the evaporator to room temperature (22-24 °C). This was done to eliminate the temperature measurement error from possible heat transfer to the environment.

Figure 4.24A shows the raw vapor and liquid pressure data for heat loads between 200 and 1000 W, plotted as a function of time. The step increase in heat load causes the pressures to increase accordingly. A salient feature of the pressure trace is the fluctuation in liquid pressure that occurs between 500 and 800 W. The fluctuations are due to the nucleation of vapor in the CC, and this range of heat loads represents the transition between a two-phase CC (<500 W) and a single phase, thermodynamically sub-cooled CC (>800 W). Nucleation was observed as an audible boiling sound during the experiment. The transition can be understood by considering the three mechanisms of heat transfer to the CC, illustrated in Figure 4.1B: 1) the heat inflow from the hot vapor channels and the Monel case, 2) the heat outflow from the convectively cooled evaporator top, and 3) the heat absorbed by the incoming cold (room temperature) liquid. As the heat load is increased, the circulating mass flow increases and the cooling effect of the incoming liquid increases. As a result, although the cycle temperatures increase with heat load, the temperature of the CC becomes relatively cooler and the fluid

in the CC becomes a thermodynamically sub-cooled liquid. The fluctuation of liquid pressure in the transition range is due to a transient cycle similar to boiling. The liquid at the hot-spot on the surface of the high permeability wick becomes superheated, which leads to the nucleation of vapor. The energy required for nucleation is extracted from the hot-spot, cooling it. The vapor pocket transfers the heat to the surrounding liquid and collapses. The cycle repeats upon reheating of the hot-spot.

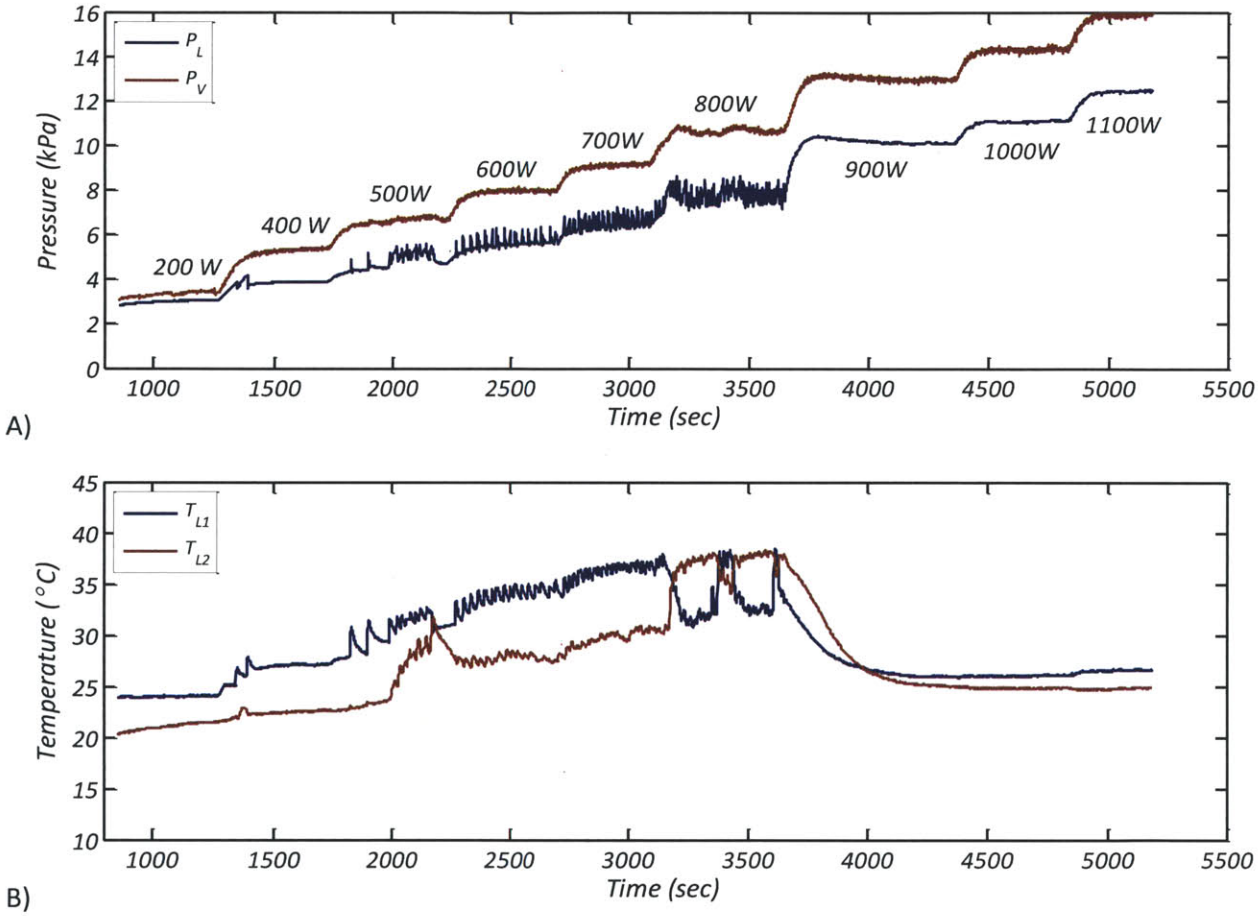

Figure 4.24. Transition from a hot, two-phase CC to a single-phase, sub-cooled CC, showing A) pressure (vapor and liquid) and B) temperature (two liquid ports) traces, plotted against time. The heat load is stepped upwards from 200 to 1100 W during the period shown. Measurement error for the pressures and temperatures are 0.4 kPa and 0.4 °C.

In addition to the pressure traces, the temperature traces of the two liquid ports in Figure 4.24B also indicate vapor nucleation. The liquid port temperatures are smooth at lower heat loads (<500 W) due to the stable existence of a vapor pocket the CC. The vapor pocket behaves like a local thermosyphon, in which evaporation occurs from the surface of the high permeability wick and condensation at the liquid-vapor interface of the vapor pocket. A high effective thermal conductivity is achieved in this pocket and the liquid port closer to the pocket is heated, causing unequal liquid port temperatures. Despite this heating, the liquid port temperatures are generally low at these heat loads due to the low heat pipe temperatures (Figure 4.20). A similar behavior continues as the heat load is increased to the transition range, except the stable vapor pocket is replaced by an intermittent nucleation site. A temperature

fluctuation occurs as the nucleation of the vapor pocket pushes hot liquid towards the thermocouple in the liquid port and the collapse of the vapor pocket retracts cooler, upstream liquid towards the thermocouple. While one liquid port is generally higher in temperature than the other, the particular port changes due to the change in location of the hot-spot. This is possible due to the symmetric design of the evaporator. At higher heat loads, the CC is single phase and the thermosyphon behavior is absent. The liquid port temperatures are thus much lower than the vapor temperature.

The saturation temperature was calculated for the average peak pressures of the liquid pressure fluctuations. Figure 4.25 shows the difference between the vapor and calculated CC temperatures, plotted against the vapor temperature. The vapor temperature is plotted in the abscissa because it is the primary driver for the heat transfer to the CC. However, the heat load also affects the CC temperature through the mechanisms mentioned above and is therefore indicated in the figure as well. The results of the model using the experimental boundary conditions are also shown in Figure 4.25 as a dotted line. The boundary conditions include the heat load, the measured vapor and incoming liquid temperatures, and the expected convective heat transfer coefficients at the evaporator top (100 W/m^2-K) and sides (20 W/m^2-K). The temperature difference between the vapor and the CC increases as the vapor temperature increases, since a greater conductive heat transfer occurs between the vapor and CC across a constant wick thermal resistance. The model results match well with the experimentally measured temperature difference between the vapor and the CC, signifying a successful implementation of the computationally developed design.

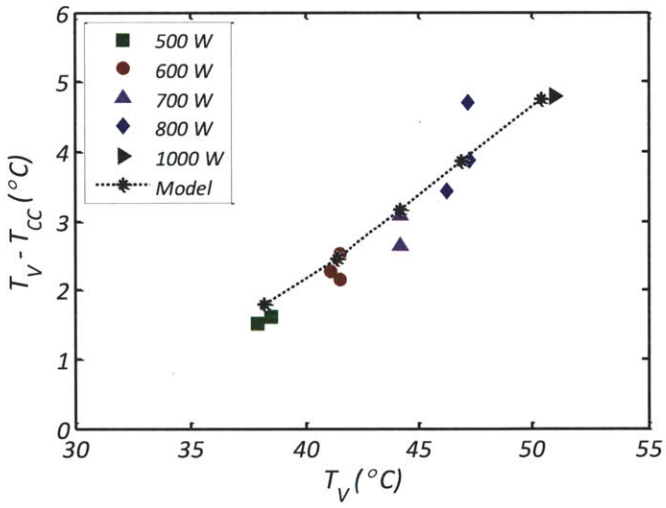

Figure 4.25. Temperature difference between the vapor and the CC, plotted against the vapor temperatures. The heat loads corresponding to the vapor temperatures are also shown. The plot shows both experimentally measured (points) and computationally modeled (line) data. Modeling was performed with experimentally measured boundary conditions. Measurement error for the temperature difference between the vapor and CC is 0.2 °C; error for the vapor temperature measurement is 0.4 °C.

4.8 Summary

A planar evaporator was developed for the integration into a multiple-condenser heat pipe. The evaporator was designed with the four goals of: 1) providing sufficient capillary pressure, 2) operation with superheated liquid, 3) low thermal resistance, and 4) operation with a prescribed CC temperature. A multi-layer wicking structure was designed using two and three-dimensional computational modeling with the desired capillary pressures, thermal conductivites and permeabilities. Subsequently, the design was fabricated by a series of sintering steps to manufacture a monolithic wicking structure integrated into the evaporator case. The evaporator was then tested with consideration of the four goals. Successful operation was observed up to 1460 W and a capillary pressure and liquid superheat greater than 14 kPa was achieved, which exceed the requirements for integration in the multiple-condenser heat pipe. The thermal resistance was observed to be dependent on the presence of liquid in the vapor channels. When the channels were completely cleared of liquid, the thermal resistance at a vapor temperature of 100 °C was measured to be 0.003 °C/W, matching the model predictions. The hottest temperature in the CC was also experimentally measured to match with the model predictions using the experimental boundary conditions. In conclusion, the evaporator was designed, fabricated and experimentally tested to meet the design criteria for integration into a multiple condenser heat pipe. An integration of the evaporator with a condenser for an air-cooled, single-condenser prototype follows in Chapter 5.

(This page intentionally left blank)

5 The Single-Condenser Prototype Heat Pipe

5.1 Overview

The evaporator and condenser were integrated into a single condenser heat pipe to confirm the operation of the heat pipe cycle with phase separation in the condenser. This prototype heat sink will be referred as the "Single-Condenser Prototype" (SCP), representing an intermediate step towards the multiple-condenser heat pipe. The SCP was operated as both LHP and CPL, and depending on the operating mode, various levels of liquid and vapor pressure control were demonstrated. This chapter begins with a description of the thermal-fluidic cycle of the heat pipe and follows with a comparison of conventional LHPs and CPLs to the SCP. The experimental apparatus is then described, and the characterization of the LHP and CPL modes are presented. The LHP mode is analyzed for total thermal resistance and phase separation in the condenser. The effects of the filling volume on the heat pipe performance are also evaluated. The use of the reservoir for liquid and vapor pressure control in CPL mode is investigated for fulfilling the requirement of Equation 2.29 as well as for active temperature control of the heat pipe. The understanding of the operating modes gained from this study is used as the basis for characterizing the multiple-condenser heat pipe in the following chapter.

5.2 Thermal-fluidic Cycle

The thermal-fluidic cycle of the SCP is illustrated in Figure 5.1 and the temperatures and pressures of the cycle are shown schematically relative to the saturation curve in Figure 5.2. The effect of gravity is neglected in Figure 5.2 due to the small height difference between the evaporator and condenser.

Heat applied to the evaporator base is conducted to the vapor channels, where evaporation takes place (1). The vapor exits the evaporator through the vapor channels and enters the condenser (2) through the two vapor lines. The vapor is convectively cooled and condenses onto the surface of a wicking structure that lines the inner surface of the condenser (2). A pressure differential exists across the meniscus formed on the condenser wick, and this meniscus separates the vapor and liquid phases. Upon condensation, the liquid enters the wick (3) and is sub-cooled as it flows from the condensation space to the liquid channels (4). After exiting the condenser, the liquid enters the two liquid lines and returns to the evaporator. The liquid enters the evaporator CC, which is at saturation (two-phase) (5) for LHP operation. From the CC, the liquid flows through the evaporator wick to the vapor channels, where the cycle repeats (6).

A separate reservoir is connected to the liquid lines to allow operation as a CPL. During LHP operation the reservoir is a non-circulating, extra volume of liquid. When the reservoir is heated to a temperature greater than that of the CC, the reservoir becomes the hottest location in the liquid-side of the heat pipe and saturation is relocated to the reservoir. In the discussion that follows, LHP will refer to the heat pipe

operation with saturation in the CC, and CPL will refer to operation with saturation in the reservoir. Additionally, this location of saturation will be referred to as the "two-phase region." It is important to note that by operating the SCP as a CPL, the capillary pressure in the condenser is decreased. This can be seen in Figure 5.2 as decrease in the pressure difference between (2) and (3).

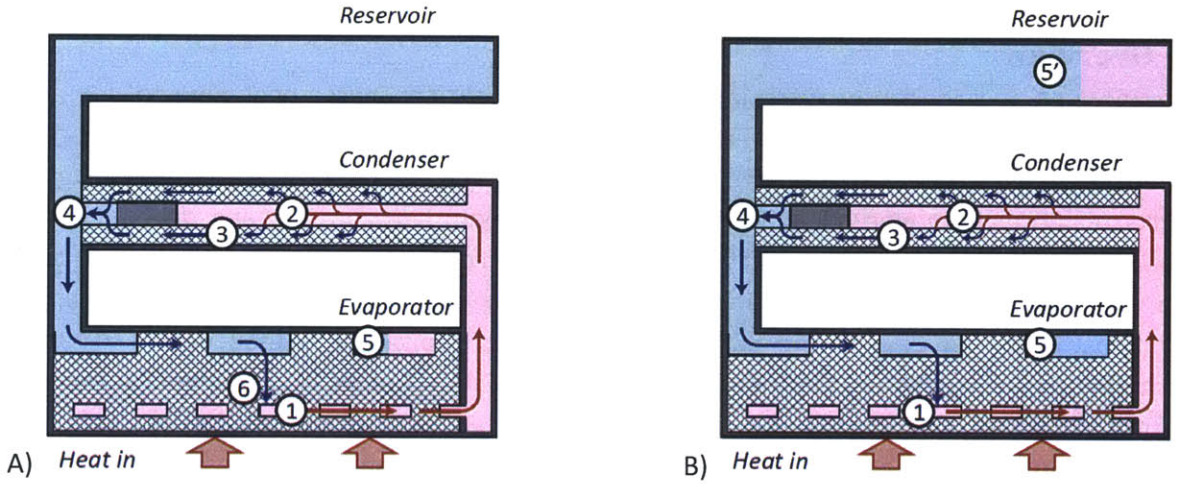

Figure 5.1 Schematic of the heat pipe cycle. The illustration shows the two-phase region in A) the CC for the LHP cycle, and B) the reservoir for the CPL cycle. Pink and light blue regions indicate vapor and liquid, respectively. The hatched sections indicate the wicks.

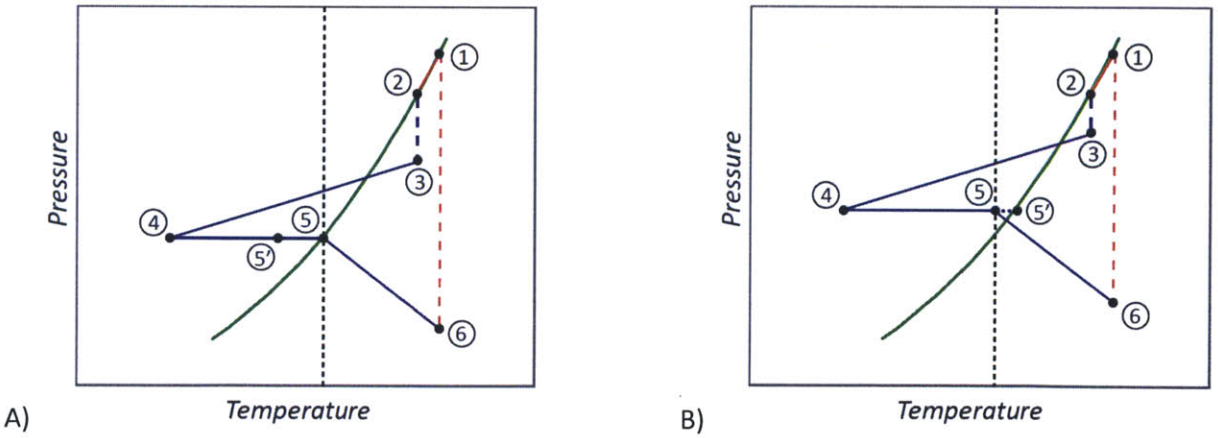

Figure 5.2 Schematic of the pressure and temperature states of the cycle. The green curve indicates the saturation curve, and red and blue traces indicate the vapor and liquid phases, respectively. The dashed portions represent the capillary pressure differentials. A) LHP operation, with the reservoir temperature below that of the CC. B) CPL operation, with the reservoir temperature above that of the CC.

In addition to the LHP cycle, the CPL cycle is characterized for two reasons. The first is to investigate the viability in using an actively heated reservoir for liquid pressure control, to decrease the condenser capillary pressure. This will give insight into the possible use of a condenser with lower maximum

capillary pressure, simplifying the manufacturing tolerances of the condensers. The second is to evaluate the effectiveness of the reservoir in raising the heat pipe temperature by deliberately flooding the condenser. Flooding is accomplished by increasing the reservoir temperature beyond the limits of Equation 2.29. This will allow operator control of the heat pipe temperature, which can be used to prevent the over-cooling of temperature-sensitive heat sources. Thus the CPL cycle is tested for two modes: 1) for heat pipe operation with a capillary pressure in the condenser, similar to the LHP cycle, for low thermal resistance (liquid pressure control); and 2) for operation with a flooded condenser to actively increase the thermal resistance in a controlled manner (vapor pressure / temperature control).

5.3 Comparison with Traditional LHPs

It is worthwhile to note the differences between the SCP and LHPs documented in literature. Besides the differences in the geometry and configuration of the heat pipe, fundamental differences exist in the operating characteristics. To describe the differences, it is useful to understand the operating characteristics of LHPs with non-wicked condensers.

Tubular, non-wicked, condensers commonly found in LHPs allow movement of the vapor-liquid interface depending on the operating condition. Most heat pipe studies in the past two decades have been performed with the condenser sink temperature below that of the ambient, with two operating modes observed – "variable" and "fixed" conduction, depending on the conductance (resistance) of the heat pipe [32, 33, 35, 53]. The condenser sink temperature is typically defined as the temperature of the (cooling) fluid that exchanges heat with the condenser. The two modes are shown in Figure 5.3 as a difference in the temperature response to a varying heat load. The curved region at lower heat loads represents the variable conductance mode, and the constant slope region at higher heat loads represents the fixed conduction mode.

When operating in the variable conductance mode, the low heat load results in the liquid-vapor interface occurring early in the length of the condenser tube, whereas higher heat loads push the interface to occur towards the end of the condenser length [33, 35]. A characteristic of the variable conductance mode is the sub-ambient vapor temperature, which is between the ambient and condenser sink temperatures [32, 33, 35, 43]. Due to the sub-ambient vapor temperature, heat transfer occurs from the ambient to the condenser sink though the heat pipe. Specifically, heat is transferred from the ambient into the liquid lines. It follows that the heat pipe has a higher heat load than that applied to the evaporator due to the additional heat transfer with the hotter ambient. The change in this added heat load results in the change in conductance, which is afforded by the movement of the liquid-vapor interface in the condenser. The movement changes the area available for condensation and thus the utilization of the condenser, and is compensated in the two-phase CC through the expansion and shrinking of the vapor in the two-phase region. The lowest vapor temperature is reached and the conductance is maximized when the evaporator heat load is increased such that the heat transfer from the ambient constitutes a smaller fraction of the total heat load and the higher heat load requires the full utilization of the condenser. This operating point is the inception of the fixed conduction mode.

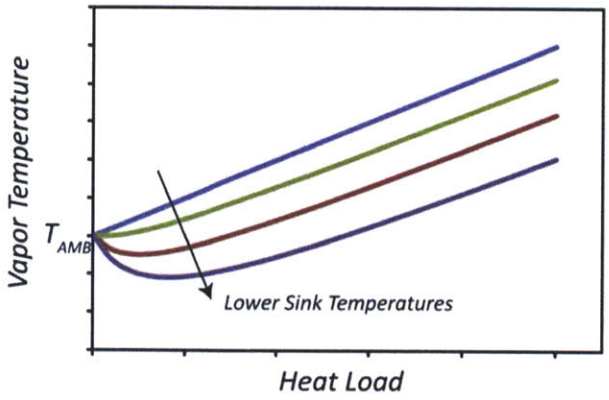

Figure 5.3. Vapor temperature schematically plotted against heat load for different condenser wick temperatures, for a LHP with a non-wicked condenser. The curved region at lower heat loads indicates the variable conduction mode, with the constant slope region the fixed conduction mode.

In the fixed conductance mode, the vapor-liquid interface occurs at the end of the condenser. The condensation area is at the maximum and is fixed, resulting in a near-linear increase in vapor temperature with an increase in heat load. For a well-designed LHP with negligible thermal and fluidic resistances in the evaporator and vapor lines, the condenser is the limiting thermal resistance in the fixed conductance mode. When the condenser sink temperature is equal to or higher than that of the ambient, the only operational mode is fixed conduction [33, 35, 37]. The heat pipe only operates with a vapor temperature higher than that of the ambient, preventing the additional heat load from the ambient described above. As a result, the lowest possible vapor temperature is that of the condenser sink temperature, which occurs at the onset of heat pipe startup.

For the air-cooled case presented here, the condenser sink and ambient temperatures are equal. The heat pipe is permanently in the fixed conduction mode, and the maximum area available for condensation is utilized [33, 35]. The SCP design takes advantage of this mode by fixing the maximum condensation area by integrating a wick, thus ensuring that condensation occurs on the wick meniscus and phase separation is achieved. Furthermore, air-cooled operation and fixing the condensation space in the fixed conduction mode is expected to prevent possible temperature oscillations and unstable operation [67-69]. To maintain a receding meniscus in the condenser, the SCP is designed with a two-phase region in the CC at a temperature defined by Equation 2.29 for liquid pressure modulation. While previous work on characterizing LHPs with a wick integrated in the condenser has been documented, testing were performed with the condenser sink temperature lower than that of the environment, and vapor and liquid pressure control measures were not documented. As a result, the LHP was found to operate with a flooded condenser [70].

5.4 Comparison with Traditional CPLs

For understanding the operational characteristics of the SCP as a CPL, it is useful to compare the operation of the SCP to that of a traditional CPL. Operational differences can be expected due to the sizing of the reservoir and the integration of a wick in the condenser. The following discussion will assume negligible height difference between the reservoir and condenser and negligible viscous pressure drop in the liquid flow.

5.4.1 Reservoir

The reservoir is typically sized in CPLs to ensure that it contains liquid for all possible operating conditions, and therefore is of a volume comparable to the volume of the remainder of the heat pipe [32]. However, when not in operation, it is common for CPLs to lose liquid from the heat pipe section to the large reservoir and therefore require a priming procedure prior to startup [32, 34]. Priming typically consists of heating the reservoir before heating the evaporator to send liquid from the pressurized reservoir into the heat pipe section. This priming procedure can require several hours, depending on the size of the heat pipe. In contrast, the reservoir in the SCP is substantially smaller in volume (8.9 mL) compared to the volume of the rest of the heat pipe (89.1 mL), and is similar to the volume of the evaporator CC (5.6 mL). While this results in the risk of losing liquid in the reservoir when the heat pipe is not in operation, no priming is necessary upon startup, as heat input to the evaporator immediately returns the liquid to the reservoir. Furthermore, similar volumes of the reservoir and CC allow the heat pipe to operate as both a LHP as well as a CPL, since a vapor volume that is appropriate for the evaporator CC (LHP) will automatically be appropriate in size for the reservoir (CPL).

When operating as a CPL, the reservoir is used to control the liquid pressure in the SCP. Setting the reservoir temperature sets the saturation pressure, which determines the liquid pressure of the heat pipe. Since the liquid pressure is separated from the vapor pressures by the evaporator and condenser wick menisci when Equation 2.29 is met, the liquid pressure can be expected to be adjusted separately of the vapor pressure. This effect is in contrast to the reservoir setting the vapor temperature and pressure in conventional CPLs [32, 34, 52].

5.4.2 Condenser Operation - Variable and Fixed Conductance

Similar to the operation of LHPs, that of CPLs with non-wicked condensers can be categorized into two modes, variable and fixed conductance, although the characteristics are different [32, 34]. Variable conductance occurs when the reservoir is heated to a temperature such that it is two-phase, and is therefore high enough to set the operating (vapor) temperature and pressure of the heat pipe. The temperature set at the reservoir can be considered to artificially "drive up" the operating vapor temperature. The condensation area and the location of the vapor-liquid interface in the condenser adjust to allow the heat pipe to operate at the temperature set by the reservoir. As a result, the condenser space/area is not fully utilized, and the heat pipe exhibits a variable conductance (resistance). Consequently, in variable conductance mode, the vapor temperature is fixed regardless of the heat load (Figure 5.4). The volume change for the movement of the vapor-liquid interface in the condenser is compensated by the expansion and contraction of the vapor region in the two-phase reservoir. However, once a critical heat load is exceeded, the full utilization of the condenser is required, and the CPL enters the fixed conduction mode.

In LHPs, fixed conduction is the result of the heat load reaching a threshold that requires the full utilization of the condenser area, and this mode can also occur in CPLs if warranted by the design. In the CPL, fixed conduction can occur when the required vapor temperature for removing the heat load exceeds the temperature set at the reservoir (Figure 5.4). Alternatively, fixed conduction can occur at a given heat load by decreasing the reservoir temperature so that the reservoir is no longer artificially driving up the vapor temperature. The resulting behavior is the same for LHPs and CPLs: the

condensation space/area is maximized, and an increase in the heat load translates to a linear increase in vapor temperature. Full utilization of the condenser minimizes the thermal resistance. However, in the CPL, when the vapor temperature exceeds that of the reservoir, the two-phase region of the reservoir collapses, becoming a thermodynamically sub-cooled liquid at the pressure set by the vapor. The vapor region in the reservoir is transferred to the condenser; if this volume is too large, not only will the condenser be completely filled with vapor, but vapor may also become present in the liquid lines and the evaporator CC. Fixed conductance will occur in CHPs when such operation is possible, or when the vapor volume in the two-phase region is sized to be small enough that relocation of the vapor from the reservoir to the condenser does not fill the remainder of the heat pipe with excess vapor [32]. The ideal design point is for the vapor relocation to result exactly in the full utilization of the condenser area.

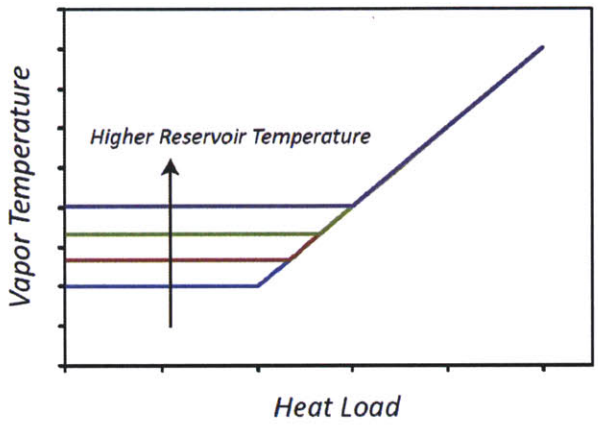

Figure 5.4. Effect of reservoir temperature on the vapor temperature plotted against the heat load. The reservoir temperature affects the variable conductance regime, shown as the horizontal section with set vapor temperature.

The SCP also operates with variable and fixed conduction modes, although the operational characteristics of the reservoir differ from that of a CPL with a non-wicked condenser. When the reservoir is heated to the temperature range established by Equation 2.29, the reservoir is two-phase. In contrast to traditional CPLs, a two-phase reservoir does not result in variable conductance; the condensation behavior is unaffected by the reservoir due to the pressure discontinuity at the condenser wick, and occurs in the same manner as in fixed conduction. Likewise, the difference in the liquid and vapor pressures prevent the two-phase region in the reservoir from collapsing despite operating in the fixed conduction mode, ensuring reservoir control of the liquid pressure. The size of the vapor region in the reservoir is determined when the heat pipe is initially charged with the working fluid by under-filling the liquid space of the heat pipe by a prescribed amount. When the reservoir temperature is too low to maintain saturation in the SCP, the vapor from the reservoir does not collapse, but is instead relocated to the CC for operation in the fixed conduction mode as a LHP. The relocation is a controlled process, as the vapor is fully contained in both reservoir and CC.

When the reservoir is heated to a temperature beyond the limits set by Equation 2.29, a pressure discontinuity will no longer be maintained across the condenser wick due to the high reservoir pressure, and the reservoir pressure will directly communicate with that of the vapor. In this case, the SCP will observe the characteristics of variable conductance operation of traditional CPLs shown in Figure 5.4,

and the reservoir temperature and pressure will roughly equal the vapor temperature and pressure. Hence the integration of a wick in the condenser allows for liquid pressure control in fixed conduction mode and vapor pressure control in variable conductance mode.

5.5 Experimental Apparatus

The SCP was constructed by integrating of the motor and fan assembly into a single condenser heat pipe. Figure 5.5A shows the SCP. The heat pipe consists of the evaporator, condenser and reservoir. For material compatibility with water the heat pipe was constructed using copper and Monel 400 [60-63]. The condenser and reservoir designs will be briefly described in order to understand the operation of the heat pipe. A more detailed description of the condenser design and development can be found in [66].

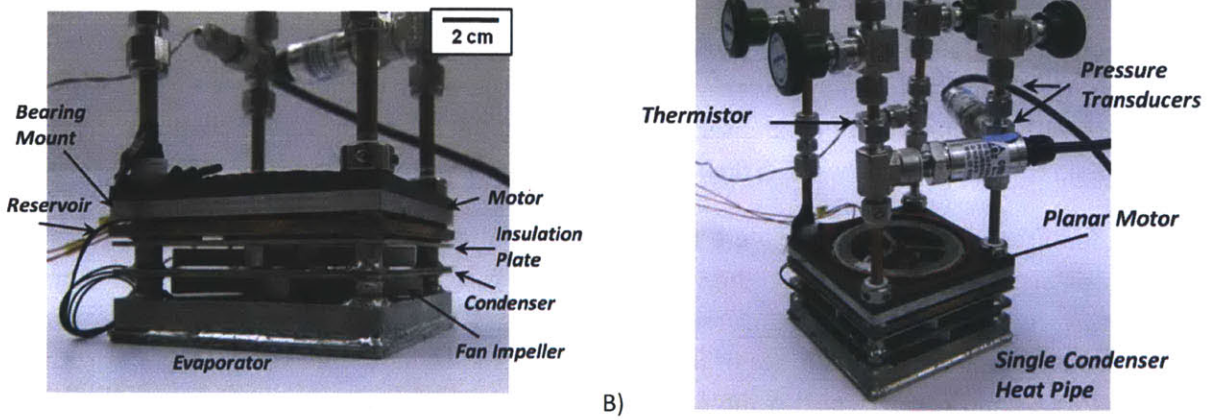

Figure 5.5. A) Single-condenser prototype. B) Single-condenser prototype with instrumented filling manifold. Testing was performed with the manifold attached.

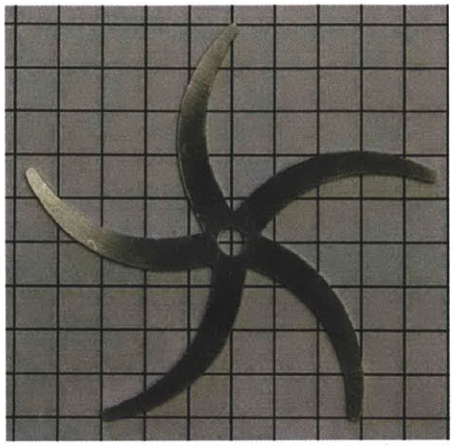

Figure 5.6. Impeller profile [30]. The grid spacing is 10 mm.

5.5.1 Condenser

The condenser was designed as a square plate to utilize the maximum footprint area available (101.6 mm x 101.6 mm). To reduce the volume occupied for a given condenser surface area, a thin geometry was adopted (2.5 mm). Two vapor and two liquid ports are located symmetrically at the corners allow transport of the fluid while avoiding obstruction of the rotating fan impellers. The configuration of the four ports allows each condenser to be inserted onto the four fluid tubes that extend from the evaporator. The condenser can therefore be made independently of the evaporator and stacked, with the number of condensers determined by the heat removal requirement. A circular hole is made in the center to allow for a flow path of the cooling air.

The inside features of the condenser were designed through thermal-fluidic modeling to: 1) maximize the area available for condensation *via* the wick and 2) integrate a sub-cooler that sufficiently cools the condensate to meet Equation 2.34 .. The flow pattern is shown in Figure 5.7 and the expected temperature profile of the outer surface of the condenser is shown in Figure 5.8. The vapor ports access the central, wick-lined region which is the condensation space. This hot, vapor space is maximized by locating the vapor-liquid partition near the edges of the square. The liquid region is a narrow channel that collects the condensate and directs it towards the liquid exit port. The flow of condensate inside the wick is therefore radial, resembling the flow pattern shown in Figure 5.1. Sub-cooling is achieved as the condensate flows across the partition. While the condensation space is isothermal at approximately the vapor temperature, a thermal gradient is observed across the partition, which behaves as a fin with a base at the vapor temperature. The partition length determines the level of sub-cooling. This general layout is similar to that modeled in Chapter 3, except the shape of the sub-cooling section has been modified to increase the area available for condensation. Modeling was performed for vapor and inlet air temperatures of 77.5 °C and 30 °C, respectively, and a convective boundary condition of 146 W/m^2K, which is expected for a fan speed of 5000 RPM [30]. The thermal conductivities of the wick and metallic frame are 2.4 and 25 W/m-K, respectively. Thermal modeling was performed with COMSOL Multiphysics. Due to the use of a thin frame and wick, the temperature drop across the condenser body in the condensation area is small (0.6-2.5 °C).

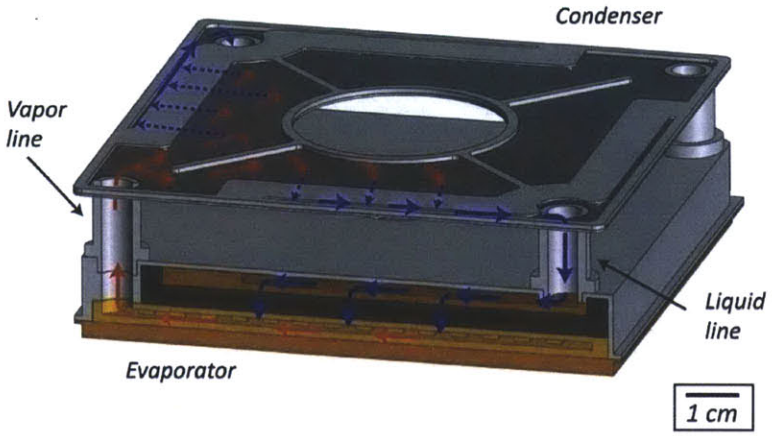

Figure 5.7. Circulation pattern in the SCP. The internal features are shown by taking cross sections of the evaporator, condenser and tubes. The reservoir observes no net mass flow and is therefore omitted in this diagram. The red and blue arrows indicate vapor and liquid flows, respectively. The dotted and dashed lines indicate the flow through the wicking structures. The figure shows how the condenser is inserted onto the four tubes. Illustration is to scale.

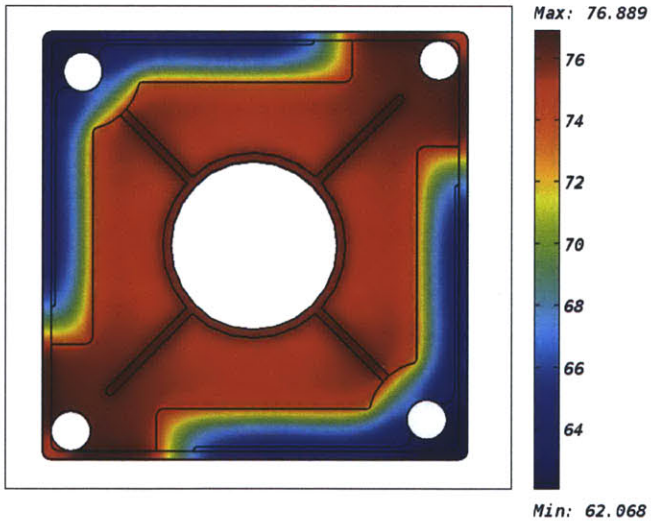

Figure 5.8. Expected temperatures of the outer surface of the condenser. The figure shows the features for half of a condenser. Total heat removed per condenser face is 61.5 W for the modeled conditions.

The condenser was fabricated as two identical halves, which are combined to complete the condenser. Figure 5.9 shows half of the condenser. Each half is constructed by sintering onto a photochemically etched Monel 400 case of 0.5 mm thickness. The wick (0.5 mm thickness) covers the entire inner surface of the condenser, and the vapor-liquid partition is shown as a solid structure on the surface of the wick. A commercially available, non-spherical Monel 400 powder with a mixed particle size of less

than 44 μm (Table 3.1) is used to fabricate the wick. The total internal volume of the condenser is 6.2 mL, with 2.6 mL in the vapor/condensation space.

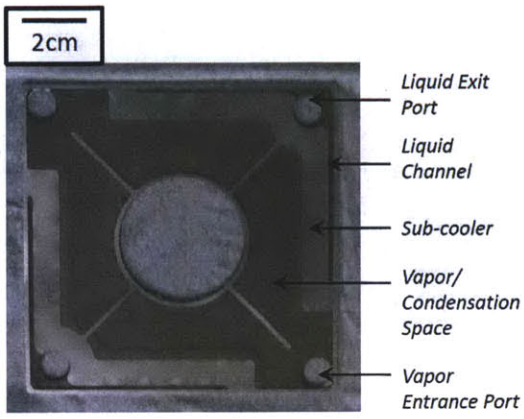

Figure 5.9. Photograph showing the symmetric half of a condenser. The dark grey section is the wick lining.

5.5.2 Reservoir

The reservoir was designed as an additional planar component that could be installed in a similar manner as the condenser (Figure 5.10). Like the condenser, a central hole in the reservoir allows for a flow passage for the cooling air. A 6.35 mm thick copper plate was milled to produce a uniform array of pillars in the inner cavity. The pillars are 2 mm x 2mm in area and 2 mm in height, spaced 2 mm apart. Copper pillars are used to maintain temperature uniformity. The cavity in the copper plate was closed with a 0.5 mm thick Monel 400 plate using a silver braze. While the reservoir has four holes for vapor and liquid line insertion, the inner cavity is connected only to the liquid lines. As designed, the volume of the inner cavity is 8.9 mL.

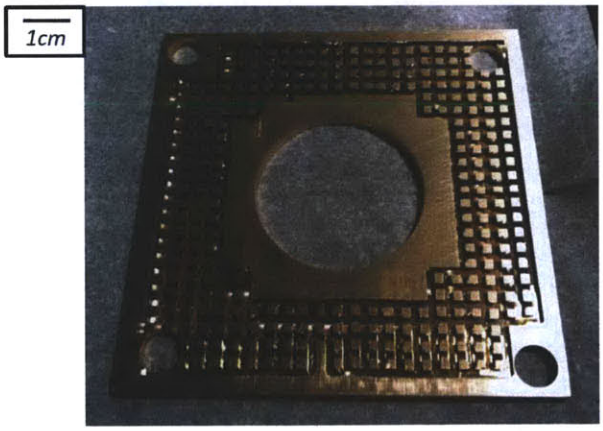

Figure 5.10. Milled copper plate for the reservoir.

The reservoir was installed above the condenser, against the topmost fan impeller. To prevent excessive convective cooling of the reservoir, an aluminum plate was placed between the reservoir and the fan impeller and aerogel insulation was placed between the aluminum plate and reservoir (Figure

5.5A). Heating was performed with two 50.8 mm x 25.4 mm polyimide heaters (McMaster-Carr, Princeton, NJ, *35475K423*).

5.5.3 Single Condenser Prototype

Figure 5.5 shows the SCP, which consists of the single condenser heat pipe, fan assembly and the filling manifold. The condenser and reservoir were brazed (72 % Cu / 28 % Ag) to the liquid and vapor lines, and this assembly was subsequently brazed (80% Ag / 20% Sn) to the evaporator. These brazes were selected such that the brazing temperature does not exceed the previous sintering temperatures in the evaporator and condenser. A custom jig was used in during brazing to correctly align the components. Machined Monel 400 tubes of inner/outer diameter of 9.53/6.35 mm were used for the lines. The braze was observed to incompletely fill the joints. The gaps from the brazing process were filled by soldering (63 % Sn / 37 % Pb). After the soldering process, the seal was measured with a helium leak detector to be 10^{-7} standard cm^3/ sec. The total volume of the heat pipe was calculated to be 88.1 mL, with a liquid space volume of 75 mL.

Like the condenser and reservoir, four holes were made at the corners of the motor and the bearing mount for the impeller shaft. The fan assembly was installed into the heat pipe by first inserting the lower bearing into the evaporator frame. Two impellers were then fit into place, one above the condenser and another below, and shimmed for clearance. Figure 5.6 shows the geometry and size of the impeller. The shaft was inserted through the impellers and into the lower bearing, and the impellers were epoxied in place. The top bearing was then pressed onto the shaft, and installed with the bearing mount onto the four fluid lines. Lastly, the motor was attached to the shaft and fixed to the four lines. After the epoxy was cured, the shims were removed from the impellers and free rotation was confirmed. The four fluid lines were thus the basis of locating the fan assembly. The impellers are 6.93 mm in thickness with an average clearance of 0.5 mm from each heat transfer surface. The profile of the impeller is shown in Figure 5.6.

A four-pronged filling manifold was made from copper tubing and compression tube connectors to mate the SCP to a heat pipe filling station. The SCP with the manifold is shown in Figure 5.5B. The filling manifold was instrumented with sensors and attached to the four pipes that extended from the SCP. The liquid and vapor pressures were measured with two pressure transducers (Omegadyne, Sunbury, OH, *PX309-030A5V*), calibrated to an accuracy of 300 Pa. The vapor temperature was measured with a 3.18 mm diameter thermistor probe with a +/- 0.2 °C interchangeability (Omega Engineering, Stamford, CT, *TH-10-44006-1/8-2-40*). The transducers and thermistor were mounted onto the manifold instead of the heat pipe to avoid disrupting the geometry of the heat pipe. The liquid pressure measurements were taken 82 mm above the compensation chamber, 100 mm above the condenser, and 112 mm above the CC in the evaporator. The liquid pressures at the respective locations were calculated by the addition of a gravitational pressure head to the pressure measured. The temperature of the reservoir was measured using a 1 mm diameter, 5 mm long thermistor probe (Redfish, Meridian, ID, *Nano Tube*) with a +/- 0.1 °C interchangeability. The thermistor was attached using polyimide tape and a silver-based thermal paste (AiT, Princeton Junction, NJ, *Cool Silver*). The ambient air and the surface temperatures of the liquid and vapor lines were measured with a type-T thermocouple (Omega Engineering, *5TC-TT-T-40-36*).

The heat load was applied to the evaporator by a copper heater block (101.6 mm x 101.6 mm footprint, 15.9 mm thickness) with four 48 ohm cartridge heaters (6.35 mm diameter, 76.2 mm length) (McMaster-Carr, Princeton, NJ, *35025K133*). The heater block was insulated by a 25.4 mm thick PTFE case.

The pressure and temperature measurements were logged using a USB data-acquisition board (National Instruments, Austin, TX, *NI USB-6251, SCB-68*) in conjunction with data-acquisition/controls software (National Instruments, *LabVIEW 8.5*). Heater control for the reservoir temperature control was executed with the same software. The layout of the instrumentation and data-acquisition is shown in Figure 5.11.

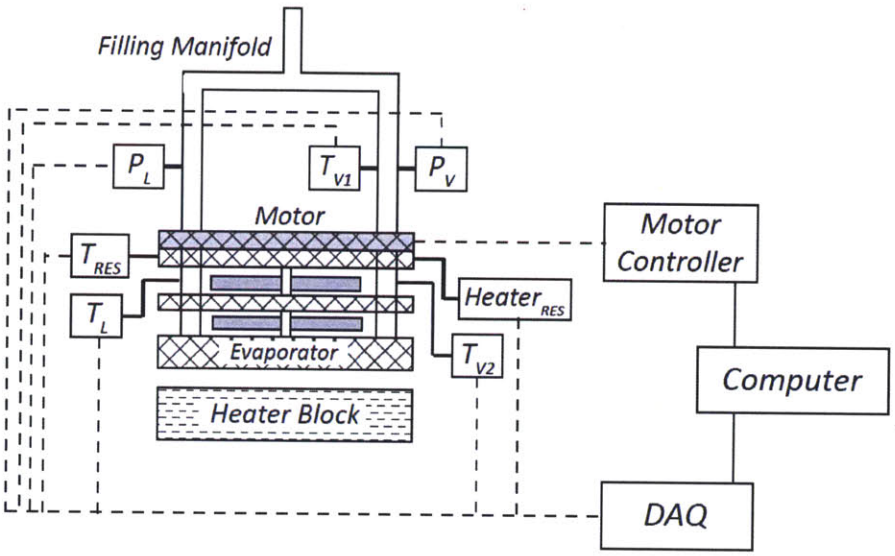

Figure 5.11. Schematic of experimental instrumentation and data acquisition layout. The routing for power supply is not shown.

5.5.4 Test Parameters

The characterization of the SCP was performed in two parts, by analyzing the operation as a LHP and as a CPL. Specifically, the following were investigated:

LHP Operation:

1. Thermal resistance from the heat pipe vapor temperature to the ambient air temperature
2. Phase separation in the condenser
3. Effects of the filling volume on heat pipe performance

CPL Operation

4. Effect of the reservoir temperature on the liquid pressure
5. Effect of the reservoir temperature on the vapor pressure

The liquid and vapor pressures were the primary measurements of the experiments, and allowed the characterization of the state of the condenser wick meniscus. Due to the thin condenser body, the

vapor temperature inside the condenser was estimated to be the condenser surface temperature; the thermal resistance of the heat sink was therefore calculated using the vapor and ambient air temperatures.

The LHP operation was tested by adjusting the heat load to the evaporator, the fan speed, and filling volume. The heat load was swept from 80 to 200 W and the fan speed was set at 3300, 4200 or 5000 RPM. The filling volume of the working fluid (water) was increased from 63 to 81 mL to determine the proper filling range. When testing the effects of the filling volume, the fan speed was set to a baseline of 4200 RPM. The precision of the filling procedure was 0.2 mL.

The CPL operation was tested by increasing the reservoir temperature from 52 to 80 °C. To investigate the proper filling volume for reservoir functionality, a range of filling volumes between 67 and 81 mL was tested. All tests were performed at a heat load of 200 W and a fan speed of 4200 RPM.

5.6 Results and Discussion – LHP Operation

5.6.1 Startup

The startup behavior of LHPs and CPLs has been heavily studied and characterized in the past, with the general agreement that LHPs start immediately with sufficient heat load to the evaporator, while CPLs require a priming process. The SCP was started as a LHP with the application of heat to the evaporator without prior priming. This was possible due to the small size of the reservoir that ensured that for the filling volumes tested, at least 85% of the working fluid was available to the heat pipe (excluding the reservoir) for circulation. All testing of the CPL operation was performed by heating the reservoir after startup as LHP.

Figure 5.12 shows the startup behavior of the SCP from room temperature. The vapor pressure and liquid pressure at the reservoir (raw data) are plotted against time, for a stepped heat input. Prior to startup, the liquid pressure is higher than the vapor pressure due to the gravitational pressure head. The initial delay in the rise of the vapor pressure (~20 seconds) is likely due to the transient heat up of the evaporator. The SCP can be considered to fully start when the liquid pressure begins to rise (~200 seconds), which is indicative of the formation of the two-phase region in the CC. Although the minimum heat load required for startup was not investigated, successful startup was observed for any heat load larger than 75 W.

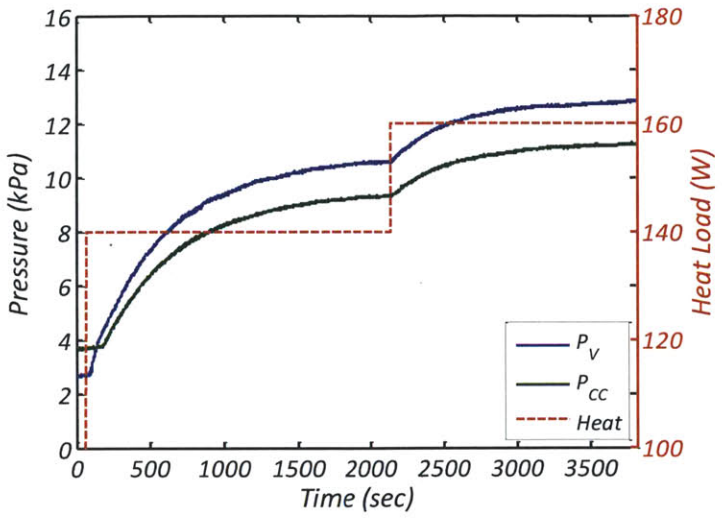

Figure 5.12. Vapor and liquid pressures plotted against time, at a fan speed of 4200 RPM. The raw data of the pressures shows the startup characteristics. The pressure measurement error is 0.3 kPa. The applied heat load is also shown schematically for reference (not logged against time).

5.6.2 Heat Removal Performance

The thermal performance of the SCP was evaluated by measuring the vapor temperature for different heat loads to the evaporator. Figure 5.13 shows the difference between the vapor and ambient temperatures, plotted against the heat load for different fan speeds. The slope of the data represents the thermal resistance. The temperature difference is taken to compensate for the change in ambient temperature among the tests; the temperature difference is representative of the thermal resistance at each heat load. The ambient air temperature varied between 19.8 and 21 °C, with a median of 20.5 °C. The measurement error for the plotted temperature difference is 0.6 °C.

Figure 5.13 shows a linear increase in the temperature difference with increasing heat load, indicating a constant thermal resistance (conductance). Since the SCP operates as a LHP in the fixed conductance mode, the thermal performance is primarily limited by the convective cooling, and the slopes of the linear fit curves in Figure 5.13 represent the convective resistances. Higher fan speeds result in lower resistance due to a higher convective heat transfer coefficient and an increase in air flow rate. The increase in air flow decreases the temperature rise of the air as it passes over the condenser surface, thereby decreasing the caloric resistance of the air. A thermal resistance of 0.177 °C/W was achieved at 5000 RPM, which is comparable to the current state-of-the-art. Multiple condensers will connect a multiple of this thermal resistance in parallel, decreasing the total heat sink thermal resistance.

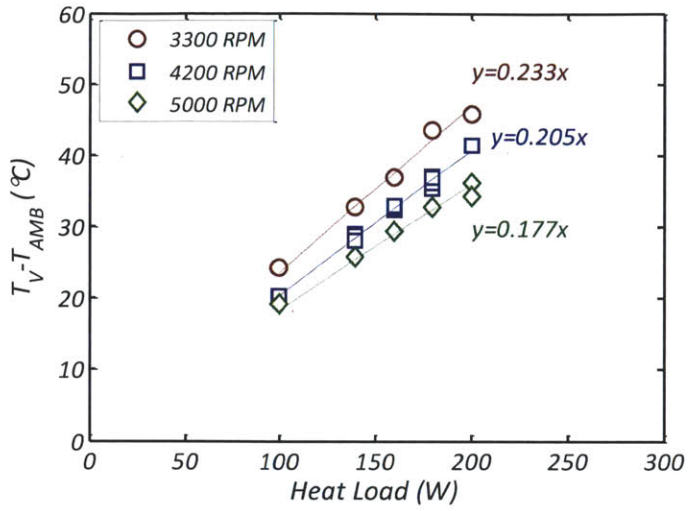

Figure 5.13. Temperature difference between the vapor and ambient air, plotted against heat load, for different fan speeds. Data for 3300 and 5000 RPM were taken at the filling volume of 67 mL, data for 4200 RPM includes the volumes of 63, 65, and 67 mL. The dotted lines are linear fit curves. The measurement error for the temperature difference is 0.6 °C.

5.6.3 Phase Separation / Capillary Pressure in the Condenser

The functionality of the condenser wick and the CC control of the liquid pressures were investigated by evaluating the capillary pressure at the condenser wick. Figure 5.14 shows the difference between the vapor and liquid pressures in the condenser, plotted against the heat load and fan speed. The measurement error of the pressure difference is 0.1 kPa. The liquid pressure is taken at the exit of the condenser; calculation of the capillary pressure differential must take into account the viscous pressure drop through the condenser wick, as follows.

$$\Delta P_{cond\ cap} = P_V - P_L - \Delta P_{wick} \qquad 5.1$$

$\Delta P_{cond\,cap}$, P_V, P_L, ΔP_{wick} indicate the capillary pressure at the condenser wick, vapor and liquid pressure, and the viscous pressure drop through the condenser wick, respectively. A positive $\Delta P_{cond\,cap}$ indicates a receding meniscus. The expected ΔP_{wick} is shown separately from the difference between the vapor and liquid pressures as it is not an experimentally measured value. ΔP_{wick} was calculated for a given mass flow rate (heat load) using an experimentally measured permeability of the condenser wick [66]. Figure 5.14 shows that a $\Delta P_{cond\,cap}$ is always positive, indicating that a receding meniscus was formed for all of the heat loads tested. This confirms phase separation in the condenser and the presence of a thermal gradient across the evaporator wick.

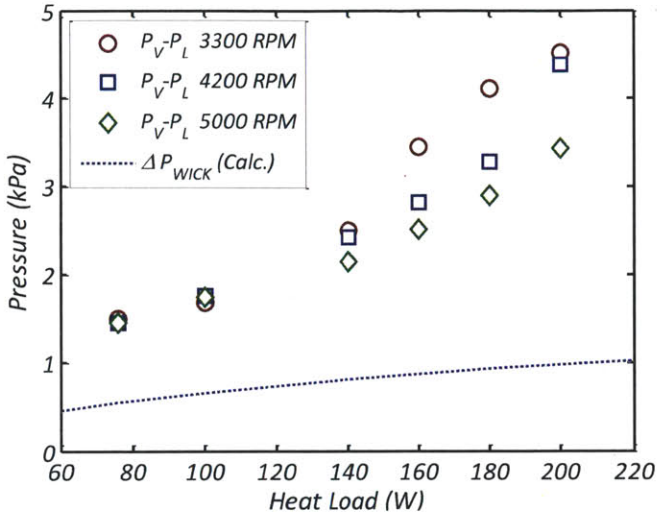

Figure 5.14. Pressure difference between the vapor and liquid in the condenser, plotted against the heat load for different fan speeds. The dotted line indicates the expected pressure drop across the condenser wick. Data for 3300 and 5000 RPM were taken at the filling volume of 67 mL, data for 4200 RPM were taken at 69 mL. Pressure measurement is 0.1 kPa.

Figure 5.14 shows similarities to Figure 3.6 in Chapter 3. The pressure difference increases with heat load with an upwards curvature. As described in Chapter 3 and 4, the higher vapor temperature from a higher head load increases the temperature difference between the vapor channels and CC. This temperature difference is translated to a greater saturation pressure difference between the CC and vapor channels. Additionally, at higher temperatures, the temperature difference results in a greater pressure difference due to the increase in $\left(\frac{dP}{dT}\right)_{sat}$. Since the vapor temperature increases more rapidly with head load for lower fan speeds, the increase in pressure difference is consequently greater.

5.6.4 Effect of Filling Volume on Thermal Resistance

The proper filling volume of LHPs depends on the size of the liquid-side volume and must account for thermal expansion at the highest expected operating temperature. To compensate for the expansion, the heat pipe must be filled below the liquid-side volume by a prescribed amount. This results in vapor in the liquid-side of the heat pipe, in the two-phase region of the CC. The CC therefore compensates for the volume change. Figure 5.15 shows the temperature difference between the vapor and ambient plotted against filling volume and heat load, for LHP operation at 4200 RPM. For a given heat load, the temperature difference represents the thermal resistance. Different heat loads are shown to indicate operation at different temperatures.

The temperature difference does not substantially change for the filling volumes between 63 and 78 mL, but increases with filling volumes greater than 78 mL. Constant thermal resistance is maintained for the range of filling volumes as the CC compensates for under-filling by expanding the size of the vapor region. 78 mL represents the filling volume in which the compensatory vapor region in the CC is minimized. However, the large range of filling volumes with constant thermal resistance (15 mL) does

not match with the size of the CC (5.6 mL). We hypothesize that the SCP was functional at the lower filling volumes by vapor occupation in one of the liquid lines, thus extending the effective volume allowed for the CC.

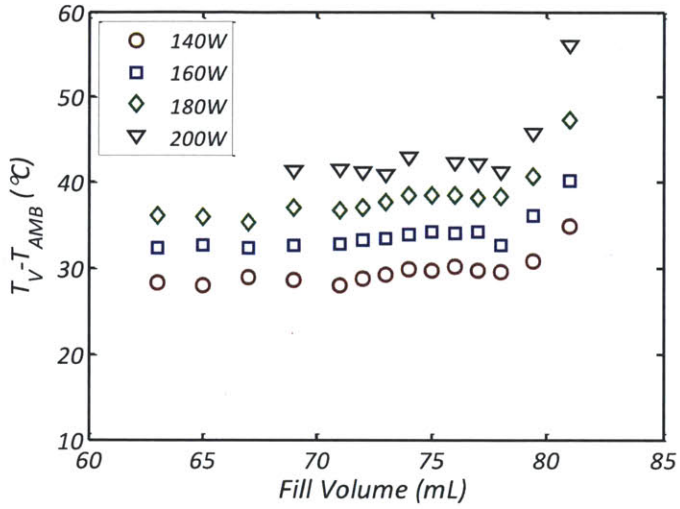

Figure 5.15. Temperature difference between the vapor and ambient air, plotted against the filling volumes for different heat loads. Data was taken for a fan speed of 4200 RPM. The measurement error for the temperature difference is 0.6 °C.

The increase of the temperature difference after 78 mL indicates over-filling, and approximately matches with the calculated liquid volume of 75 mL. Liquid occupation at the cooler ends of the vapor lines is a possible cause of the volume difference. When over-filled, the heat pipe is filled to the extent that the liquid not only occupies the allocated liquid space, but also a portion of the vapor space in the condenser (Figure 5.16). As a result, the area available to the vapor for condensation is decreased. The condenser must operate with a hotter vapor temperature to be able to condense the mass flow associated with the same heat load. For a given over-filled volume, the increase in the temperature difference is more pronounced at higher heat loads due to the greater volume expansion of the liquid from the higher operating temperatures.

Figure 5.17 shows the vapor and liquid pressures plotted against the filling volume, for different heat loads. A pressure difference between the vapor and liquid is maintained for the under-filled volumes up to 78 mL, but for filling volumes greater than 78 mL, the pressures become equal. When the heat pipe is over-filled, the vapor-liquid phase separation does not occur across the wick surface, and the condenser wick cannot be considered to have a stable meniscus at the wick surface.

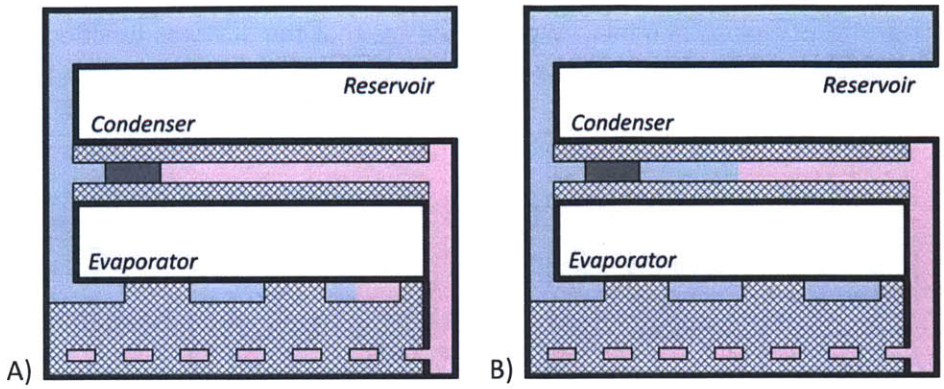

Figure 5.16. Schematic of the filling conditions at A) 63-78 mL and B) 78+ mL (over-filled). Note that the two-phase region in the CC (pink) is lost in the over-filled case. Pink and light blue regions indicate vapor and liquid, respectively. The hatched sections indicate the wicks.

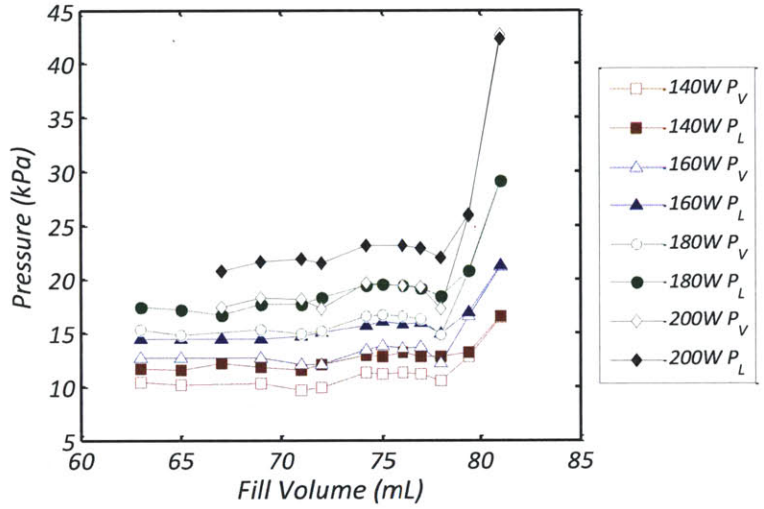

Figure 5.17. Vapor and liquid pressures, plotted against filling volume. The vapor and liquid pressures equal when the heat pipe is flooded (< 78 mL) Pressure measurement error is 0.3 kPa.

5.7 Results and Discussion – CPL Operation

5.7.1 Effect of Reservoir Temperature on Liquid Pressure

The effectiveness of the reservoir in controlling liquid pressure was evaluated by observing the change in the liquid pressure while the reservoir temperature was increased. Figure 5.18A illustrates the expected dependency of the liquid pressure on the reservoir temperature. Two regions are shown: the flat region is characterized by saturation in the CC (LHP), and the curved region is characterized by saturation in the reservoir (CPL). The transition between the two regions indicates the transfer of the two-phase region from the CC to the reservoir. The liquid pressure in the LHP region shown in Figure 5.18A is an average liquid pressure that was experimentally measured for LHP operation, and the pressure of the curved CPL region is the saturation pressure at the measured reservoir temperature.

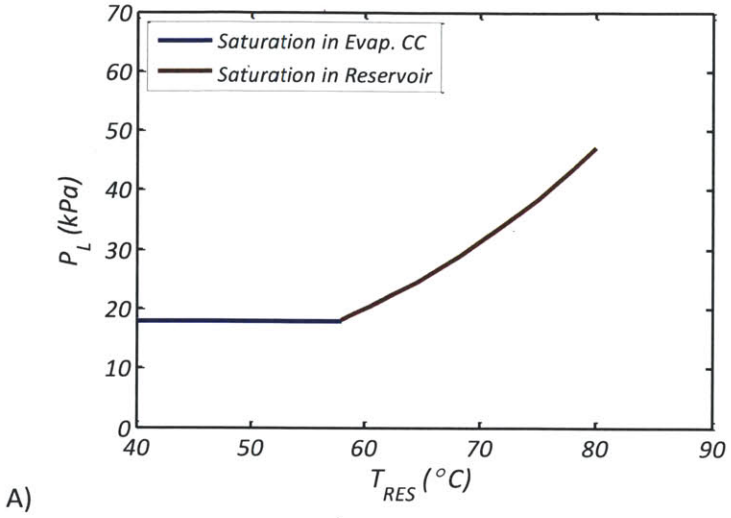

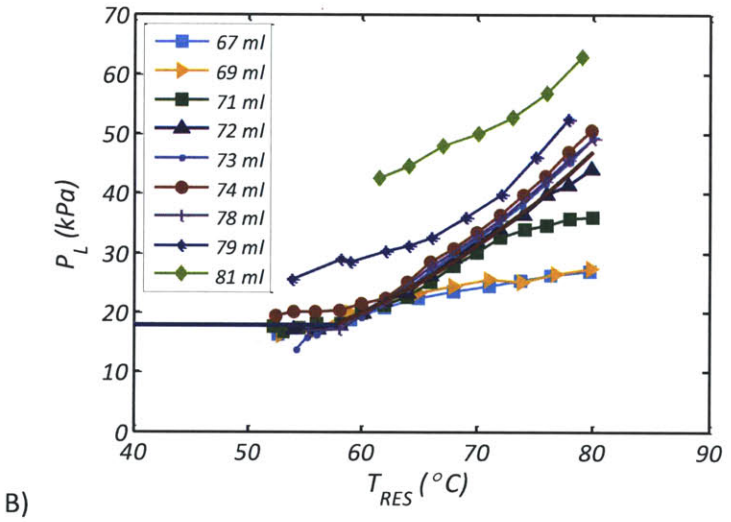

Figure 5.18. Liquid pressure dependency on the reservoir temperature and filling volume, showing A) Expected liquid pressure dependence on the reservoir temperature. B) Liquid pressure plotted against the set temperature of the reservoir, for different filling volumes. Pressure measurement error is 0.3 kPa.

Figure 5.18B shows the liquid pressure at the reservoir plotted against the reservoir set temperature and filling volumes. The predicted liquid pressure profile from Figure 5.18A is superposed for reference. With respect to the effect of the filling volume, three regimes exist: under-filled (67-72 mL), properly filled (72-78 mL), and over-filled (>78 mL). The under and properly filled cases demonstrate equal operation as a LHP, but vary in performance as a CPL. The data for the lowest reservoir temperature for each of the curves represent an unheated reservoir, and corresponds to the data shown in Figure 5.17 as LHP operation at 200 W. Although the reservoir is unheated, the reservoir temperature is higher than ambient temperature due to conductive heat transfer from the remainder of the heat pipe.

For the under-filled volumes of 67-71 mL, the liquid pressure does not follow the saturation curve through the range of reservoir temperatures tested. The insufficient filling results in a two-phase region with a vapor volume larger than the reservoir. The interface, which dictates the saturation pressure, is located in the liquid tube. As a result, the temperature measured at the instrumented location of the reservoir is not representative of the actual interface temperature and the interface temperature is not responsive to the reservoir heating. 71 mL shows the transitional case, in which the interface is initially contained in the reservoir but moves towards the tubes as the reservoir is heated.

For filling volumes between 72-78 mL, the experimentally measured pressures are in good agreement with those of the reference curve, and indicate a two-phase reservoir. The proper filling range is that which results in a two-phase vapor region sized to fit within the isothermal volume of the reservoir. However, the measured filling range, 6-7 mL, is less than the reservoir volume. This difference is due to the temperature gradient in the reservoir. To understand the temperature profile, the reservoir was modeled in COMSOL Multiphysics using experimentally measured values for the boundary conditions (reservoir, vapor line and liquid line temperatures). A schematic of the model geometry is shown in Figure 5.19. The reservoir was modeled with four 2 cm tubes (Monel 400, ID = 6.35 mm, OD = 9.53 mm) inserted to mid-height, with the vapor and liquid temperatures imposed on the ends of each tube to simulate connection to the condenser. The aerogel-insulated planar surface was modeled as adiabatic; a convective heat transfer coefficient of 20 W/m^2-K was used for all other exposed surfaces. The temperature profile is shown in Figure 5.20. The hottest areas indicate the locations of the polyimide heaters. Due to the direct contact with liquid line, a significant temperature gradient exists near the liquid line. If this area is excluded, the reservoir temperature is spatially uniform to within two degrees. Thus, the interpretation of "properly filled" refers to the containment of the vapor region in the near-isothermal area of the reservoir, excluding the area near the liquid lines. Furthermore, due to the two degree temperature gradient in the reservoir, the true vapor-liquid interface temperature may be slightly different from the measured value, resulting in liquid pressures that deviate slightly from saturation pressure calculated for the measured reservoir temperature (Figure 5.18B). As the filling volume is increased and the size of the vapor region in the reservoir decreases, the interface temperature approaches the hottest reservoir temperature, and the measured liquid pressure exceeds the saturation pressure of the temperature at the instrumented location. Similarly, installation of the thermistor near the cooler liquid lines will compromise the accuracy of the measurement.

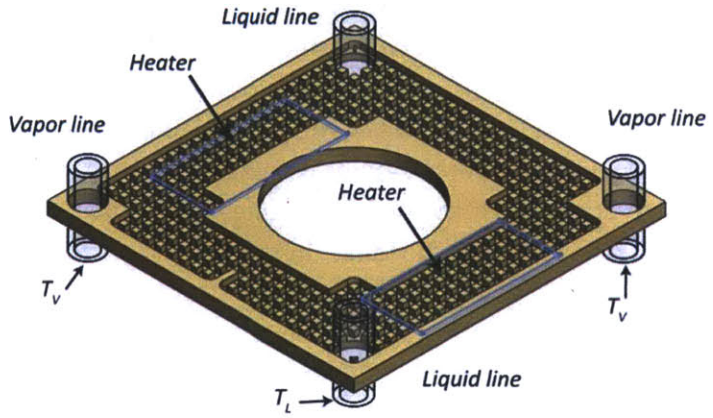

Figure 5.19. Schematic of modeled reservoir. The heaters are applied to the bottom of the reservoir; the locations are outlined in grey.

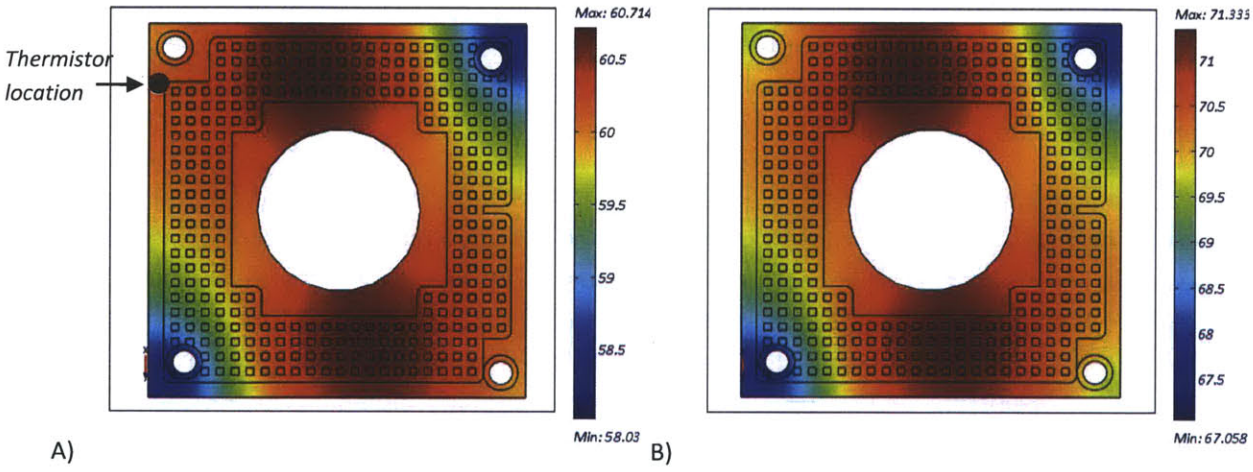

Figure 5.20. Temperature profile (°C) of the reservoir, modeled with experimentally measured reservoir, vapor line and liquid line temperatures as boundary conditions. Two reservoir temperatures are shown, A) 60 °C and B) 70 °C. The boundary conditions (temperature) used are A) T_V=61.4 °C, T_L=45.56 °C; B) T_V=66.9 °C, T_L=45.4 °C,

When the filling volume is increased to 79 mL, the liquid pressure dependence on the reservoir temperature departs from the reference curve due to the higher thermal resistance with the over-filling of the heat pipe. Over-filling results in excess liquid in the heat pipe which enters the vapor space of the condenser. The condensation interface no longer occurs on the wick surface, and the vapor and liquid pressures are equal. Figure 5.18B shows that the liquid pressure (and vapor pressure) increase with an increase in the reservoir temperature. This increase occurs through the effect of the reservoir temperature on the vapor pressure, and is discussed in detail in the following section.

5.7.2 Effect of Reservoir Temperature on Vapor Pressure

In addition to controlling the liquid pressure, the reservoir can be used to change the vapor pressure. The vapor pressure is affected through two mechanisms, through 1) direct reservoir control of the vapor pressure, and 2) a higher effective heat load due to the heating of the reservoir.

Direct control of the vapor pressure occurs through flooding. For properly filled CPL operation with the reservoir within the temperature range prescribed in Equation 2.29, the liquid pressure is independent from that of the vapor through the condenser and evaporator menisci, and the reservoir controls only the liquid pressure. However, for conditions in which the pressure difference is no longer supported by the condenser meniscus, the liquid and vapor pressures will equal, and the reservoir control of the liquid pressure directly translates to a control of the vapor pressure. This condition of the vapor and liquid pressures being equal will be referred to as "flooding" in the following discussion, in reference to the condition of the condenser wick. In this case, the effect of the reservoir on the heat pipe is similar to that of a CPL with a non-wicked condenser in variable conduction, in which the reservoir is used to set the operating (vapor) pressure and temperature. Flooding can occur when the heat pipe is over-filled, or when the reservoir temperature exceeds the limits of Equation 2.29.

The second mechanism of vapor pressure control is through the increase in the effective heat load on the heat pipe. Because the reservoir is in direct thermal contact with the vapor and liquid lines, heat is conducted from the reservoir to the remainder of the heat pipe. The conduction from the reservoir to the liquid line is can be seen in the thermal gradient near the liquid line in Figure 5.20. Heating the reservoir for temperature control effectively adds to the heat load of the heat pipe, causing the vapor temperature to increase.

Figure 5.21 schematically illustrates the expected pressure dependency on the reservoir temperature for the properly filled case, and shows the effect of the first mechanism. The grey horizontal line indicates the expected vapor pressure in LHP operation, this pressure is the average vapor pressure measured in Section 5.6.4. The expected liquid pressure curve from Figure 5.18A is included for reference. The vapor pressure is unaffected by changes to the liquid pressure as long as a pressure discontinuity is maintained by the condenser meniscus. The pressure discontinuity disappears when the reservoir temperature exceeds the range prescribed in Equation 2.29 and the liquid pressure equals the vapor pressure. Thus, the intersection of the vapor pressure curve (grey line) and the saturation curve at ~61 °C (red line) represents the lower limit of Equation 2.29, and indicates the onset of flooding. This type of flooding will be referred to as "Type 1 flooding," and is induced by high reservoir temperatures. Flooding due to over-filling will be referred to as "Type 2 flooding," and is independent of operating conditions.

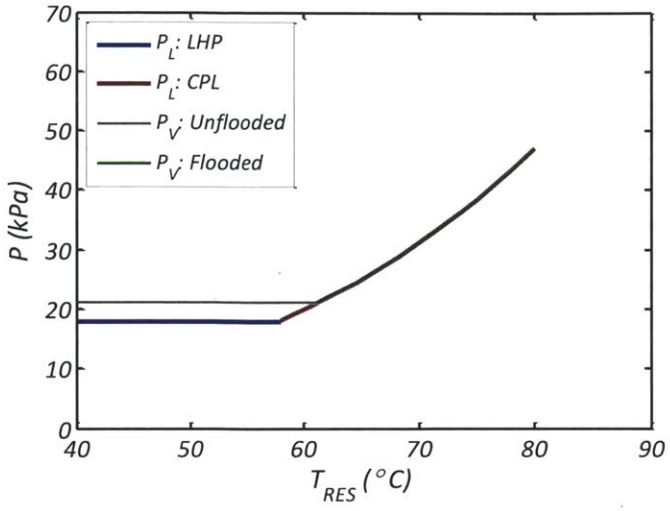

Figure 5.21. Expected vapor pressure dependence on the set temperature of the reservoir. The vapor pressure shown for the unflooded case is average vapor pressure measured for LHP operation. The expected liquid pressure from Figure 5.18A is included for reference.

Figure 5.22 shows the vapor and liquid pressures as a function of the reservoir temperature, for four different filling volumes, and represents the range from under to over-filled. The vapor and liquid pressure curves from Figure 5.21 are also included for reference. The liquid pressures are the same data as that shown in Figure 5.18B, and show differing levels of departure from the saturation curve depending on the degree of under-filling. The difference between the vapor and liquid pressure is the receding capillary pressure differential at the condenser wick.

In both the under and properly filled cases (69, 71, 72 mL), the vapor pressure increases with reservoir temperature. The vapor pressure curve can be considered to consist of two regimes, before it intersects the saturation curve and after the intersection. The intersection is indicated in Figure 5.22A-C by the vertical dotted lines. Until the vapor pressure meets the saturation curve, the increase is nearly the same for the different filling volumes, and is independent of the liquid pressure. This increase is caused by the higher effective heat load due to the conduction from the reservoir, and is not represented in the idealized operation illustrated in Figure 5.21.

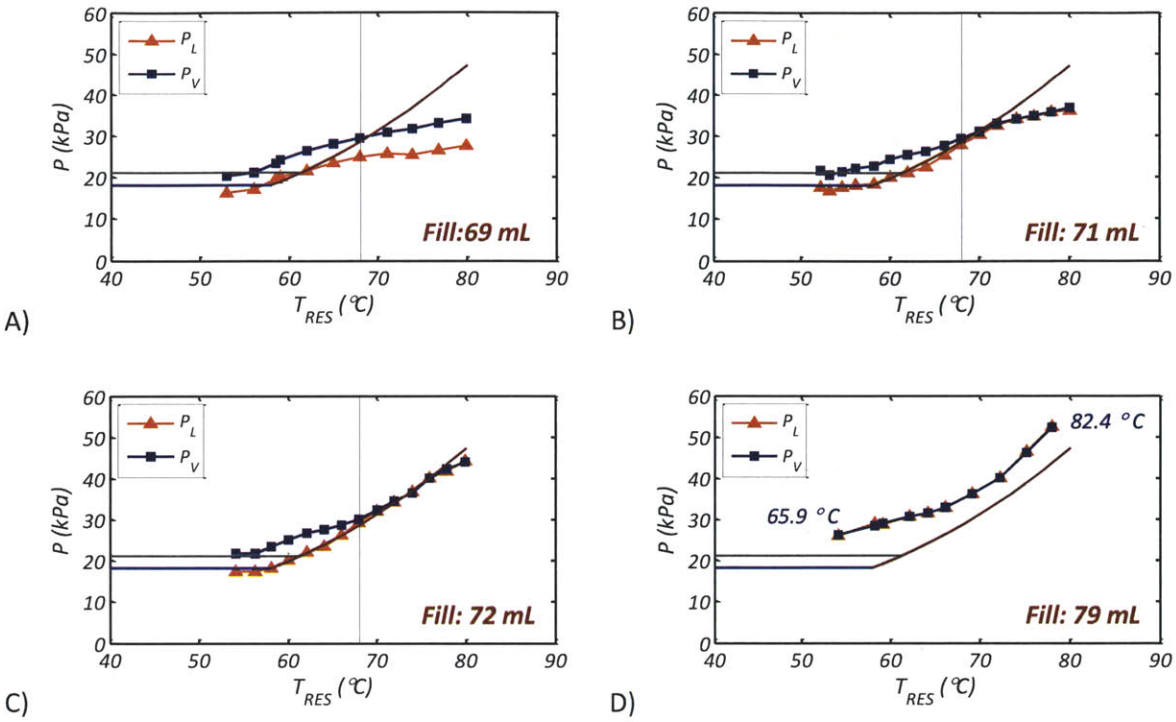

Figure 5.22. Vapor and liquid pressures plotted against the set temperature of the reservoir, for filling volumes of A) 69 mL, B) 71 mL, C) 72 mL, and D) 79 mL. The vapor temperatures at the lowest and highest reservoir temperatures are indicated in D). Pressure measurement error is 0.3 kPa.

After intersecting the saturation curve, the increase in vapor pressure with reservoir temperature is distinctly different, and depends on the filling volume. At 69 mL, the liquid pressure remains lower than the vapor pressure for all reservoir temperatures tested, and a receding meniscus is maintained. The increase in vapor pressure is due to the higher effective heat load in both regimes, before and after the saturation curve. At 71 mL, the higher filling allows the liquid pressure to better follow the saturation curve and approach the vapor pressure. The liquid pressure increase due to the heated reservoir is greater than the increase in vapor pressure from the higher heat load, and the vapor and liquid pressures become equal after the saturation curve. Type 1 flooding occurs, induced by the increase in reservoir temperature. Type 1 flooding is also observed at 72 mL; the vapor pressure is "pulled upwards" by the increase in liquid pressure along the saturation curve. In order for the vapor temperature to match the vapor pressure increase, the thermal resistance of the heat pipe is increased by flooding the condenser vapor space with excess liquid. Type 1 flooding equates to CPL operation in the variable conductance mode, and is not possible if more liquid is required to flood the condenser than is available in the reservoir. This is seen at 71 mL. While liquid is initially present in the reservoir, condenser flooding that occurs with Type 1 flooding results in the depletion of the reservoir liquid, and the liquid and vapor pressures depart from the saturation curve. This type of flooding can therefore only happen in mildly under-filled (> 71 mL) and properly filled cases.

When the heat pipe is over-filled, liquid is present in the vapor space of the condenser and the thermal resistance increases. As shown in Figure 5.22D, Type 2 flooding occurs, and the vapor and liquid pressures are equal regardless of reservoir temperature. The higher thermal resistance results in higher vapor temperature and pressure and therefore higher liquid pressure. Furthermore, when over-filled, a two-phase region no longer exists on the liquid side, as it is completely filled with liquid. The lack of a meniscus in the condenser results in the vapor pressure setting (equaling) the liquid pressure, causing the liquid pressure to be higher than it would otherwise be when properly or under-filled. For a given reservoir temperature and heat load, the fluid in the reservoir becomes thermodynamically sub-cooled. The reservoir therefore does not function in the over-filled state. The exception to this is the condition in which the reservoir is heated in excess of the vapor temperature; however, this condition was not tested.

Since the vapor temperature and pressure are related through the saturation curve, Figure 5.22D represents a vapor temperature increase with reservoir temperature. This is caused by a higher effective heat load and the resulting thermal expansion of the working fluid. Heating the reservoir increases the heat load, which causes an increase in the overall heat pipe temperatures. The lower liquid density at higher temperature results in volume expansion, and since the magnitude of the expansion is comparable to the vapor (condensation) space of the condenser (2.6 mL), the thermal resistance is noticeably increased by additional flooding. This adds to the effect of the higher heat load in increasing the vapor temperature. A quantitative calculation of this effect is not straightforward due to the non-uniform temperature in the system, but an approximation is as follows. The vapor temperature is the highest temperature in the heat pipe, and only a small amount of liquid reaches this temperature. Most of the liquid will be closer to the reservoir temperature. If this temperature is used to calculate the volume change between the two extreme operating points of Figure 5.22D (T_{RES} = 53 °C and 78 °C), taking into account that initial filling occurred at 20 °C, the expansion is 1.1 mL. This amounts to a 42% reduction of the condensation space, and is close to the 37% increase in the vapor-ambient temperature difference that is observed across this range. It is important to note that consideration of volume expansion is not necessary for analyzing the under and properly filled cases because the volume increase is compensated by the reduction of the vapor space in the reservoir.

Figure 5.23 compiles the vapor pressure measurements taken at the under and properly filled volumes, plotted against the reservoir temperature. The predicted vapor and liquid pressure curves from Figure 5.21 are superposed for reference. In the regime before the vapor pressure intersects with the saturation curve (T_{RES} < 68 °C), the data collapse into one curve, as the shared mode of pressure increase is the higher effective heat load from heating the reservoir. After the intersection with the saturation curve (T_{RES} > 68 °C), the behavior can be separated into two types, depending on whether flooding occurs:

1) When the heat pipe is properly filled, the liquid pressure increases according to the saturation curve, and also causes the vapor pressure to increase due to Type 1 flooding. This is indicated by the change in the slope before and after the intersection with the saturation curve. Type 1 flooding may also occur when under-filled, but to a varying degree. Higher filling (less under-filling) allows the liquid pressure to better follow the saturation curve and results in Type 1

flooding. When properly filled, this behavior is equivalent to a conventional CPL in variable conductance mode.

2) In the case of severe under-filling, the liquid pressure does not meet the vapor pressure as the reservoir temperature is increased, and a receding meniscus will be maintained in the condenser. In this case (67 and 69 mL), the liquid pressure does not affect the vapor pressure, and vapor pressure increase continues due to the higher effective heat load. This is shown in Figure 5.23 as the continuation of the slope from the first regime.

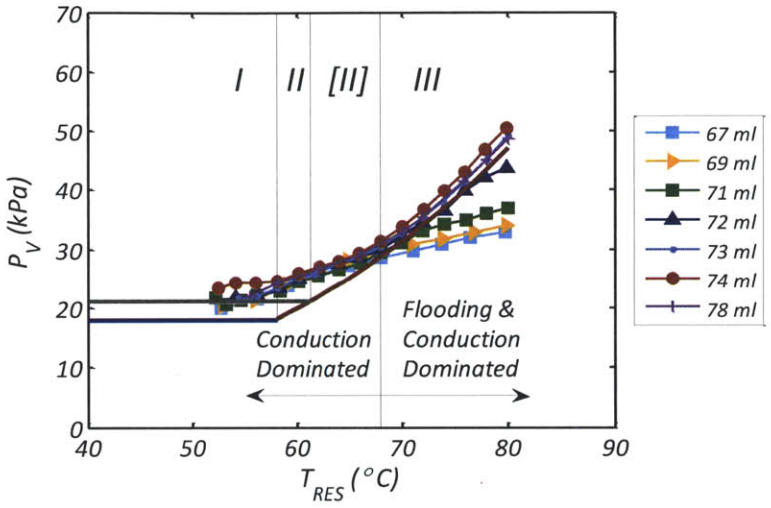

Figure 5.23. Vapor pressures plotted against the set temperature of the reservoir, for under-filled and properly filled volumes. I, II, and III refer to the three operating modes of the SCP. Measurement error is 0.3 kPa.

5.7.3 Summary of the Effect of Filling Volume: Three Ranges

In contrast to the LHP operation, the CPL operation is characterized by defined "under-filled" and "properly filled" volumes, as improper filling compromises the functionality of the reservoir. Figure 5.24 summarizes the three ranges of filling. Specifically, the properly filled range is bounded by the volumes that allow the largest (72 mL) and smallest (78 mL) vapor volumes in the two-phase region in the reservoir. The LHP, on the other hand, was found to operate with equal performance (thermal resistance) as long as over-filling was avoided. The terminology of "under-filled" and "properly filled" are therefore not directly applicable to the LHP. Filling beyond 78 mL resulted in over-filling in both LHP and CPL operation, with a characteristic increase in thermal resistance and loss of phase separation in the condenser.

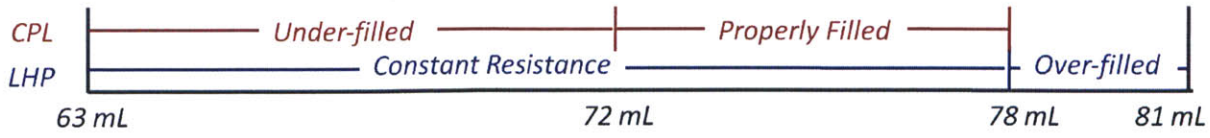

Figure 5.24. Ranges of filling: under-filled, properly filled, and over-filled.

5.8 Operating Modes

When properly-filled, the operation of the SCP can be separated into three modes as a function of the reservoir temperature, annotated as I, II and III in Figure 5.23.

I When the reservoir temperature is lower than the evaporator CC temperature, the SCP operates as a LHP.

II+[II] When the reservoir temperature exceeds that of the CC, the reservoir is two-phase, and CPL operation is observed (II and III). For the range of reservoir temperatures defined by Equation 2.29, the SCP operates as a CPL in the fixed conduction regime, with the reservoir controlling the liquid pressure (II). In this range, condenser flooding is avoided while the condenser capillary pressure is decreased. Due to the conduction from the reservoir to the remainder of the heat pipe, heating the reservoir increases the vapor temperature, which allows for higher reservoir temperatures by extending the range of Equation 2.29. As a result, the actual range for operation in fixed conduction mode is extended (II+[II]). The temperature limit of Equation 2.29 can be graphically seen in Figure 5.23 as the intersection of the vapor pressure and the reservoir saturation curve.

III When the reservoir is heated beyond the limits of Equation 2.29, the SCP undergoes Type 1 flooding and operates with variable conductance. In this mode, the reservoir sets both the liquid and vapor pressures through controlled condenser flooding, and operates in the same manner as a conventional CPL with a non-wicked condenser in variable conductance mode.

In summary, mode I allows for a hands-free operation as a LHP with the maximum capillary pressure in the condenser and the lowest thermal resistance. Mode II allows for operation as a CPL that eases the capillary pressure required in the condenser while still maintaining an unflooded state. Mode III, alternatively, enables operator control of the heat pipe temperature in case the heat source requires a specific operating temperature.

5.9 Summary

An air-cooled, single condenser heat pipe prototype was constructed with the capability of dual-mode, LHP / CPL operation. The prototype was developed as a simplified platform for characterizing the novel heat pipe cycle, without the complexity of multiple condensers. The integrated heat sink was tested to evaluate the thermal resistance (LHP), confirm operation with a receding capillary meniscus in the condenser (LHP), and confirm operation with active pressure control (CPL). The effect of the filling volume on the thermal resistance and pressure control was also investigated.

The thermal resistance of 0.177 °C at 5000 RPM was achieved and up to 3.5 kPa of capillary pressure was generated in the condenser, confirming the successful operation of the heat pipe cycle. Higher fan speeds resulted in lower thermal resistance and lower capillary pressure in the condenser. The filling volume was found to affect the LHP and CPL modes of operation differently. No adverse effects were observed for the LHP operation for the under-filled volumes tested. In contrast, liquid pressure control in CPL operation was found to be compromised by under-filling (63-72 mL), due to insufficient liquid in

the reservoir. Over-filling (>78 mL), on the other hand, resulted in the complete loss of liquid pressure control due to flooding of the condenser and collapsing of the two-phase region in the reservoir. For both LHP and CPL operation, over-filling resulted in a noticeable increase in the thermal resistance.

Three operational modes were observed when the heat pipe was properly filled, depending on the reservoir temperature and the corresponding state of the liquid-vapor interface in the condenser. First, at low reservoir temperatures, the two-phase region is located in the evaporator CC, and the heat pipe operates as a LHP with a liquid pressure lower than that of the vapor. A receding capillary meniscus is formed on the surface of the condenser wick, separating the vapor and liquid phases and sustaining a pressure discontinuity. The second mode is observed when reservoir temperature is increased beyond the CC temperature. Like the first mode, the vapor-liquid phase separation occurs across the condenser wick meniscus, but the two-phase region transfers to the reservoir, resulting in operation as a CPL in the fixed conduction mode. This operational mode allows for lower capillary pressures required at the condensers while still preventing flooding. When the reservoir is heated such that the reservoir saturation pressure meets the vapor pressure, the third operational mode is observed. Vapor-liquid phase separation is no longer present and the heat pipe operates as a CPL in variable conductance mode. The vapor and liquid pressures in the condenser are equal and are set by the reservoir temperature. A seamless transition between the three modes was demonstrated by gradually increasing the reservoir temperature. Thus, two mechanisms of controlling the heat pipe temperature were characterized: control of the fan speed and reservoir temperature.

In summary, the evaporator, condenser and reservoir were integrated into a prototype air-cooled heat pipe, and a capillary pressure was measured in the condenser, confirming the functionality of the novel heat pipe cycle. Furthermore, three operational modes were characterized as a function of the reservoir temperature. The understanding of the heat pipe cycle gained from this study is applied in Chapter 6, in characterizing the multiple condenser heat pipe.

6 The Multiple-Condenser Prototype Heat Pipe

6.1 Overview

A six-condenser heat pipe was constructed to confirm the functionality of the multiple-condenser heat pipe cycle. This device will be referred to as the "Multiple-Condenser Prototype" (MCP). Like the SCP, the MCP was tested in both LHP and CPL operation. This chapter reports the characterization of the MCP, which begins with a description of the experimental setup and follows with an evaluation of the overall thermal performance of the multiple-condenser configuration. The effect of condenser flooding on thermal resistance is then described for various orientations. Finally, the degree of liquid and vapor pressure control is analyzed with respect to the filling volume of the working fluid. As many of the analyses parallel those performed on the SCP, the layout of the figures are similar and overlapping descriptions are abridged.

6.2 Thermal-Fluidic Cycle

The thermal fluidic cycle of the MCP is described in Sections 2.2 and 2.3 (LHP and CPL, respectively) in Chapter 2. The thermal performance of the MCP is characterized using the LHP cycle, as the heating of the reservoir in the CPL cycle adds an additional, unmeasured heat load to the device. The CPL cycle is tested in the multiple-condenser configuration for liquid and vapor pressure control, for the reasons mentioned in Chapter 5 (Section 5.2).

6.3 Experimental Apparatus

The MCP was constructed with the integration of a six-impeller fan assembly into a six-condenser heat pipe. The MCP is shown in Figure 6.1. The heat pipe consists of an evaporator, six condensers, a reservoir and four tubes as fluidic lines. The reservoir was modified from the design used in the SCP to decrease the heat transfer from the reservoir to the liquid lines; the connection between the liquid line and the reservoir was reduced to a copper capillary tube with an inner/outer diameter of 1.65 /3.18 mm (Figure 6.2). The modified design has a total volume of 6.7 mL.

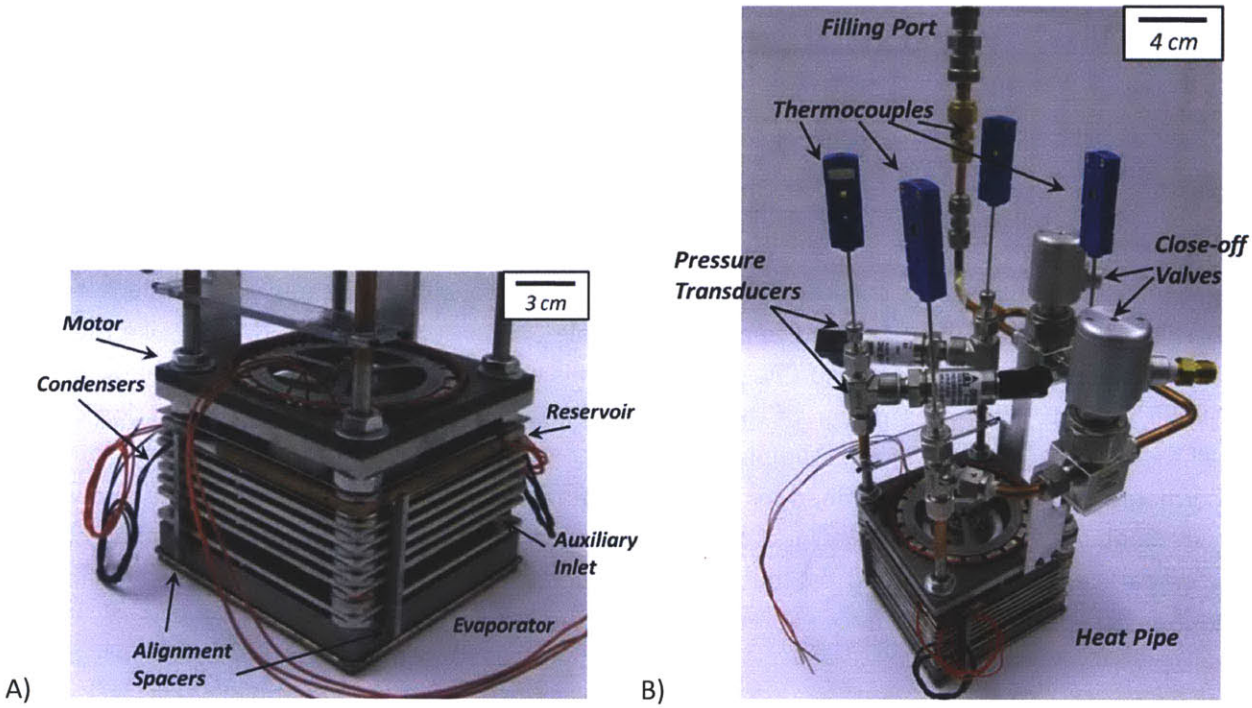

Figure 6.1. Experimental apparatus. A) Multiple condenser heat pipe. B) Multiple condenser heat pipe with the filling manifold and instrumentation.

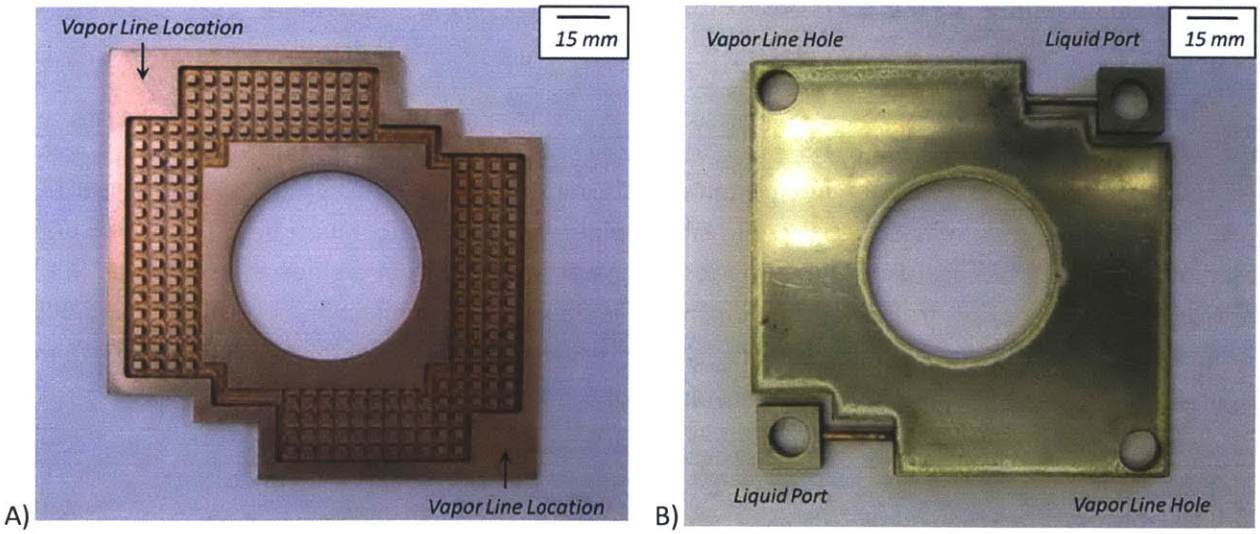

Figure 6.2. Reservoir for the MCP. A) shows the internal cavity, and B) the complete reservoir. A) shows the copper cavity before the holes for the vapor lines were drilled. The liquid ports are connected by capillary tubes (OD=3.18mm, ID=1.65 mm) to prevent conductive loss to the cooler liquid lines.

In contrast to the brazed and soldered joints of the SCP, most of the joints in the MCP were sealed with o-rings (nitrile). O-rings were used for this construction because of the difficulty of achieving a leak-tight seal with brazing in the SCP, and to allow the disassembly of the heat pipe for potential design modifications. The construction process is as follows. The liquid and vapor tubes were first soldered to the evaporator (63 % Sn / 37 % Pb). The tubes were machined for an inner/outer diameter of 9.53/6.35 mm and with slots for fluidic access to the condensers. The condensers were then inserted onto the four tubes with o-rings above and below each liquid and vapor port (Figure 6.3). The top of the tubes were threaded; nuts were used to axially compress the condenser / o-ring stack. Each o-ring was circumferentially housed in a metal ring to prevent unrestricted radial expansion. The rings can be seen between the condensers in Figure 6.1A and as the "retainer ring" in Figure 6.3. To fix the locations of the individual condensers, a comb-like structure was inserted against each side. Each condenser is positioned between the teeth of the comb structure, which shown in Figure 6.1A as the "alignment spacer." The reservoir was installed in the same manner above the top-most condenser. The assembled heat pipe seal was measured with a helium leak detector to be 10^{-8} standard cm^3/ sec. This measurement was taken before the effect of helium permeation into the o-rings was observed. Following the terminology of Chapter 2, the following descriptions will use "bottom" and "top" to refer to particular condensers, which are positioned closest to and farthest from the evaporator, respectively. In contrast, "lower" and "upper" will depend on the orientation; "lower" will refer to the condenser at the least gravitational height. Since each condenser has vapor and liquid volumes of 2.6 and 3.6 mL, the cumulative vapor and liquid volumes in the condenser stack are 15.6 and 21.6 mL, respectively. The total volume of the heat pipe was calculated to be 125.5 mL, with a liquid space of 92.7 mL.

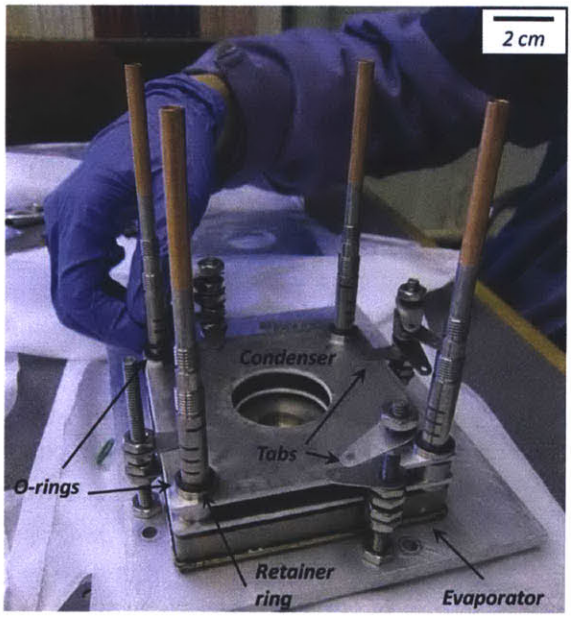

Figure 6.3. Photograph of the assembly of the MCP, showing the installation of a condenser using o-rings. The tabs compress the individual condensers and o-rings until the entire condenser stack is installed. The four slotted and threaded fluid lines are also shown.

The fan assembly was installed using the same procedure as for the SCP. Six impellers of 1.53 mm in thickness were mounted at a 0.5 mm clearance from the heat transfer surfaces. The complete stack was tightened with the four nuts for a mechanically rigid structure. To reduce the induction pressure loss of the air-flow, an auxiliary air inlet was made by removing a condenser and two impellers from the interdigitated condenser-impeller stack [30]. As shown in Figure 6.1, this inlet is located above the bottom condenser. The MCP therefore has two induction inlets, one at the top of the stack and another near the evaporator.

The four vapor and liquid tubes extend above the MCP and allow access for heat pipe charging and sensor mounting. A two-pronged manifold was made from copper tubing and compression fittings to connect two of the tube extensions, one vapor and one liquid, to the filling station (Figure 6.1B). Two of the extensions were used for mounting pressure transducers (Omegadyne, *PX309-030A5V*) for vapor and liquid pressure measurement, calibrated to an accuracy of 150 Pa. The pressure transducers were mounted 104, 114, 144, and 150 mm above the reservoir, top condenser, bottom condenser, and CC, respectively. The gravitational pressure head associated with the respective height difference was included in calculating the liquid pressure. Temperature measurements were taken by 1.59 mm diameter, 254 mm long T-type thermocouples inserted into the four tubes (Omega Engineering, *TMQSS-062U-10*), as shown in Figure 6.1B. The tips of the thermocouples were positioned at the vapor and liquid ports of the evaporator. The sensors that required internal access to the heat pipe were thus mounted on the tube extensions, away from the heat pipe, to avoid disrupting the geometry of the heat pipe. A schematic of instrumentation is shown in Figure 6.4.

In addition to the internal measurements, several temperature measurements were taken externally of the heat pipe. The temperatures of the reservoir and evaporator base were measured using 1 mm diameter, 5 mm long thermistor probes (Redfish, *Nano Tube*) with +/- 0.1 °C interchangeability. The thermistors were inserted in holes drilled into the sides of the copper reservoir body and the copper base plate of the evaporator. The surface temperatures of the condensers were also measured with type-T thermocouples (Omega Engineering, *5TC-TT-T-40-36*). The thermocouples were attached to the surface of the condenser at identical locations with polyimide tape and high thermal conductivity paste (AiT, *Cool Silver*). The locations of measurements are shown in Figure 6.5, and are labeled from 1 to 6, with 1 at the condenser closest to the evaporator. It is important to note that due to the inherent variation in the thermal contact between the surface and the thermocouple, the measured temperatures cannot be compared with one another. The temperatures are instead used as a qualitative indicator of the performance change of an individual condenser. The same type of thermocouple was used to measure the ambient air temperature. The reservoir was heated with four 50.8 mm x 25.4 mm polyimide heaters (McMaster-Carr, *35475K423*). Heat was applied to the evaporator with the heater block described in Chapter 5. Similarly, the data acquisition and heater control for the reservoir were performed with the setup described in Chapter 5.

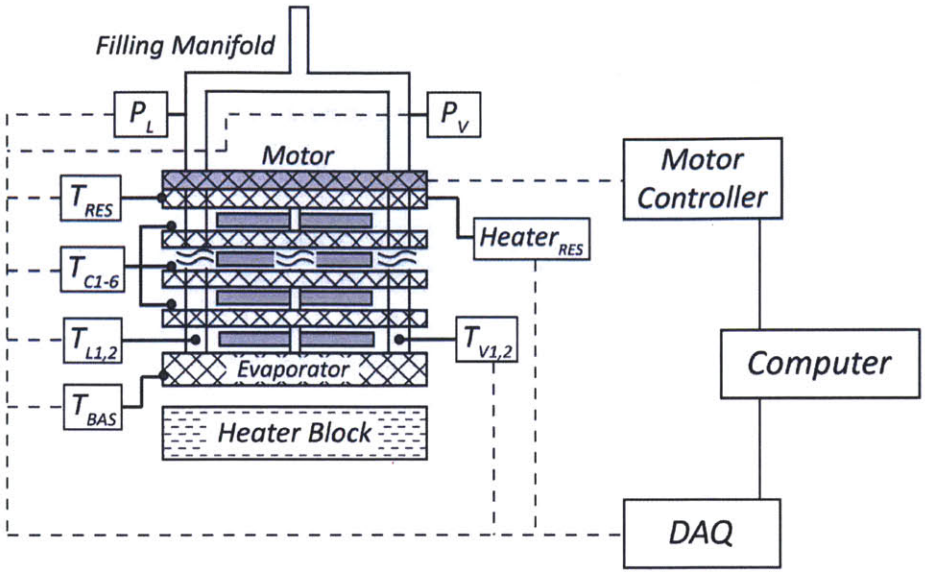

Figure 6.4. Schematic of experimental instrumentation and data acquisition layout. The routing for power supply is not shown.

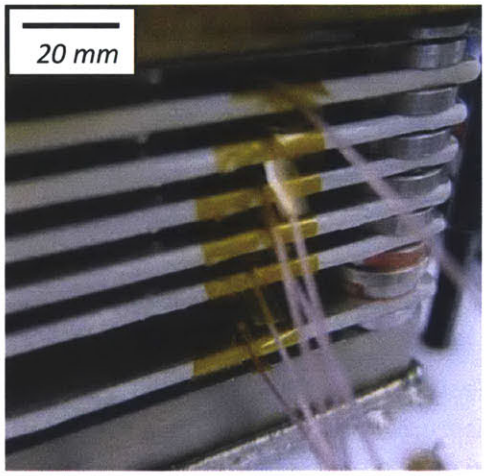

Figure 6.5. Location of the thermocouples for condenser surface temperature measurement. The photograph shows the evaporator at the bottom and the vapor line towards the right. The thermocouple is adhesively attached approximately 5 mm from the edge.

To test the effect of orientation, a hinged tilting stand was fabricated from extruded aluminum framing. The MCP was mounted onto the PTFE insulation of the heater block and the insulation was fixed to the tilting stand. The stand allows for orientations from 0° (upright) to 180° (inverted). Figure 6.6 shows photographs of the MCP on the stand, at 90° and 135°.

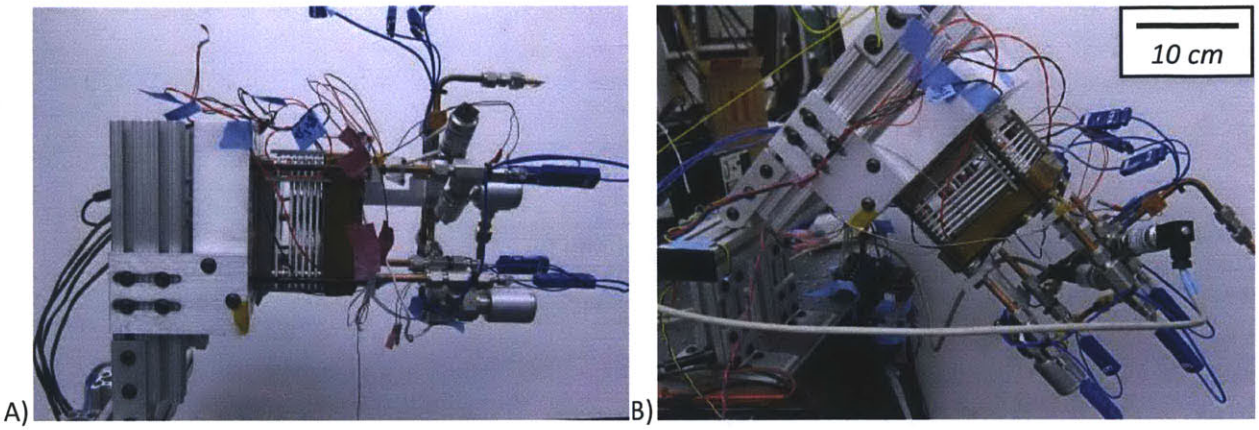

Figure 6.6. The MCP mounted to the tilting stand, at A) 90° and B) 135°

6.3.1 Test Parameters

Characterization of the MCP involved both LHP and CPL operation, focusing on the points below.

LHP Operation:

1. Thermal resistance of the heat sink
2. Phase separation in the condenser and multiple condenser functionality/performance
    a. Effect of orientation on the performance of the condenser
3. Effect of the filling volume on the thermal performance

CPL Operation

4. Effect of the reservoir temperature on the liquid and vapor pressure

The thermal resistance of the heat sink and the performance of the condensers were tested in the upright orientation, for heat loads from 40 to 500 W and fan speeds of 3500, 5000 and 6000 RPM. The effect of orientation was tested at a 5000 RPM baseline at 150, 250 and 350 W, for tilt angles from 0° to 135°. The filling volume was increased from 83 to 97 mL at 5000 RPM and 0° to determine the proper filling range. The reservoir was not used for these tests; the heat pipe was operated as a LHP.

The effect of the reservoir temperature on the liquid and vapor pressures were tested by heating the reservoir from 40 to 66 °C in the upright orientation, at 5000 RPM and 300 W. To investigate the proper filling volume for reservoir functionality, a range of filling volumes between 87 and 97 mL was tested.

6.4 Results and Discussion

6.4.1 Startup

Like the SCP, the MCP was started as a LHP without initial priming. Due to the small size of the reservoir, at least 92% of the working fluid was available to the heat pipe (excluding the reservoir) for circulation.

This volume was sufficient to initiate startup with the application of heat to the evaporator. The pressure response during startup is shown in Figure 6.7 for 150 W. The initial delay in the rise of the vapor pressure of approximately 20 seconds is likely due to the transient heat up of the evaporator. The relatively fast response of the liquid pressure indicates that the CC was initially at saturation, and the temperature increase of the CC prompted an increase in pressure. Successful startup was observed for heat loads greater than 40 W. Startup was also confirmed for tilt angles up to 120 °C at 50 W. Lower heat loads were not tested due to significantly longer times in reaching steady state. Figure 6.7 also shows that at 150 W, the MCP achieved steady state operation in approximately 1800 seconds (30 minutes).

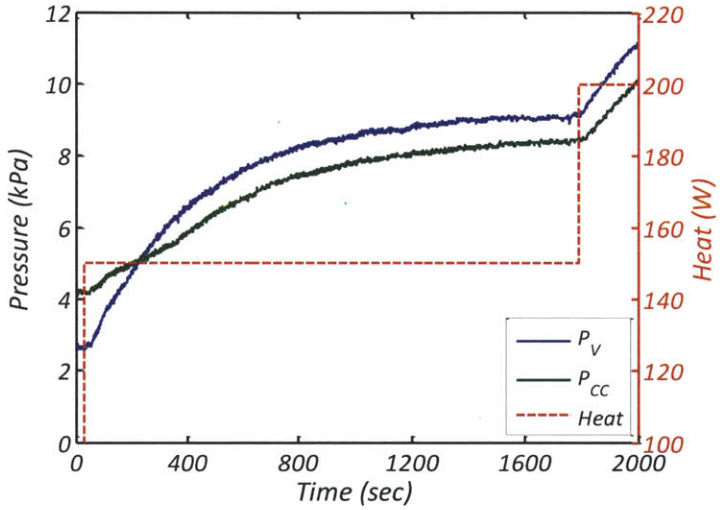

Figure 6.7. Vapor and liquid pressures plotted against time, at a fan speed of 5000 RPM, at 91 mL. The raw data of the pressures shows the startup characteristics. The pressure measurement error is 0.15 kPa. The applied heat load is also shown schematically for reference (not logged against time).

6.4.2 Thermal Resistance

Analysis of the thermal resistance was separated into two parts, from the base to the vapor and from the vapor to the ambient. Hence the resistances of the evaporator and the combined resistance of the condenser and convection were investigated separately. The conductive resistance across the condenser body was assumed to be negligible compared to the convective resistance due to the thin metallic body.

Figure 6.8 shows the temperature difference between the base and vapor, plotted against the heat load. The results are slightly higher than the temperature difference measured at 100 °C in Chapter 4 due to the higher vapor viscosities and thus higher channel pressure loss at lower temperatures. The average thermal resistance of the evaporator is approximately 0.004 °C/W. Since the temperature drop between the vapor and the condenser surface is expected to be between 0.6 and 2.5 °C, the thermal resistance of the heat pipe is between 0.0046 to 0.0065 °C/W.

Figure 6.9 shows the difference between the vapor and ambient temperatures, plotted against the heat load for different fan speeds. The ambient temperature varied between 22.3 and 24.5 °C, with a median of 23.4 °C. The dotted lines indicate linear fit curves with a zero y-intercept, and the slopes indicate the average thermal resistances. Higher fan speeds decrease the thermal resistance due to the greater air-flow rate and the higher convective heat transfer coefficient. A thermal resistance of 0.098 °C/W is achieved at 6000 RPM, for a heat removal of 500 W at a vapor-ambient temperature difference of 50 °C. Since this resistance is significantly larger than the evaporator and heat pipe thermal resistances, the heat transfer in the MCP is limited by the air-cooling, and the total heat sink thermal resistance is approximately 0.1 °C/W at 6000 RPM.

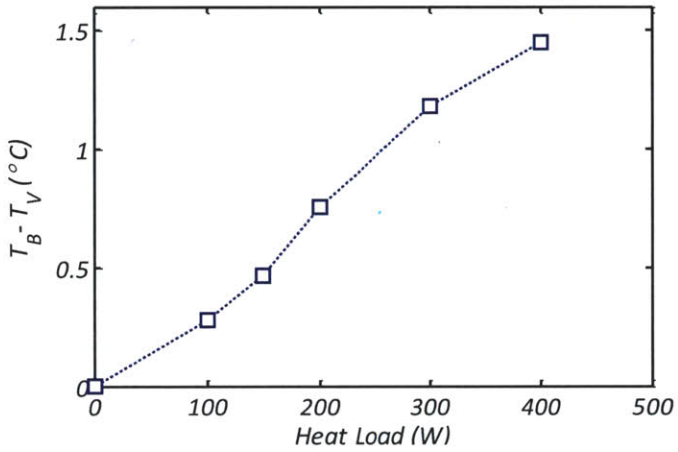

Figure 6.8. Temperature difference between the evaporator base and vapor, plotted against heat load. Data was taken at 5000 RPM. Measurement error for the temperature difference is 0.16 °C.

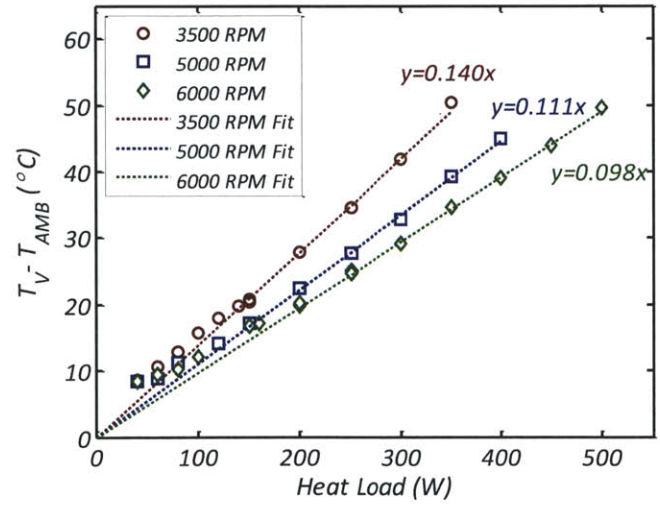

Figure 6.9. Temperature difference between the vapor and ambient air, plotted against heat load, for different fan speeds. Data was taken for a fill volume of 91 mL. Measurement error for the temperature difference is 0.56 °C.

The experimental data closely match the linear fit curves for heat loads greater than 150 W, but depart from the fit curves for heat loads lower than 150 W. The linearity is due to the dominance of the convective resistance, which is constant for a given fan speed. The departure from linearity is due to the increase in the thermal resistance of the heat pipe. As predicted in Chapter 3, the low heat loads result in the flooding of the lower condensers, which effectively decreases the area available for convective cooling. This effect is shown in Figure 6.10. The thermal resistance of each operating point, defined as the temperature difference divided by the heat load, increases with decreasing heat load below 150 W. The details of flooding are discussing the following section.

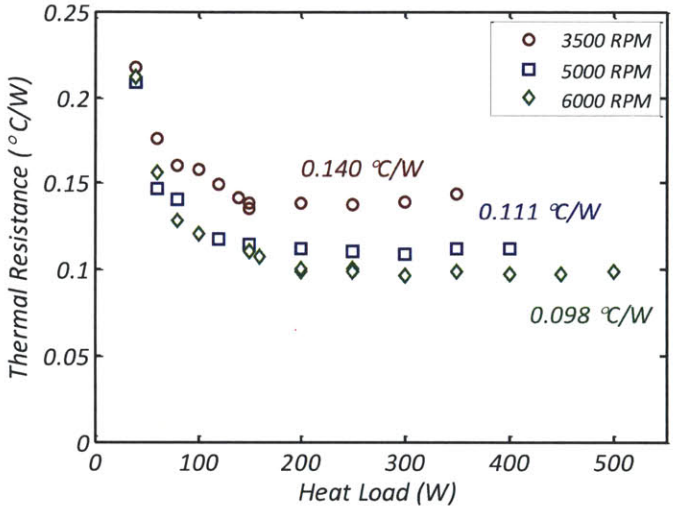

Figure 6.10. Thermal resistance, plotted against the heat load for different fan speeds. Data was taken for a fill volume of 91 mL. Measurement error for the temperature difference is 0.005 °C/W.

6.4.3 Phase Separation / Capillary Pressure in the Condenser

The capillary pressure in the condenser prevents flooding by separating the vapor and liquid phases, and is therefore a critical metric in understanding the thermal performance of the condenser. Figure 6.11 shows the difference between the vapor and liquid pressures, plotted against heat load and fan speed. The liquid pressure is measured at the exit of the lowest condenser. To calculate the capillary pressure, the viscous pressure drop through the condenser wick must be considered (Equation 4.1). Since this pressure drop could not be experimentally measured, the predicted pressure drops calculated from the wick properties are included in the figure. Like Figure 4.14 in Chapter 4, the experimental data are shown separately from the calculated values to avoid mixing the analyses. Following Equation 4.1, the capillary pressure is the difference between the vapor-liquid pressure difference and the viscous pressure drop.

Similar to the trends observed in Figures 3.6 and 5.14, the pressure difference increases with heat load due to the larger temperature difference between the vapor and CC at higher temperature. A capillary pressure of 5.3 kPa is achieved at 500 W and 60000 RPM. As the heat load is decreased, the capillary pressure in the lowest condenser approaches zero at 150 W, indicating the loss of a receding meniscus.

A sufficient temperature difference is not generated between the vapor and CC to fulfill the requirement of Equation 2.29. Below this threshold heat load, flooding occurs and liquid occupies the vapor space of the condenser. This mode of flooding will be referred to as "Type 3 flooding," to distinguish the mechanism from the other two modes described in Chapter 5. The movement of liquid into the vapor space results in the corresponding movement of vapor into the liquid space to fulfill volume conservation. As a result, liquid pressure measurement below 150 W becomes unreliable as the actual gravitational pressure head in the liquid pipe becomes uncertain. Since the pressure measurement of Figure 6.11 assumes a constant gravitational pressure head in which the entire liquid tube is filled with liquid, the negative pressures shown below 150 W are artifacts of the measurement method.

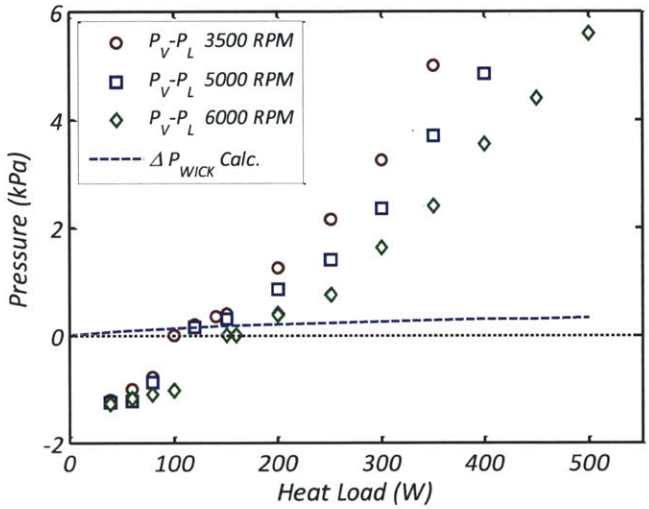

Figure 6.11. Pressures plotted against heat load. The experimentally measured difference between the vapor and liquid pressures are shown for the lowest condenser at three fan speeds. The predicted viscous pressure drop through the condenser wick is shown as the dotted line. Measurement error for the pressure difference is 0.1 kPa. Data was taken for a filling volume of 91 mL.

The effect of flooding on thermal performance is observed through the relative change in the condenser temperatures. Figure 6.12 shows the condenser surface temperature plotted against heat load. The temperature is non-dimensionalized through the following expression so that different temperatures can be plotted in a single graph.

$$\phi = \frac{T_V - T_{COND}}{T_V - T_{AMB}} \qquad 6.1$$

T_V, T_{COND}, and T_{AMB} are the vapor, condenser surface, and ambient temperatures, respectively. A larger value of Φ indicates a cooler condenser temperature and signifies flooding. Figure 6.12 shows the onset of flooding at 200 W, which approximately matches the threshold heat load from Figure 6.9, Figure 6.10 and Figure 6.11. Figure 6.12 also provides the additional information that the increase in thermal resistance observed in Figure 6.10 was due to the flooding of the two lowest condensers.

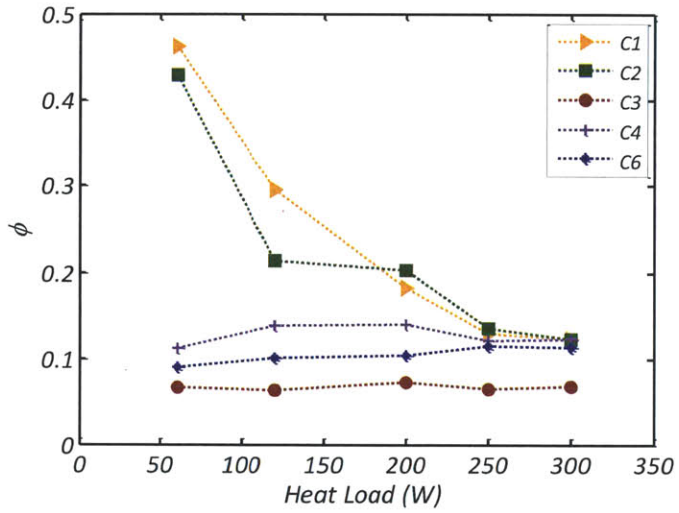

Figure 6.12. Non-dimensionalized condenser temperature plotted against heat load. The temperature of C5 is not shown due to a faulty thermocouple. Data was taken at 5000 RPM and 91 mL.

6.4.4 Effect of Filling Volume on Thermal Resistance

The dependence of the thermal resistance on the heat pipe filling volume was investigated to determine the proper filling volume. Figure 6.13 shows the difference between the vapor and ambient temperatures, plotted against the filling volume at 300 W and 5000 RPM. Over-filling the heat pipe results in liquid occupying the vapor space in the condenser, hence reducing the area available for condensation. This causes permanent condenser flooding, and increases the vapor temperature (thermal resistance). Over-filling is observed for volumes greater than 95 mL, which is the volume of liquid that exactly fills the liquid side of the heat pipe for the temperature tested. This volume approximately matches the calculated liquid side volume of 92.7 mL. Like the SCP, the difference in the calculated and measured volumes is predicted to be due to the presence of condensate at the cooler ends of the vapor tubes.

To function as designed, the heat pipe should be filled so that a two-phase region exists in the CC or the reservoir, depending on the operation mode (LHP or CPL). Thus, for a given temperature, the ideal range of volumes is defined by the ability to contain the vapor of the two-phase region in either the CC or the reservoir. The maximum vapor volume that can be contained in the CC is 5.6 mL, and thus the lower limit of this range is expected to be 89.4 mL. Similarly, the limit for the reservoir is expected to be 88.3 mL. These predicted volume ranges are marked in Figure 6.13. The vapor in the CC or reservoir compensates for the volumetric expansion of the liquid with temperature. The mechanism of the compensation is described in Chapter 5.

Filling volumes under the lower limits result in a vapor pocket in the liquid side that cannot be contained in the CC or reservoir. Despite this under-filling, the MCP was fully functional as a LHP. Operation was possible by using one of the liquid lines as an extension of the CC. In this case, one liquid line contained vapor while the other line returned the liquid to the evaporator. This was confirmed through

significantly different liquid tube temperatures, where one of the liquid tubes was closer in temperature to the vapor tubes than to the other liquid tube. While this results in a different liquid circulation path, the thermal resistance is not compromised, and therefore the practical range of "under-filled" is not clearly defined for the MCP in LHP operation. In contrast, the under-filled range is well defined for CPL operation, as will be discussed in a later section (Section 6.4.6) on liquid and vapor pressure control.

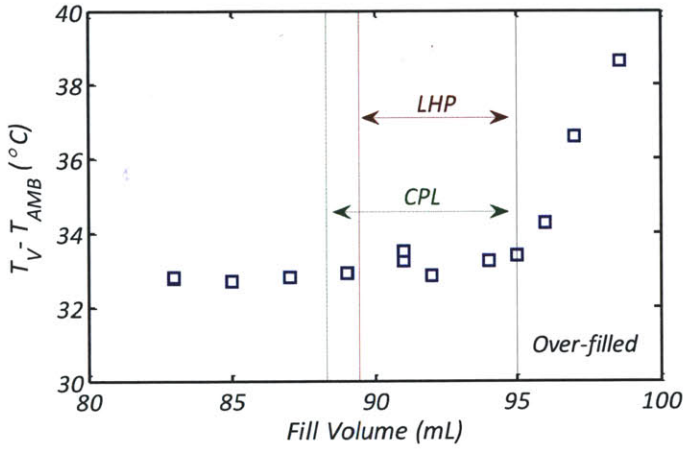

Figure 6.13. Temperature difference between the vapor and ambient, plotted against the filling volume. Data taken at 5000 RPM and 300 W. Measurement error for the temperature difference is 0.56 °C.

6.4.5 Effect of Orientation on Condenser Operation

As heat sinks are commonly mounted in the upright orientation as well as sideways, the MCP was tested in different orientations (tilt angles) to investigate the effect on thermal resistance. Figure 6.14 shows the difference between the vapor and ambient temperatures, plotted against the tilt angle for different heat loads. 150 W was included in the testing as an operating condition on the brink of flooding. The temperature difference for a given heat load represents the thermal resistance, which remains relatively constant for tilt angles between 0° and 110-120°. This result is indicative of phase separation in the condensers. The vapor and liquid occupy separate spaces in the condenser regardless of orientation, resulting in unchanged condensation behavior. Changes in liquid pressure from orientation changes are compensated by the capillary meniscus in the condenser. This is in contrast to the operation of LHPs with non-wicked condensers, where the change in the liquid pressure results in the movement of the condensation interface and a change in the thermal resistance [35].

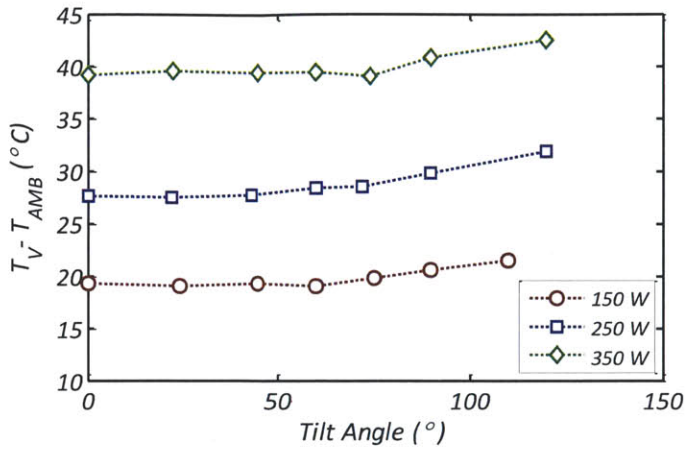

Figure 6.14. Temperature difference between the vapor and ambient, plotted against the tilt angle for different heat loads. Data taken at 5000 RPM and 91 mL. Measurement error for the temperature difference is 0.56 °C.

Tilt angles greater than 110-120°, however, resulted in a significant increase in thermal resistance which was frequently followed by heat pipe failure. This was observed at a lower tilt angle (110°) for 150 W, due to the lower condenser capillary pressures. Due to the lack of repeatability in achieving steady state operation, data for these angles are not shown in Figure 6.14. Figure 6.15 shows the vapor and condenser surface temperatures as a function of tilt angle. Little change in temperature occurs between 0° and 120°, as the MCP operates with near-constant thermal resistance. At 135°, however, the lower (top) condensers drop in temperature while the vapor temperature rises, indicating condenser flooding and an increase in thermal resistance. In contrast, the upper condenser rises in temperature since a larger heat load must be removed to compensate for the preformance degradation of the lower condensers. While the data for tilt angles between 0° and 120° was taken at steady state, the data for 135° was taken approximately 45 minutes into the experiment during a transient heat up towards heat pipe failure.

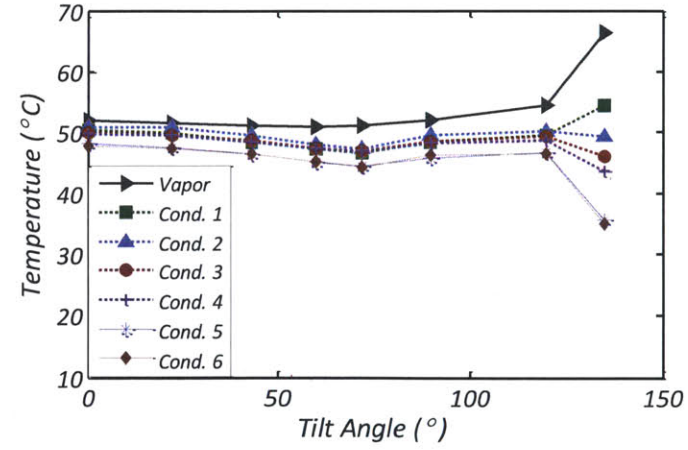

Figure 6.15. Temperatures of the vapor and condenser surfaces, plotted against the tilt angle. Data taken at 250 W, 5000 RPM and 91 mL.

Figure 6.16 shows the pressure difference between the vapor and liquid (CC), plotted against tilt angle for three heat loads. A positive pressure difference is maintained up to 90°, indicating phase separation. The data for tilt angles greater than 90° is not shown, as the gravitational pressure head in the liquid line and therefore the liquid pressure were not able to be determined. The data suggests, however, that a sudden decrease in the pressure difference occurred after 90° to cause the flooding-induced failure. A hypothesis of the cause is shown in Figure 6.17. Due to the non-adiabatic nature of the vapor line, condensation occurs along the tube walls. In the upright orientation, the condensate is gravity-fed back to the evaporator. In the semi-inverted case of 120-135°, however, the condensate flows away from the evaporator, accumulating at the end of the vapor line. Continued accumulation results in a liquid puddle that contacts the condenser wick, eliminating the capillary pressure. It should be noted that this hypothesis brings to question the long term stability of the heat pipe for any angle greater than 90°.

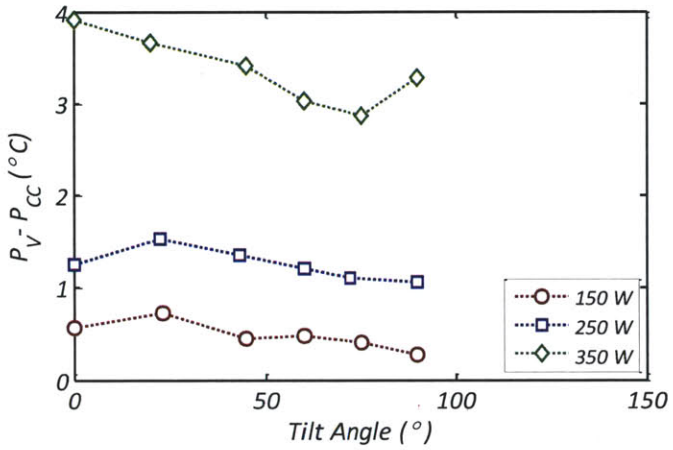

Figure 6.16. Pressure difference between the vapor and CC, plotted against the tilt angle, for different heat loads. Data is not shown past 90° due to the inability to calculate the liquid pressure. Data was taken at 5000 RPM and 91 mL. Measurement error for the pressure difference is 0.1 kPa.

To test the hypothesis, portions of the vapor tube were heated during inversion to mitigate the accumulation of the condensate. Kapton heaters (McMaster-Carr, *35475K423*) were attached to the extension of the vapor tubes, adjacent to the compression fitting joint that connects to the manifold. The extension was the only location on the vapor line where the heater could be attached, due to the close stacking of the condensers. A T-type thermocouple (Omega Engineering, *5TC-TT-T-40-36*) was also attached to the pipe for temperature control. A simple on-off type feedback control was implemented through the data acquisition system. The raw data of the vapor line, liquid line, and vapor tube extension temperatures are shown in Figure 6.18. The tube extension was first heated to a temperature higher than the vapor temperature before tilting. The MCP was tilted to 135° at 895 seconds. This is shown in the plot as the onset of the vapor and liquid temperature rise. At 1163 seconds, the tube heater was turned off, resulting in an immediate drop in the tube extension temperature. The effectiveness of the tube heating can be seen in the subsequent increase in the temperature rise rate of the vapor and liquid lines. The heat load was turned off at 1320 seconds to prevent damaging the MCP.

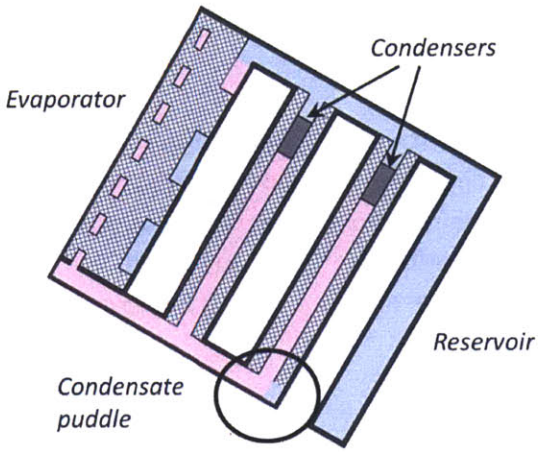

Figure 6.17. Effect of condensate puddle in the vapor line. Condensate in the vapor line connects with the liquid in the condenser wick, diminishing the condenser capillary pressure and inducing flooding.

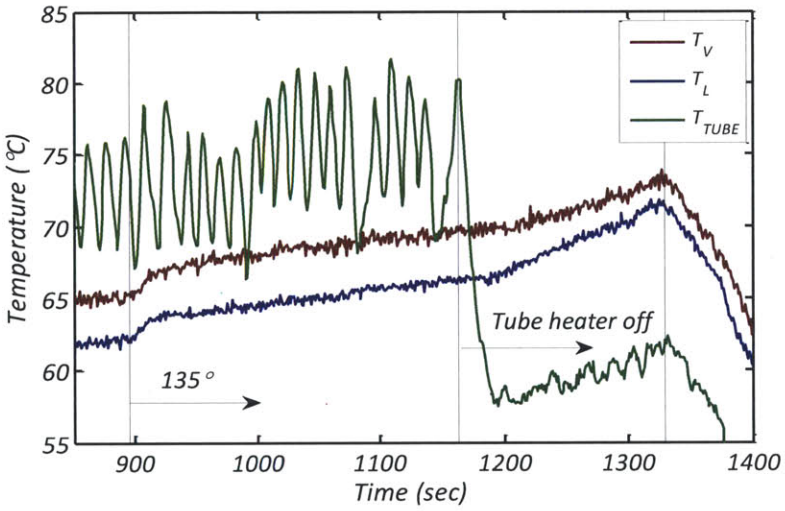

Figure 6.18. Temperatures of the vapor, liquid and the heated portion of the vapor tube at 350 W and 5000 RPM. Data shows the transition to a 135° tilt angle and the subsequent heat pipe failure. Filling volume was 91 mL. Measurement error for each thermocouple is 0.5 °C.

Figure 6.18 suggests that the hypothesis is true. While the application of the heater did not completely prevent the increase in vapor temperature, the rate of temperature increase towards heat pipe failure was suppressed. This behavior is likely due to the location of the heater: sufficient heating of the vapor line was not possible due to the location of the heating. The experimental conditions therefore depart from the ideal case of an adiabatic vapor line through direct heating.

The hypothesis can be used to draw a provisionary design modification. The accumulation of the condensate can be eliminated by the integration of the wick liner inside the vapor line that connects to

either the condenser wick or the evaporator wick. Any condensation will occur on the wick surface, ensuring vapor-liquid phase separation. Connection to the condenser wick will direct the condensate flow to the liquid line, whereas connection to the evaporator wick will return the condensate to the evaporator for vaporization.

6.4.6 Liquid and Vapor Pressure Control (CPL operation)

The MCP was tested in CPL mode to characterize liquid and vapor pressure control. Figure 6.19 shows the liquid pressure as a function of the reservoir temperature for different filling volumes. Similar to Figure 5.18, the expected liquid pressure curves for the LHP (blue line) and CPL (red line) modes are superposed. A transition between the two modes occurs at approximately 54°C. The vapor pressures are shown in the same layout in Figure 6.20.

6.4.6.1 General Operation: Three Modes

In general, the liquid and vapor pressures show the same trends as those observed in the SCP, and are separated into three modes (Figure 6.20).

I In LHP mode at lower reservoir temperatures, the vapor pressure does not respond to the increase in reservoir temperature. The vapor pressure is higher than the liquid pressure by the condenser capillary pressure and the requirement of Equation 2.29 is met. At higher temperatures (> 51 °C), the vapor pressure rises with reservoir temperature due to the heat transfer from the heated reservoir to the remainder of the heat pipe, which effectively increases the heat load. Due to the redesign of the reservoir, this vapor pressure increase is less than that of the SCP. The liquid pressure is minimally affected by the reservoir temperature as saturation is held in the CC.

II Increase of the temperature past 54°C results in the transfer of saturation from the CC to the reservoir, and the heat pipe operates as a CPL. The liquid pressure increases with the reservoir temperature through the saturation curve. Similar to the SCP, the match of the liquid pressure and the saturation pressure of the reservoir depends on the filling volume. In this temperature range, condenser flooding is avoided while the capillary pressure required in the condenser is decreased, and Equation 2.37 is still met.

III Further increase of the reservoir temperature (> 57°C) results in the liquid pressure meeting the vapor pressure, diminishing the capillary pressure in the condenser and causing Type 1 flooding. Loss of capillary pressure in the condenser signifies that Equation 2.29 is not satisfied. The vapor and liquid pressures become approximately equal, and follow the saturation curve. The transition is seen in Figure 6.20 through the change in the slope of the vapor pressure trace, as the mechanism of the pressure increase changes. Operation with Type 1 flooding equates to a conventional CPL operating in the variable conductance mode, as the condenser wick is no longer utilized and the increase in reservoir temperature is directly reflected in the vapor pressure.

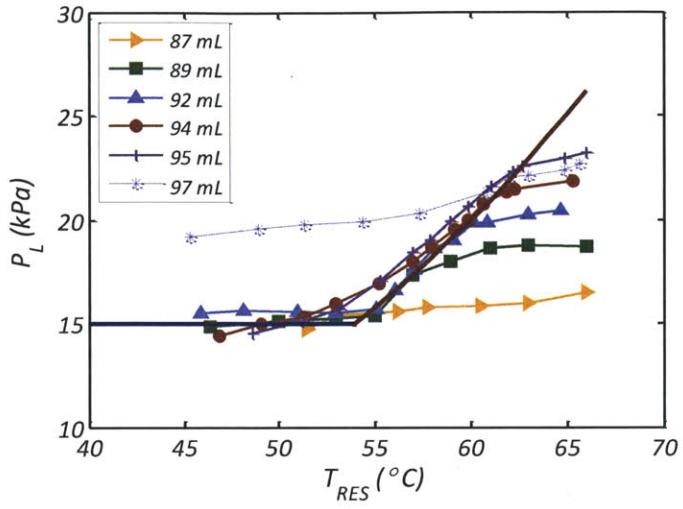

Figure 6.19. Liquid pressure, as a function of the reservoir temperature for different filling volumes. Data was taken at 5000 RPM and 300 W. Measurement error is 0.15 kPa.

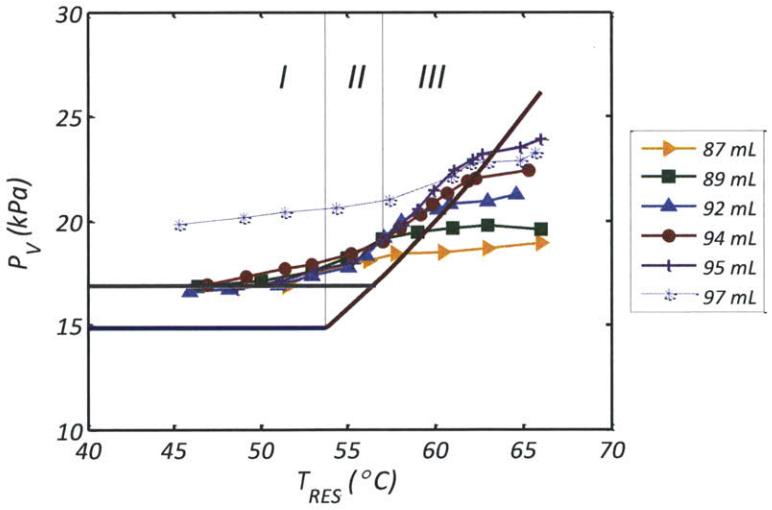

Figure 6.20. Vapor pressure, as a function of the reservoir temperature for different filling volumes. Data was taken at 5000 RPM and 300 W. Measurement error is 0.15 kPa.

6.4.6.2 Effect of Filling Volume and Reservoir Depletion

The degree of liquid pressure control in modes II and III depends on the filling volume. Under-filling results in a two-phase region with a vapor volume larger than the reservoir, and temperature control of the reservoir does not affect the interfacial (saturation) temperature. This is observed at 87 mL, as the liquid pressure changes little with reservoir heating. The vapor pressure increases only due to the higher effective heat load, and Type 1 flooding does not occur. As the degree of under-filling is

decreased, the vapor volume of the two-phase region decreases, eventually fitting within the reservoir. As a result, for filling volumes between 89 and 95 mL, the liquid pressure matches the saturation pressure of the reservoir temperature, and the match improves with higher filling volumes. Due to the redesign of the reservoir, this volume range matches the expected range shown in Figure 6.13. High reservoir temperatures allow for vapor pressure control through Type 1 flooding. Filling volumes greater than 95 mL result in over-filling (Type 2 flooding), increasing the pressures through higher temperatures, which agrees well the maximum liquid-side volume measured in Figure 6.13.

With proper filling in the SCP, the liquid and vapor pressures followed the saturation pressure of the reservoir for all temperatures tested in Type 1 flooding (mode III). A clear range of properly-filled volumes was not seen for the MCP, however, as increasing the filling volume resulted in over-filling before the liquid and vapor pressures continuously followed the reservoir saturation pressure. This is caused by the mechanism of pressure increase during Type 1 flooding. Figure 6.21 shows a schematic of the liquid distribution in the MCP, starting with the onset of Type 1 flooding (a). An increase in the reservoir temperature results in:

1) An increase in the liquid pressure through an increase in the saturation pressure of the reservoir.
2) An increase in the vapor pressure due to the absence of capillary pressure in the condenser.
3) An increase in the vapor temperature, since the vapor pressure and temperature are related through saturation.
4) An increase in thermal resistance to allow for the increase in the vapor temperature. Liquid is transferred from the reservoir to the (lowest) condenser to decrease the condensation space through flooding.

Thus, the ability of the reservoir to control the vapor temperature (pressure) during operation in Type 1 flooding is dependent on the ability of the reservoir to flood the condensers (b). In the MCP, the requirement for significant condenser flooding at high reservoir temperatures leads to the depletion of the liquid in the reservoir (c). As a result, the reservoir becomes filled with vapor, losing control of the liquid and vapor pressures. This was not observed in the SCP due to the ability of the reservoir (8.9 mL) to completely flood the vapor space of the single condenser (2.6 mL). Since the reservoir in the MCP (6.7 mL) is insufficient for completely flooding all of the condensers (2.6 x 6 = 15.6 mL), Type 1 flooding is possible only in a limited range of temperatures.

To assess the effect of the reservoir size on the temperature range available for variable conduction mode, it is useful to calculate the increase in vapor temperature achieved through the depletion of the reservoir. At the threshold filling volume of 95 mL, 6.7 mL is available to flood a maximum of 2.3 condensers. The lowest condenser contributes approximately 10-15% to the total cooling [30]. However, the vapor pressure rise due to Type 1 flooding is 5.0 kPa, from 18 to 23 kPa. This translates to a 5.3 °C (from 57.8 to 63.1 °C), *i.e.* a 15 %, increase in vapor temperature and thermal resistance. While the performance of a flooded condenser is not known, the results suggest that not all of the liquid in the reservoir is used for flooding. Although the liquid distribution in the heat pipe cannot be conclusively determined from the data, it is likely that some of the reservoir liquid entered the vapor lines after flooding the lowest condenser.

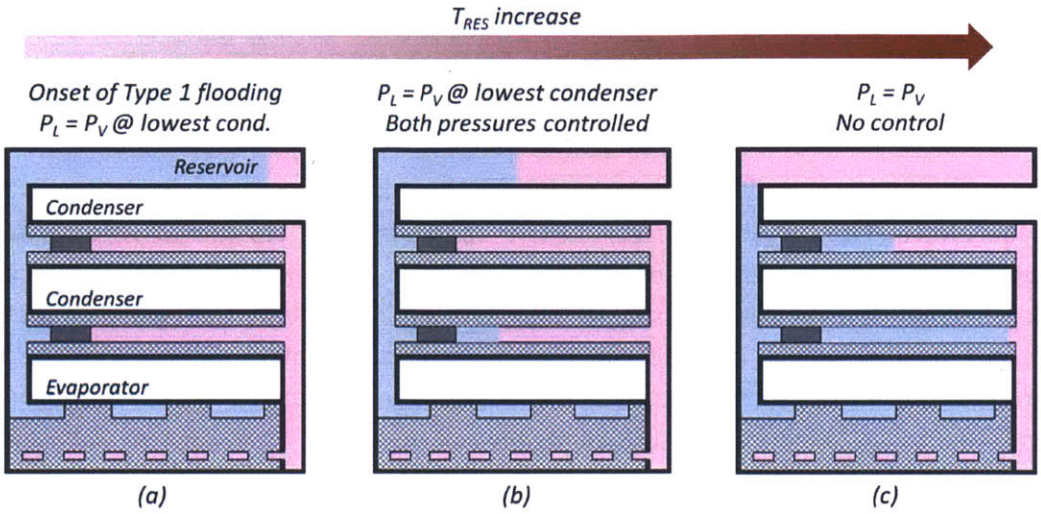

Figure 6.21. Schematic of the liquid distribution in variable conduction mode, showing a) the onset of Type 1 flooding, b) the use of the reservoir liquid for flooding, and c) the depletion of the reservoir liquid. Pink and light blue regions indicate vapor and liquid, respectively. The hatched sections indicate the wicks.

Liquid depletion in the reservoir also occurs in the over-filled case. When over-filled, the vapor and liquid pressures are equal, at a higher value than that expected for an under or properly filled case. The small increase in pressures as the reservoir temperature is increased from 45 to 60 °C is due to the increased condenser flooding from the thermal expansion of the liquid, as described in Chapter 5. The effect of the thermal expansion is significantly less than that observed for the SCP because the expansion constitutes a smaller fraction of the total condenser vapor space. Further heating of the reservoir results in the reservoir temperature matching that of the vapor, and Type 1 flooding occurs through a saturated reservoir (60 – 62 °C). The vapor and liquid pressures cross the saturation curve at 62 °C as the liquid in the reservoir is depleted and direct pressure control is lost. Type 1 flooding was not demonstrated for the over-filled SCP due to the high temperatures and pressures involved.

6.4.7 Summary of Filling Volumes

Figure 6.22 summarizes the effects of the filling volumes on LHP and CPL operation. The MCP was operated as a LHP with constant thermal resistance from 83 to 95 mL. Any filling volume greater than 95 mL resulted in over-filling, with an absence of phase separation in the condenser and high thermal resistance. For consistency with the analysis of the SCP, "properly filled" will specifically refer to the volumes that allow for variable conductance CPL operation for an unrestricted range of temperatures. Thus, while the MCP has an under-filled volume range in which the reservoir is not functional, a properly filled range was not observed due to the sizing of the reservoir.

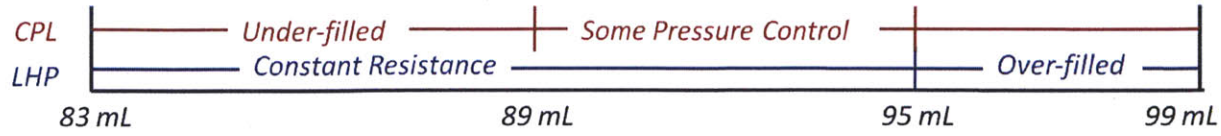

Figure 6.22. Ranges of filling

However, the effectiveness of the reservoir in CPL operation must considered with respect to its intended purpose: 1) To alleviate the requirement of Equation 2.29 and allow for heat pipe operation with condensers with low capillary pressure, and 2) to artificially increase the heat pipe temperature through Type 1 flooding, which leads to variable conductance operation. Thus, since the reservoir provides enough liquid pressure control to span the range underlying Equation 2.29, it is sufficient for 1). This is seen by the ability to induce Type 1 flooding, which is the limit of Equation 2.29. To achieve 2) for a thermal resistance increase of more than 15 %, the reservoir should be sized to be larger the total volume of the condenser vapor space. To retain the capability to operate as both LHP and CPL, the proper filling volume will be determined by the containment of the two-phase vapor volume in the CC. Hence, it should be noted that the use of a larger reservoir with a large two-phase region will necessitate a priming procedure prior to startup. The current reservoir size is therefore appropriate for a heat sink tailored towards low thermal resistance with automatic startup without priming.

6.5 Summary

A MCP was developed by integrating a six condenser heat pipe with a six-impeller fan assembly. The heat pipe includes a reservoir for operation as both LHP and CPL. Similar to the SCP, three operational modes are characterized. The first mode is the LHP operation, in which the reservoir is either unheated or at a temperature lower than the CC. The lowest thermal resistance is achieved in this mode, and therefore the thermal resistance and the condenser capillary pressure was characterized for LHP operation as a function of heat load, filling volume and orientation. The second is the CPL operation where phase separation is maintained in the condenser, but with lower capillary pressure than in the LHP mode. The reservoir is used to increase the liquid pressure to decrease the capillary pressure. The third mode is the CPL operation with flooded condenser(s). The degree of flooding is controlled with the reservoir, and the thermal resistance is increased, resulting in the increase of the vapor pressure and temperature.

The thermal performance of the MCP was tested in LHP operation. A thermal resistance of 0.1 °C/W was achieved at 6000 RPM, for a heat removal of 500 W at a base-to-air temperature difference of 50 °C. High heat loads (> 150 W) led to the formation of a receding meniscus for vapor-liquid phase separation; capillary pressures of up to 5.3 kPa were measured in the lowest condenser. Phase separation prevented flooding and ensured equal condenser operation. As predicted in Chapter 3, lower heat loads (< 150 W) resulted in an insufficient pressure difference between the vapor and the liquid, causing Type 3 flooding of the lower condensers. In addition, the MCP operated with constant thermal

resistance for a wide range of filling volumes, as under-filling was compensated by vapor not only in the CC, but also in one of the liquid lines. In contrast, over-filling resulted in the flooding of the condenser (Type 2 flooding), eliminating the capillary pressure and increasing the thermal resistance of the heat pipe. The MCP demonstrated nearly constant thermal resistance for orientation angles between 0 and 110°, but showed an increase in thermal resistance at 120-135° due to flooding in the lower condensers. This is hypothesized to be caused by the accumulation of liquid at the ends of the vapor lines.

The control of the liquid and vapor pressures was tested in CPL operation. The reservoir was used for liquid pressure control in the second mode of operation. The vapor pressure was not affected due to the capillary pressure in the condenser. The degree of vapor pressure control in the third mode was dependent was possible for a limited range of pressures. This was due to the limited volume of liquid available in the reservoir to flood the condensers (Type 1 flooding). The second and third modes of operation can be used to decrease the condenser capillary pressure and actively increase the thermal resistance of the heat pipe.

In summary, the air-cooled six condenser heat pipe was confirmed to remove up to 500 W with equal condenser performance, and is the proof-of-concept of the novel heat pipe-heat sink developed in this thesis. Additionally, mechanisms of condenser flooding were investigated and their relationship to operational limits was characterized for the multiple-condenser layout.

(This page intentionally left blank)

7 Summary and Conclusions

7.1 Overview

Thermal management is increasingly becoming a challenge in the electronics industry, as rapid advancements in computational performance are accompanied by a concomitant increase in heat dissipation. Efficient air-cooling solutions with low thermal resistance are needed for the next generation of electronics. This thesis reports the development of an air-cooled loop-type heat pipe for the integration into a high performance air-cooled heat sink for cooling electronics. Heat pipes are characterized by low effective thermal resistance due to the use of the latent heat of vaporization to transfer heat. The heat pipe developed in this study utilizes multiple condensers to increase the air-cooled surface area and wicks are integrated into the condensers to ensure equal functionality and prevent condenser flooding. Flooding decreases the area available for condensation and increases the heat pipe thermal resistance. In the development process, the heat pipe layout was first modeled analytically to determine the required wick properties. The results of the analytical model were then used for a more detailed component modeling of the evaporator. The details of the condenser design are described in reference [66]. Single-condenser and multiple-condenser prototypes were fabricated to demonstrate that capillary pressure can be generated in the condenser and that the condenser wicks are a viable approach to maintaining equal condenser performance. The prototypes confirmed that the following four objectives, as presented in Chapter 1, were accomplished.

5) Immediate startup upon the application of heat.
6) Operation with equal and optimal performance in all condensers.
7) Operation with a low heat pipe thermal resistance (<<0.05 °C/W), with the option of higher thermal resistances, as set by the operator.
8) Operation in a range of angles with constant thermal resistance.

This chapter summarizes the development process, highlighting the key features of the heat pipe. The implications of the heat pipe characteristics on the operation of the heat sink are also presented.

7.2 Design

The heat pipe was designed in a two-stage process, consisting of a nodal, analytical analysis of the entire heat pipe followed by a detailed, computational analysis of the evaporator.

7.2.1 Operating Characteristics of the Heat Pipe

The analytical analysis was directed at determining the requirements for forming capillary pressure on the surface of the condenser wick. The capillary pressure compensates for the gravitational liquid pressure difference in the individual condensers and is critical for separating the vapor and liquid phases, preventing the free movement of the liquid that results in a flooded condenser. The capillary pressure

generated in the condenser therefore ensures equal condensation behavior and thus low thermal resistance of the heat pipe.

In the context of the heat pipe cycle, vapor and liquid pressures must be regulated such that a pressure differential is maintained across the condenser wick meniscus. The vapor pressure is determined by the saturation temperatures at the vapor channels (evaporator) and in the condensation space (condenser). Since the two temperatures are related, only one of the temperatures is sufficient for the analysis. For LHP operation, the liquid pressure is typically determined by the saturation temperature of the compensation chamber, or CC (evaporator). The requirements for forming a receding meniscus are therefore the following: 1) Establishing a higher vapor pressure than that of the liquid, which requires a temperature difference between the vapor channels and the CC, and therefore an evaporator wick with low thermal conductivity. 2) Maintaining a stable saturation condition in the CC by preventing vaporization at the exit of the condenser wick. The condensate must therefore be thermodynamically sub-cooled prior to exiting the wick. Thus, for equal and full condenser functionality, specific thermal properties are necessary in both the condenser and evaporator. The analytical model was developed to evaluate the extent to which these requirements can be met with different wicks. The following list summarizes the modeling results. While modeling was performed for LHP operation, the results can be applied to CLP operation by evaluating saturation in a heated reservoir in place of the CC. The analytical model gave insight to the following trends:

1. With the use of high permeability wicks in the evaporator and condenser, the total viscous pressure drop of the cycle can be decreased to below 2kPa. In this case, the primary pressure drop becomes the capillary pressure in the condenser, and most of the capillary pressure generated at the evaporator is used to pump against the condenser capillary pressure.
2. The temperature difference between the vapor channels and the CC increases with heat load. This causes the condenser capillary pressure to increase also.
3. At lower heat loads, the vapor temperature is too low to establish a sufficient temperature difference with the CC. Capillary pressure is not generated in the condenser and flooding occurs, beginning with the lowest condenser. For the modeled case, the threshold heat load for flooding is approximately 100 W for the upright orientation and greater than 300 W for the inverted orientation, and depends on the thermal conductivity of the evaporator wick. The possibility of capillary pressure with an advancing meniscus is neglected; experiments showed that the advancing capillary pressure in sintered metal wicks is negligible due to surface defects.
4. Due to the effect described in (2), a design with a low threshold heat load results in significant capillary pressure in the condenser at high heat loads. The condenser wick must have a maximum capillary pressure greater than this pressure.
5. A high condenser permeability increases the condenser capillary pressure for a given temperature difference between the vapor and CC. This effect is greater for permeabilities below $2*10^{-13}$ m^2.
6. For sufficient sub-cooling of the condensate, the thermal conductivity of the condenser wick should be low ($\leq$ 40 W/m-K). Larger thermal conductivities can be used, however, with a larger section of the condenser dedicated to sub-cooling.

7. The results of the model were compared with the propertied of actual sintered metal wicks. Suitable wicks were found to be: a thermally insulating Monel 400 (<44 μm) wick in the evaporator, with a high permeability copper 40-90 μm, copper 40-75 μm or the Monel wick in the condenser.

7.2.2 Evaporator Development

The evaporator was designed using two and three-dimensional computational modeling. The design focuses on 1) generating high capillary pressure for driving the cycle, 2) stable operation with superheated liquid in the wick, 3) low thermal resistance between the base and the vapor exiting the evaporator, and 4) establishing a thermal gradient across the wick. A three-layer, monolithic wick was developed based on these goals and experiments were performed to confirm that these four goals were met. The following lists the key features of the evaporator development as well as the performance.

1. The three-layer, monolithic wick consists of:
    - A fine powder, high thermal conductivity, copper wick interfaces the copper base of the evaporator to the vapor channels to decrease the conductive thermal resistance through the wick and provide high capillary pressure.
    - A low thermal conductivity Monel 400 wick separates the vapor channels and the CC. A thermal gradient is formed across this wick.
    - A high permeability copper wick surrounds the CC, allowing fluidic access to the vapor channels in the presence of vapor in the CC. The wick also facilitates the cooling of the CC by providing a thermal connection to the air-cooled top surface.
2. The geometry of the vapor channels and the high thermal conductivity wick was designed with two and three-dimensional modeling to minimize the thermal resistance of the evaporator. The thermal resistance was experimentally measured to be 0.003 °C /W at 100 °C, matching the model prediction.
3. The shapes of the low thermal conductivity wick and the high permeability wick were designed through three-dimensional modeling to maintain a thermal gradient between the vapor channels and the CC. The model prediction of this temperature matched the experimental measurements for the vapor temperatures tested (37 – 50 °C).
4. A fabrication procedure was developed for the layered wick structure, consisting of a series of sintering steps that begins with high temperatures and ends with low temperatures.
5. The evaporator was tested on a custom heat pipe cycle with a liquid superheat and capillary pressure of approximately 14 kPa without signs of failure.

7.3 Prototype Characterization

Two prototypes were constructed and tested, of single-condenser (SCP) and multiple-condenser (MCP) formats. The SCP confirmed the successful operation of the novel heat pipe cycle with phase separation in the condenser, as well as dual-mode LHP and CPL operation. The MCP confirmed the operation of the

multiple-condenser layout with equal condenser performance and is the proof-of-concept of the heat pipe cycle developed in this thesis. Similar tests were performed on both prototypes; the characteristics of each are listed together below.

7.3.1 Startup

Automatic heat pipe startup was demonstrated by applying a heat load to the evaporator. Both SCP and MCP were started as LHPs, and CPL operation was achieved by heating the reservoir. Due to the dual mode (LHP and CPL) characteristic of the prototypes, the conventional priming procedure was not required for startup. Both SCP and MCP started in approximately 20 seconds after the application of heat, and startup was observed for all heat loads greater than 75 W and 40 W, respectively. Both prototypes achieved steady state in approximately 30 minutes.

7.3.2 Thermal Resistance and Condenser Functionality

1. Phase separation was achieved in the condenser(s) though capillary pressure for both prototypes in LHP mode. The capillary pressure was determined by measuring the difference in the vapor and liquid pressures, and was observed for all heat loads tested in the SCP. The capillary pressure in the MCP was in good agreement with the behavior predicted in the analytical model: the condenser capillary pressure approached zero at lower heat loads. The threshold heat load was measured to be 150 W, below which flooding (Type 3 flooding) was observed. It should be noted, however, that flooding at low heat loads is not a large concern for a heat sink application, as the electronics will be sufficiently cooled. Furthermore, the increase in vapor temperature due to Type 3 flooding is self-correcting, since a larger temperature difference will be generated between the vapor channels and the CC.
2. A constant thermal resistance was observed for the range of heat loads with capillary pressure in the condenser. The thermal resistance between the vapor and ambient air was measured to be 0.177 °C/W for the SCP at 5000 RPM, and 0.1 °C/W for the MCP at 6000 RPM. The thermal resistance of the multiple-condenser heat pipe was approximately 0.0065 °C/W.

7.3.3 Effect of Orientation

1. The MCP was operated with tilt angles from 0 to 110° with little change in thermal resistance, indicating that the heat pipe can be mounted and operated sideways. Phase separation in the condenser maintained constant condensation behavior for these angles.
2. The thermal resistance rapidly increased beyond a tilt angle of 120° and frequently led to heat pipe failure. The capillary pressure in the lowest condensers was lost, and flooding was observed.
3. The flooding at the higher angles is hypothesized to be due to the accumulation of the condensate at the ends of the vapor line. The puddle of liquid contacts the condenser wick, destroying the capillary pressure.

7.3.4 Liquid and Vapor Pressure Control

The reservoir was used for liquid and vapor pressure control, which is separated into three modes. Both prototypes demonstrated a seamless transition between the LHP and CPL modes as the two-phase region was relocated from the CC to the reservoir.

1. **(I)** *LHP operation, receding meniscus in condenser:* At low reservoir temperatures, the two-phase region is located in the CC and both liquid and vapor pressures are largely unaffected by the reservoir temperature. The vapor pressure is greater than the liquid pressure, and a receding meniscus is formed in the condenser.
2. **(II)** *CPL operation, receding meniscus in condenser:* Increasing the reservoir temperature leads to the relocation of the two-phase region from the CC to the reservoir, and the liquid pressure follows the reservoir saturation pressure. While the vapor pressure is still greater than that of the liquid, increasing the reservoir temperature increases the liquid pressure, which decreases the capillary pressure in the condenser.
3. **(III)** *CPL operation, flooded condenser:* Further increase of the reservoir temperature diminishes the vapor-liquid pressure difference and the vapor and liquid pressures become equal. The capillary pressure in the condenser is lost and flooding is induced (Type 1 flooding). An increase in the reservoir temperature leads to an increase in the vapor pressure through the saturation curve. A corresponding increase in the vapor temperature occurs as the flooding of the condenser increases the thermal resistance.
4. Mode I allows for operation with the lowest thermal resistance. Mode II allows for the use of condensers with low capillary pressure, as the condenser capillary pressure is manually decreased. Mode III results in an operator-defined thermal resistance, where the vapor pressure and temperature are controlled through the reservoir. This mode is identical to the variable conduction mode of conventional CPLs without wicks in the condensers.

7.3.5 Effect of Filling Volume

The operating characteristics of the heat pipe were dependent on the filling volume, and three ranges were observed.

1. *Over-filled:* The vapor and liquid spaces of the heat pipe are physically bounded by the evaporator and condenser wicks. Filling the heat pipe with a liquid volume greater than the liquid space resulted in excess liquid occupying the vapor space of the condenser. The over-filled case is characterized by a permanently flooded (Type 2 flooding) condenser, with an increased thermal resistance and vapor temperature for a given heat load.
2. *Under-filled:* Insufficient filling results in a two-phase (vapor) region in the liquid side that is larger than the CC or reservoir. Both prototypes were fully functional as LHPs despite under-filling; it is likely that one of the liquid lines was used as an extension of the CC to contain the extra vapor. Since the reservoir was completely filled with vapor in CPL operation (modes II and III), little or no liquid and vapor pressure control was possible for the under-filled range.
3. *Properly filled:* Proper filling is characterized by the two-phase vapor region in the liquid side that is fully contained in the CC or reservoir. As thermal resistance was unchanged for LHP operation from the under-filled case, the range of volumes defined as properly filled was based on the CPL performance. Proper filling in the SCP allowed for complete control of liquid and vapor pressures in modes II and III. The MCP, however, did not exhibit full liquid and vapor pressure control in mode III even with the two-phase region contained in the reservoir. This

behavior is attributed to the sizing of the reservoir; the reservoir supply of liquid is insufficient for flooding all of the condensers.

7.3.6 Types of Flooding

Four types of flooding were observed, and are summarized in the list below. Flooding was indicated by the increase in heat pipe thermal resistance and the loss of capillary pressure in the condenser(s). Flooding was either permanent or dependent on the operating conditions.

1. *Type 1 (conditional):* High reservoir temperatures in mode III induces flooding in the lowest condenser(s).
2. *Type 2 (permanent):* Overfilling the heat pipe results in excess liquid which occupies the condensation (vapor) space in the condenser. This prevents the formation of the capillary meniscus, and the condenser is permanently flooded.
3. *Type 3 (conditional):* In the MCP, low vapor temperatures at low heat loads results in an insufficient temperature difference between the vapor channels and the CC, and capillary pressure is not generated in the lower condenser(s).
4. Flooding due to adverse orientation.

7.4 Considerations in Application and Future Work

The fundamental insights gained from testing the two prototypes can be used to conceive methods to extend the operating range of the multiple-condenser heat pipe. 1) If higher heat pipe temperatures can be tolerated, a careful control of the fan speed and reservoir temperature can extend the maximum heat load before the heat pipe fails. 2) Similarly, the maximum heat load can be increased by adding condensers. 3) Also, operation in a greater range of angle may be achieved by integrating a wick in the vapor line.

1. For a given heat pipe design and proper filling, the maximum heat load of the heat sink is limited by the maximum capillary pressure in the evaporator and condenser. The evaporator capillary pressure must overcome the condenser capillary pressure as well as the cumulative pressure drop of the cycle. The latter is a function of the mass flow rate. As shown in Chapter 3, the condenser capillary pressure is dominant at higher temperatures and heat loads. However, the experimental results show that the condenser capillary pressure can be reduced by 1) increasing the fan speed, and 2) increasing the reservoir temperature in mode II operation. Therefore, future work is suggested in implementing an active feedback control of the fan speed and reservoir temperature such that the capillary pressures of the condensers are not excessively high to avoid dry-out of the condenser wick. The heat load limit in this case is then predominantly determined by the evaporator capillary pressure, which becomes a function the mass flow rate. From Chapter 2, the cumulative pressure drop of the cycle for the wicks used in the present heat pipe is approximately 2 kPa at 1000 W. Since the evaporator demonstrated a capillary pressure greater than 14 kPa in Chapter 4, a larger heat load may be removed if the capillary pressure in the condenser is restrained. However, this argument does not consider the

physical robustness of the device, as higher heat loads will result in higher temperatures and moreover, substantially higher pressures.

2. To remove a higher heat load without higher operating temperatures and thus satisfy the DARPA metrics, the thermal resistance needs to be decreased. This can be accomplished by increasing the number of condensers and fan impellers in the heat pipe. Future work is suggested at correlating the decrease in thermal resistance with the addition of condensers to understand the number required to meet the DARPA metrics. An increase in the number of condensers is not expected to change the operating characteristics from that presented in Chapter 6.
3. For a fully orientation independent design, future work is suggested at eliminating the accumulation of the condensate. One method is the integration of a wick on the inner surface of the vapor line, which connects to either the condenser wick or the evaporator wick. Connection to the condenser wick will direct the liquid to the liquid line, whereas connection to the evaporator wick will return the liquid to the evaporator for vaporization. It is expected, however, that the manufacturing will be difficult, since this design requires the connection of wicks from two separate components.

7.5 Concluding Remarks

Despite the potential for high heat removal, loop-type heat pipes are currently only used in specialty applications. Furthermore, due to the dependence of the thermal resistance on the operating conditions, an intensive characterization is typically required before practical integration. The development reported in this thesis was directed at addressing the dependence of heat pipe performance on operating conditions by the incorporation of a wick in the condenser. While the goal of this effort was primarily to ensure the functionality of multiple condensers for a heat sink application, the thermal-fluidic relationships that were developed as the basis of vapor and liquid pressure control provide insights to how the effects of operating condition can be reduced by design.

(This page intentionally left blank)

A Appendix: MATLAB Code to Solve the Analytical Model

A.1 Function for Water Properties

```
function [prop] = properties(x)

vis_l_Tw_ex =5.8498E-08*x(3)^2 - 1.3970E-05*x(3) + 1.0962E-03;          %liquid viscosity, as a function of temperature of node (3)
vis_v_Tv =3E-08*x(1) + 9E-06;                                           %vapor viscosity, as a function of temperature of node (1)
dens_l_Tw_ex =-0.0026*x(3)^2 - 0.2009*x(3) + 1004.6;                    %liquid density, as a function of temperature of node (3)
dens_v_Tv = 1.2948E-06*x(1)^3 - 1.3379E-04*x(1)^2 + 7.7093E-03*x(1) - 1.2993E-01;
                                                                        %vapor density, as a function of temperature of node (1)
hfg_Tv = -2.5085E+03*x(1) + 2.5081E+06;                                 %vapor viscosity, as a function of temperature of node (1)
Cp_Tlsc = 0.0084*x(4)^2 - 0.5849*x(4) + 4189.8;                         %liquid specific heat, as a function of temperature of node
(4)
vis_l_Tcc=5.8498E-08*x(5)^2 - 1.3970E-05*x(5) + 1.0962E-03;             %liquid viscosity, as a function of temperature  of node (5)
dens_l_Tcc=-0.0026*x(5)^2 - 0.2009*x(5) + 1004.6;                       %liquid density, as a function of temperature of node (5)
Cp_Tcc = 0.0084*x(5)^2 - 0.5849*x(5) + 4189.8;                          %liquid specific heat, as a function of temperature of node
(5)

prop=[vis_v_Tv, dens_v_Tv, hfg_Tv, vis_l_Tw_ex, dens_l_Tw_ex, Cp_Tlsc, vis_l_Tcc, dens_l_Tcc, Cp_Tcc];
```

A.2 Function for the Heat Pipe Geometry, Material Properties and Saturation Curve for Water

```
%File name: Specifications
%_____________________________________________________________________
%setting values for geometry and material properties
Tamb=30;                    %ambient temperature for condenser
Tamb2=30;                   %ambient temperature for evaporator and liquid line
k_wick=2;                   %thermal conductivity of evaporator wick
l_wick=4*10^-3;             %thickness of primary wick
l_wick_cond=5*10^-4;        %thickness of condenser wick
r_shaft_space=22.5*10^-3;   %radius of shaft hole in condenser
r_condense_wick=42*10^-3;   %radius of condensation wick (doens't include subcool section)
k_body=25;                  %envelope therm. conductivity (defult-ss)
area_wick=88.8*10^-4;       %area of wick (evaporator)
area_wall=8*10^-4;          %area of walls and support strutures in wick
area_ev_conv=93.72*10^-4;   %area of convective surface on evaporator
```

```
d_pipe=6.4*10^-3;           %inner diameter of vapor and liquid pipes
d_pipe_out=9.5*10^-3;       %outer diameter of pipes
d_v_chan=2*10^-3;           %diameter (hieght=width) of vapor channel teeth
n_chan=10;                  %number of vapor channels in evap
cond_vap_space=5*10^-4;     %thickness of vapor space channel in condenser
cond_wick_space=5*10^-4;    %thickness of wick space in condenser
pore_c=0.42;                %porosity of condenser wick
pore_ev=0.42;               %porosity of evap. wick
perm_c=2*10^-13;            %permeability of condenser wick
perm_e=10^-13;              %permeaiblity of primary wick
plates=15;                  %number of plates
subcool=5*10^-3;            %subcooling wick length
l_c_l_chan=9*10^-2;         %length of flow of condensed liquid in condenser
w_c_l_chan=1*10^-3;         %width of flow of condensed liquid in condenser
cond_area=40.2*10^-4;       %available condensing area, 2 on each condenser(def=44.2)

l_pipe=0.005;               %both vapor pipe and liquid pipe same length
                                % l_pipe=0.005 for upright, =0.09 for
                                % inverted
l_pipe_avg=0.045            %average length for thermal calculations
l_ev_chan=0.05;             %length of evaporator vapor channels

h_c=100;                    %conv. heat transfer coeff. for cond
h_ev=100;                   %conv. heat transfer coeff. for evap

area_pipe=(d_pipe/2)^2*pi;  %vapor pipe line presure loss
area_v_evap=d_v_chan^2;     %evaporator vapor line pressure loss


%_____________________________________________________________________
%linearized saturation curve, separated into 10 degree (C) increments
%linearization is used to ease the computational effort
%T=dt*(P)+ct,   temperature linearization (coefficients)
%P=Ap*(T)+Bp,   pressure linearization (coefficients)

Tavg=(y(1)+y(2)+y(3)+y(4)+y(5)+y(7))/6       %average temperature of the cycle


if (Tavg>30) && (Tavg<40)       %coefficients for the temperature range of 30-40 degrees C
    dt=3.179E-03;
    ct=16.87;
    At=313.16;
    Bt=-5256.6;
    temp=30
end

if (Tavg>40) && (Tavg<50)       %coefficients for the temperature range of 40-50 degrees C
    dt=2.009E-03;
    ct=25.5;
    At=495.76;
    Bt=-12605;
```

```
    temp=40
end

if (Tavg>50) && (Tavg<60)        %coefficients for the temperature range of 50-60 degrees C
    dt=0.0013;
    ct=34.075;
    At=758.19;
    Bt=-25784;
    temp=50
end

if (Tavg>60) && (Tavg<70)        %coefficients for the temperature range of 60-70 degrees C
    dt=8.873e-4;
    ct=42.592;
    At=1123.9;
    Bt=-47799;
    temp=60
end

if (Tavg>70) && (Tavg<80)         %coefficients for the temperature range of 70-80 degrees C
    dt=6.16e-4
    ct=51.051;
    At=1619.5;
    Bt=-82585;
    temp=70
end

if (Tavg>80) && (Tavg<90)        %coefficients for the temperature range of 80-90 degrees C
    dt=4.387e-4;
    ct=59.448;
    At=2274.5;
    Bt=-135091;
    temp=80
end

if (Tavg>90) && (Tavg<100)        %coefficients for the temperature range of 90-100 degrees C
    dt=3.198e-4;
    ct=67.79;
    At=3121;
    Bt=-211410;
    temp=90
end

if (Tavg>100) && (Tavg<110)       %coefficients for the temperature range of 100-110 degrees C
    dt=2.381e-4;
    ct=76.07;
    At=4193;
    Bt=-318761;
    temp=100
end
```

```
%_____________________________________________________________________
%Constants for the radial fin (sub-cooler)
ex=0.8504;          % ex=(T_4-T_AMB)/(T_2-T_AMB), calculated using the Bessel function
%_____________________________________________________________________
%Resistances in the evaporator
Rwall=l_wick/(k_body*area_wall);        %conductive thermal resistance through evaporator case
Rwick=l_wick/(k_wick*area_wick);        %conductive thermal resistance through evaporator wick
Rww=1/(1/Rwick+1/Rwall);                %combined conductive thermal resistance of wick and case
Rconv=1/(h_ev*area_ev_conv);            %convective thermal resistance at the top surface of the evaporator
```

A.3 Function to Simultaneously Solve the Analytical Relations

```
function f = nle_lin(x)

Specifications;    %calls the function with the physical geometry of the heat pipe and the water saturation curve
global y
prop=properties(y);          %call the function with the water properties,
vis_v=prop(1);               %and rename
dens_v=prop(2);
hfg=prop(3);
vis_l=prop(4);
dens_l=prop(5);
Cp=prop(6);
vis_l_wick=prop(7);
dens_l_wick=prop(8);
Cp_cc=prop(9);

%_____________________________________________________________________
%formulation of the 7 equations to be solved simultaneously
%unknowns:
%x(1):  temperature at node 1
%x(2):  temperature at node 2
%x(3):  temperature at node 4
%x(4):  temperature at node 5
%x(5):  temperature at node 6
%x(6):  mass flow rate

dP_pri_wick=vis_l_wick*l_wick*x(6)/(perm_e*dens_l_wick*area_wick);          %liquid pressure drop across the evaporator wick
f(1)=-x(2)+dt*At*x(1)+dt*Bt-
dt*(1/(2*dens_v)*(x(6)/(2*area_pipe))^2*(64*vis_v*area_pipe*2/(d_pipe*x(6))*(l_pipe/d_pipe)+1.25)+1/(2*dens_v)*(x(6)/(area_v_evap*6*4)
)^2*(56.91*vis_v*area_v_evap*4*6/(d_v_chan*x(6))*(l_ev_chan/d_v_chan)+1.5))+ct;
                                                                            %vapor pressure drop through the capor channels and vapor

lines
f(2)=-x(3)+Tamb+(x(2)-Tamb)*ex;                                             %heat removal from the radial fin (sub-cooler)
f(3)=-x(4)+Tamb2+(x(7)-Tamb2)*exp((-h_c*l_pipe_avg*pipe_conv_area)/((x(6)/2)*Cp));  %cooling of the liquid as it flows throgh the
liquid line
f(4)=(1/Rww+x(6)*Cp_cc)*(x(1)-x(5))-Q+x(6)*hfg;                             %Kirkhoff's law a node 1
f(5)=(x(6)*Cp+1/Rconv)*x(5)-x(6)*Cp*x(4)+x(6)*hfg-Q-1/Rconv*Tamb2;           %Kirkhoff's law a node 6
f(6)=(0.22329+h_c*cond_area)*(x(2)-Tamb)-x(6)/(plates*2)*hfg;               %Kirkhoff's law a node 2
end
```

A.4 Function to Calculate the Pressures after the Temperatures are Solved (Main Function)

```
function [] = phump_lin();

global Q
global y
Specifications;                 %calls the function with the physical geometry of the heat pipe and the water saturation curve
prop=properties(y)              %call the function with the water properties,
vis_v=prop(1);                  %and rename
dens_v=prop(2);
hfg=prop(3);
vis_l=prop(4);
dens_l=prop(5);
Cp=prop(6);
vis_l_wick=prop(7);
dens_l_wick=prop(8);


x0=[80 80 80 80 80 0.0004, 80];                          %initial guess to start solver
options=optimset('MaxFunEvals',5000, 'Maxiter',5000);    %options on setting solver
x = fsolve(@nle_linR_step3_thesis,x0,options);           %solver
x=x';


dP_pipe=32*l_pipe/(d_pipe^2*area_pipe)*(x(6)*vis_l/(2*dens_l))      %liquid pressure drop through the liquid line
dP_wick=vis_l*x(6)/(4*plates*perm_c*l_wick_cond*pi*dens_l)*(0.5-r_shaft_space^2/(r_condense_wick^2-
r_shaft_space^2)*log(r_condense_wick/r_shaft_space))
                                                             %liquid viscous pressure drop through the condenser wick
dP_total=dP_pipe-dens_l*9.8*l_pipe+dP_wick;                  %total pressure drop between nodes (3) and (6). NOTE:(-) on pgh is
upright, (+) is inverted
Pcc=0.267*x(5)^3-30.81*x(5)^2+1730.3*x(5)-30572;             %saturation pressure of CC, use temperature to calculate
Pcond=0.267*x(2)^3-30.81*x(2)^2+1730.3*x(2)-30572;           %saturation pressure of vapor in condenser, use temperature to
calculate
Pw_ex=Pcc+dP_total-dP_wick;                                  %pressure at the exit of the condenser
Prec=Pcond-Pcc-dP_total;                                     %receding capillary pressure in the condenser wick
dP_pri_wick=vis_l_wick*l_wick*x(6)/(perm_e*dens_l_wick*area_wick);  %liquid pressure drop across the evaporator wick
Pv=0.267*x(1)^3-30.81*x(1)^2+1730.3*x(1)-30572;              %saturation pressure of vapor in the evaporator, use temperature
to calculate
Pcap=Pv-(Pcc-dP_pri_wick);                                   %receding capillary pressure in the evaporator wick
Pressure=[Pv, Pcond, Pcond-Prec, Pw_ex, Pw_ex, Pcc, Pcc, Pcc-dP_pri_wick, Pv]' % show list of pressures
deltaPs=[Prec, Pcap, dP_wick, dP_pri_wick]'                  %show list of pressure drops
heat_leak=Q-hfg*x(6)                                         %heat leak across the evaporator

mass_flow=x(6)                                               %show mass flow rate

Temps=[x(1) x(2) x(2) x(3) x(7) x(4) x(5) x(1) x(1)]'        %show list of temperatures in order of nodes: 1, 2, 3, 4, 5, 6, 7, 1
y=[x(1) x(2) x(2) x(3) x(7) x(4) x(5)];
```

(This page intentionally left blank)

B Appendix: Geometry and Properties Used in the Analytical Model

Table B.1. List of geometrical and material property values used in the analytical model.

Section of heat sink	Geometry or Property	Value	Units
Evaporator	Wick thickness	4	mm
	Wick thermal conductivity	1 - 10	W/m-K
	Wick permeability	$7.5*10^{-15}$ - $5*10^{-13}$	m^2
	Wick porosity	0.42	
	Wick area	88.8	cm^2
	Vapor channel cross section (height x width)	2 x 2	mm x mm
	Vapor channel length	5	mm
	Vapor channel developing flow loss coefficient	1.5	
	Number of vapor channels	10	
	Area of top surface	93.7	cm^2
	Height of compensation chamber	0	mm
	Evaporator case thermal conductivity	25	W/m-K
	Evaporator case thickness (sides | top)	2 | 1	mm | mm
	Evaporator footprint (length x width)	101.6 x 101.6	mm x mm
Condenser	Wick thickness	0.5	mm
	Wick thermal conductivity	25	W/m-K
	Wick permeability	10^{-13} - 10^{-11}	m^2
	Wick porosity	0.42	
	Condensation space thickness	0.5	mm
	Condensation area (inner|outer radius)	22.5 | 42	mm | mm
	Sub-cooler (radial) length	5	mm
	Liquid return channel cross section (height x width)	1 x 1	mm x mm
	Liquid return channel length	90	mm
	Number of liquid return channels	4	
	Height of lowest condenser	5	mm
	Height of upper condenser	90	mm
	Condenser case thermal conductivity	25	W/m-K
	Condenser case thickness (planar surface | edges)	1 | 2	mm
	Number of condensers	15	
	Condenser footprint (length x width)	101.6 x 101.6	mm x mm
Fluidic lines	Pipe length	90	mm
	Pipe inner diameter	6.4	mm
	Pipe outer diameter	9.5	mm
	Pipe developing flow loss coefficient	0.5	
Air-flow	Ambient temperature	30	°C
	Convective heat transfer coefficient	100	W/m^2-K

(This page intentionally left blank)

C Appendix: Heat Pipe Filling Station

C.1 Overview

This appendix describes the heat pipe filling station developed to remove non-condensable cases from the working fluid (water) and evacuate and fill the heat pipe with a prescribed volume of the working fluid.

C.2 Purpose and Methodology

Heat pipes are sensitive to the presence of non-condensable gases (NCs), such that the operating characteristics are altered. Startup in the presence of significant NCs requires the heating of the heat pipe to the saturation temperature of the total pressure, which includes the vapor pressure as well as the pressure of the NCs. Furthermore, the NCs have a tendency to accumulate in the condenser(s), decreasing the area available for condensation and increasing the thermal resistance [71]. This mechanism is used in variable conductance heat pipes to increase the thermal resistance [18-20].

Consequently, for a predictable and low thermal resistance heat pipe, it is critical to eliminate NCs from the working fluid prior to filling. Typical methods of de-gassing, or removing the NCs from the working fluid, consist of 1) boiling, to decrease the solubility of the NCs in the liquid, or 2) freezing to separate the working fluid from the NCs [18, 72-74]. The latter approach is adopted in this work, and will be referred to as "freeze-pump-thaw" (FPT). The working fluid is frozen by immersing the container in a bath of liquid nitrogen or a slurry of dry ice and alcohol. Upon freezing, the gaseous content in the container is evacuated by a vacuum pump. The working fluid is thawed, and the process repeated at least three additional times.

In addition to de-gassing the working fluid, NCs must be removed from the heat pipe. While this is typically performed prior to filling using a vacuum pump [18-20, 72-74], some researchers have used the heat pipe as the container for de-gassing *via* boiling or FPT [72]. In the latter procedure, some of the working fluid is inevitably lost. Consequently, the former method is used in this work, as the separation of the filling and de-gassing processes allows for a greater precision in controlling the filling volume. In this case, the de-gassed working fluid must be introduced to the heat pipe. This can also be performed in two different methods. The first method uses separate setups for the de-gassing and heat pipe evacuation. In some cases, syringes have been used to transfer the fluid from the de-gassing container to the heat pipe [75]. However, due to the moving seal in the syringe and the multiple transfers required, NC's are invariably introduced in the process. The second method performs both de-gassing and filling in the same apparatus [18-20, 72-74]. While this results in a significantly greater equipment size and cost due to the complexity of the fluidic and vacuum lines, the introduction of NCs are minimized. The present filling station employs the latter method.

C.3 Layout of the Filling Station

The layout of the filling station developed for this work is shown in Figure C.1. This section describes the layout; the operation is outlined in the following section (Section C.4). The valves are labeled in the figure with letters. A characteristic feature of this filling station is the central, four-way intersection between valves A, B, C and D. One leg of the intersection connects to the vacuum pumps through valve A. A liquid nitrogen trap is used to collect any condensable matter that is pulled by the vacuum pumps, and is a critical feature to prevent liquid from accidentally being ingested into the pumps. Through valve B, the second leg connects to the burette that is used to measure the volume of liquid that fills the heat pipe. The burette allows for a maximum volume measurement of 100 mL, with a resolution of 0.2 mL. The third leg connects to the de-gassing container (FPT tank) through valve C. Two lines access the FPT tank: one connects at the top of the tank for access to the vapor (NCs) and the second connects to the base of the tank for access to the liquid. The fourth leg connects to the heat pipe through valve D. Two vacuum pumps are used in tandem. Low vacuum is created by an oil-lubricated, rotary vane roughing pump (Adixen, Hingham, MA, *2010*), and the pressure measured by a thermocouple gauge (P_{LV}) with a range of 1-1000 mtorr, or 0.13-133 Pa (Teledyne-Hastings, Hampton VA, *DV-5*). An oil mist filter is used between the roughing pump and valve G to prevent a diffusive flow of oil mist into the vacuum. The turbomolecular pump (Pfeiffer Vacuum, Asslar, Germany, *TMH-071YP)* is turned on at a pressure of approximately 1 Pa (measured at P_{LV}). The high vacuum is measured by a cold-cathode pressure gauge (P_{HV}) (Pfeiffer Vacuum, *PKR-251*). This filling station was tested to a vacuum of 10^{-7} mbar (10^{-5} Pa).

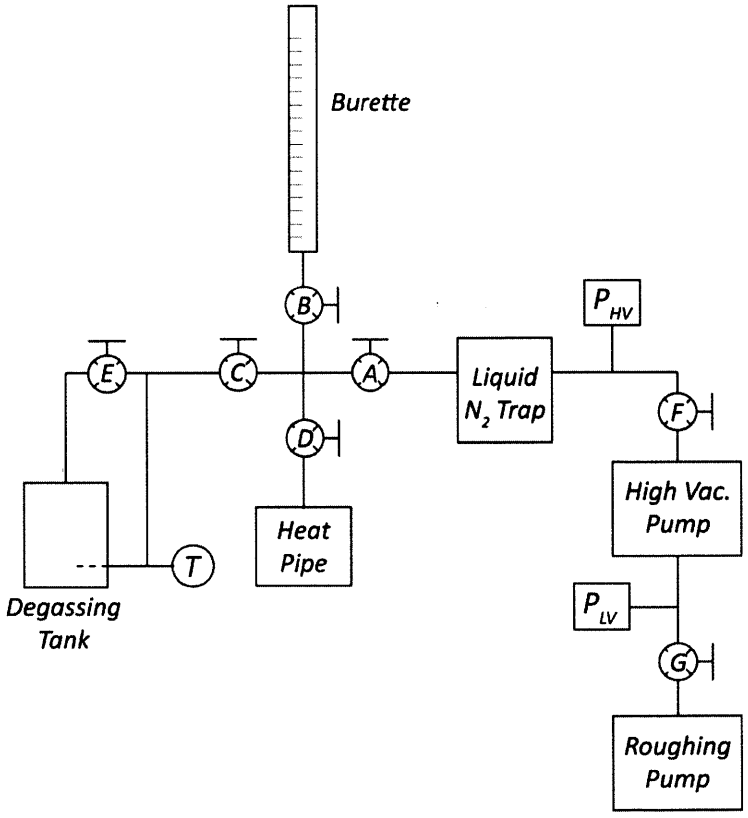

Figure C.1. Layout of the heat pipe filling station. The letters label the valves, and "P" and "T" indicate the pressure gauges and thermocouple, respectively. "HV" and "LV" indicate "high vacuum" and "low vacuum," respectively.

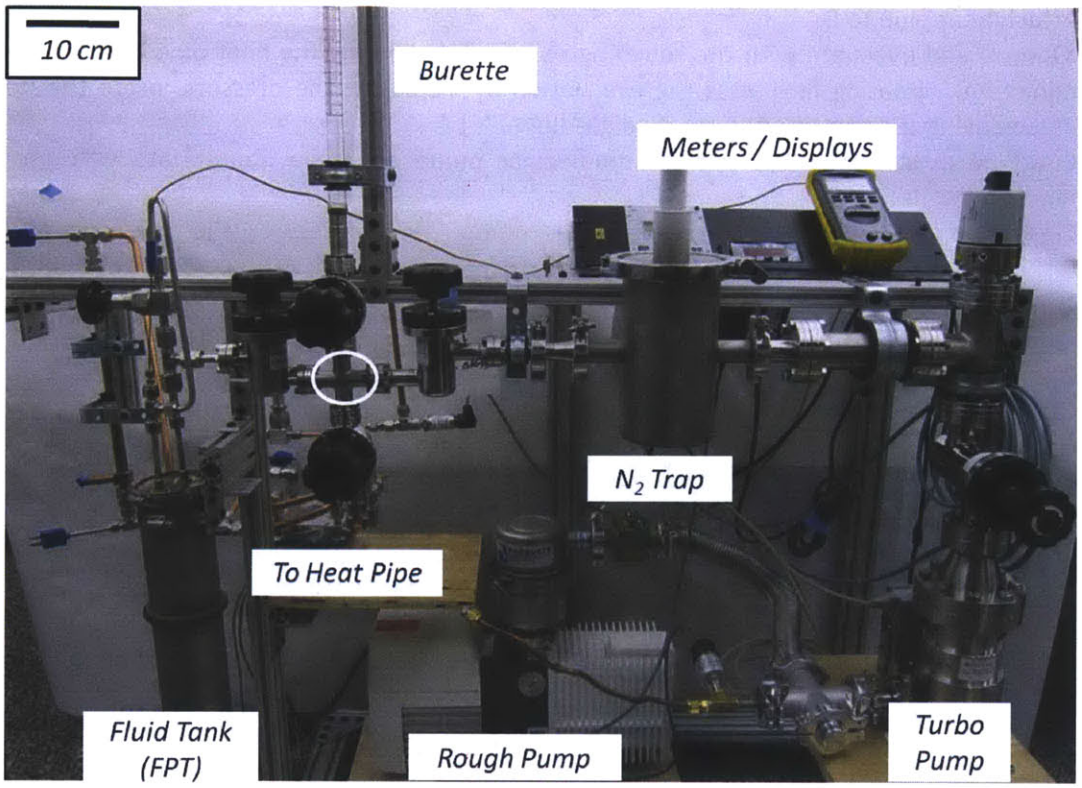

Figure C.2. Photograph of the filling station. The position of the components is similar to that shown in Figure C.1. As a reference, the four-way intersection is circled in the photograph with a white line.

Several precautionary features are implemented in this design to eliminate the possibility of leaks. Bellows valves are used for all valves in the high vacuum side (valves A-F), so that the high vacuum chamber/piping is completely separated from the ambient. Also, all connections in the high vacuum side are of the Con-Flat, compression gasket type. Exceptions to this include the liquid nitrogen trap, which uses o-ring compression seals, and the narrow piping connecting the FPT tank, which are ferrule-type compression fittings. The borosilicate (PYREX) burette is custom welded to stainless steel adapter so that a Con-Flat type connection can be used. To prevent contamination, the station is completely evacuated when not in use.

C.4 Operating Procedure

The following outlines the procedure for evacuating the heat pipe, de-gassing the working fluid (water), and filling.

1) Begin with all valves closed.
2) Fill nitrogen trap with liquid nitrogen and maintain the tank at least half full.
3) Open valves F (hereon "F") and G, and evacuate the vacuum leg with the roughing pump.

A) Evacuation of heat pipe

4) Attach heat pipe to D.
5) Open D and evacuate with the roughing pump while heating the heat pipe to 60+ °C (3 hours minimum). Heating facilitates the evacuation by increasing the pressure inside the heat pipe and delaying the transition to rarefied gas flow [76].
6) Continue evacuation with the turbomolecular pump once the appropriate vacuum level is reached (~1 Pa).
7) Close D and turn off the turbomolecular pump. In contrast to the roughing pump, the turbomolecular pump cannot be subjected to pressure shock (abrupt change in pressure of greater than 50 Pa).

B) Evacuation of burette

8) Open B and evacuate the burette with the roughing pump.
9) Continue evacuation with the turbomolecular pump once the appropriate vacuum level is reached (~1 Pa).
10) Close B and turn off the turbomolecular pump.

C) De-gassing the working fluid (water)

11) Introduce water into the FPT tank by removing valve E and injecting into the tank with a syringe.
12) Reattach the valve to close the filing station.
13) Cool the FPT by immersing the tank in a bath of liquid nitrogen or a slurry of dry ice (dry ice + alcohol, such as ethanol) to freeze the water. This step is complete only when all of the water is completely frozen.
14) Open E and C, and evacuate the FPT tank with the roughing then the turbomolecular pump. Care must be taken to avoid cryogenic temperatures in the FPT tank, since gases condensable at such temperatures, such as oxygen and carbon dioxide, may condense in the tank and may not be evacuated easily.
15) Close C , turn off the turbomolecular pump and allow the water to thaw. A heater can be used for thawing.
16) Repeat 3 times.
17) Close E and C.

*NOTE: steps A, B, and C may be performed in any order

D) Filling the heat pipe

18) Heat the FPT tank to raise the vapor pressure. The temperature is raised to ~100 °C for the present filling station. This pressure is required to send the liquid into the burette; the vapor pressure is required to drive the liquid into the burette against the gravitational pressure head. A taller burette will require a larger pressure.
19) Open B then C, and allow the liquid to enter the burette. A sufficient volume is required in the FPT tank to fully fill the burette. Note that the all of the piping between the FPT tank and the burette will also be filled with liquid.
20) Close C.
21) Cool the four-way intersection and burette to room temperature. Failure to cool any location filled with liquid will result in: 1) boiling when D is opened to fill the heat pipe, which will prevent a steady measurement with the burette; and 2) loss of accuracy in the measurement of filling volume due to the non-uniform liquid density.
22) Open D and allow the liquid to enter the evacuated heat pipe by the desired amount by viewing the volume change in the burette.

References

1. International Technology Roadmap for Semiconductors, *Assembly and Packaging*. 2010. p. 1-62.
2. Accel La Habra. 2012; Available from: http://www.accelthermal.com/index4c65.html?page_id=116.
3. Trutassanawin, S., et al., *Experimental Investigation of a Miniature-Scale Refrigeration System for Electronics Cooling.* IEEE Transactions on Components and Packaging Technologies, 2006. **29**(3): p. 678-687.
4. Pettes, A.M., M.S. Hodes, and K.E. Goodson, *Optimized Thermoelectric Refrigeration in the Presence of Thermal Boundary Resistance.* IEEE Transactions on Advanced Packaging, 2009. **32**(2): p. 423-430.
5. Hodes, M., *Optimal Design of Thermoelectric Refrigerators Embedded in a Thermal Resistance Network.* IEEE Transactions on Components, Packaging and Manufacturing Technology, 2012. **2**(3): p. 483-495.
6. Astrain, D., J.G. Vián, and M. Domínguez, *Increase of COP in the thermoelectric refrigeration by the optimization of heat dissipation.* Applied Thermal Engineering, 2003. **23**(17): p. 2183-2200.
7. Ebadian, M.A. and C.X. Lin, *A Review of High-Heat-Flux Heat Removal Technologies.* Journal of Heat Transfer, 2011. **133**(11): p. 110801-11.
8. Kandlikar, S.G., *Heat Transfer and Fluid Flow in Minichannels and Microchannels*. 2006, Oxford, UK: Elsevier Science Ltd.
9. Tuckerman, D.B. and R.F.W. Pease, *High-performance Heat Sinking for VLSI.* Electron Device Letters, 1981. **2**(5): p. 126-129.
10. Fabbri, M., S. Jiang, and V.K. Dhir, *A Comparative Study of Cooling of High Power Density Electronics Using Sprays and Microjets.* Journal of Heat Transfer, 2005. **127**(1): p. 38-48.
11. Bowers, M.B. and I. Mudawar, *High Flux Boiling in Low Flow Rate, Low Pressure Drop Mini-Channel and Micro-Channel Heat Sinks.* International Journal of Heat and Mass Transfer, 1994. **37**(2): p. 321-332.
12. Brutin, D. and L. Tadrist, *Pressure drop and heat transfer analysis of flow boiling in a minichannel: influence of the inlet condition on two-phase flow stability.* International Journal of Heat and Mass Transfer, 2004. **47**(10–11): p. 2365-2377.
13. Qu, W. and A. Siu-Ho, *Experimental Study of Saturated Flow Boiling Heat Transfer in an Array of Staggered Micro-pin-fins.* International Journal of Heat and Mass Transfer, 2009. **52**(7–8): p. 1853-1863.
14. Qu, W. and I. Mudawar, *Flow Boiling Heat Transfer in Two-hase Micro-channel Heat Sinks—I. Experimental Investigation and Sssessment of Correlation Methods.* International Journal of Heat and Mass Transfer, 2003. **46**(15): p. 2755-2771.
15. Qu, W. and A. Siu-Ho, *Measurement and prediction of pressure drop in a two-phase micro-pin-fin heat sink.* International Journal of Heat and Mass Transfer, 2009. **52**(21–22): p. 5173-5184.
16. Sung, M.K. and I. Mudawar, *Single-Phase and Two-Phase Hybrid Cooling Schemes for High-Heat-Flux Thermal Management of Defense Electronics.* Journal of Electronic Packaging, 2009. **131**(2): p. 021013-10.
17. Sung, M.K. and I. Mudawar. *Single-phase and Two-phase Hybrid Cooling Schemes for High-heat-flux Thermal Management of Defense Electronics.* in *11th Intersociety Conference on Thermal and Thermomechanical Phenomena in Electronic Systems*. 2008. Orlando, FL.

18. Reay, D. and P. Kew, *Heat Pipes, Fifth Edition: Theory, Design and Applications*. 2006, Oxford, UK: Elsevier Science Ltd.
19. Faghri, A., *Heat Pipe Science and Technology*. 1995, New York, NY: Taylor and Francis.
20. Peterson, G.P., *An Introduction to Heat Pipes: Modeling, Testing, and Applications*. 1994, New York, NY: John Wiley & Sons.
21. Vasiliev, L.L., *Heat Pipes in Modern Heat Exchangers.* Applied Thermal Engineering, 2005. **25**(1): p. 1-19.
22. Thermacore Europe. Available from: http://www.thermacore.co.uk/loop-heat-pipes.
23. Maydanik, Y.F., *Loop heat pipes.* Applied Thermal Engineering, 2005. **25**(5–6): p. 635-657.
24. Charoensawan, P., et al., *Closed Loop Pulsating Heat Pipes: Part A: Parametric Experimental Investigations.* Applied Thermal Engineering, 2003. **23**(16): p. 2009-2020.
25. Riehl, R.R., *Characteristics of an Open Loop Pulsating Heat Pipe*, in *34th International Conference on Environmental Systems*. 2004, SAE International: Colorado Springs, Colorado.
26. Khandekar, S., N. Dollinger, and M. Groll, *Understanding operational regimes of closed loop pulsating heat pipes: an experimental study.* Applied Thermal Engineering, 2003. **23**(6): p. 707-719.
27. OCZ. 2012; Available from: http://www.ocztechnology.com/ocz-vendetta-cpu-cooler-eol.html.
28. Defense Advanced Research Projects Agency, *Broad Agency Announcement: Microtechnologies for Air-Cooled Exchangers (MACE)*. 2008. p. 1-30.
29. Jenicek, D.P., *Design of Low-power Permanent-magnet Synchronous Motor for Use in High-density Heat Pump*. 2011, Massachusetts Institute of Technology: Cambridge, MA.
30. Staats, W.L., *Active Heat Transfer Enhancement in Integrated Fan Heat Sinks*. 2012, Massachusetts Institute of Technology: Cambridge, MA.
31. Allison, J.M., *Air Flow in a High Aspect Ratio Heat Sink*. 2010, Massachusetts Institute of Technology: Cambridge, MA.
32. Nikitkin, M. and B. Cullimore, *CPL and LHP Technologies: What are the Differences, What are the Similarities?*, in *28th International Conference on Environmental Systems*. 1998, SAE International: Danvers, MA.
33. Ku, J., *Operating Characteristics of Loop Heat Pipes*, in *29th International Conference on Environmental Systems*. 1999, SAE International: Denver, Colorado.
34. Butler, D., J. Ku, and T. Swanson, *Loop Heat Pipes and Capillary Pumped Loops-an Applications Perspective*, in *Space Technology and Applications International Forum*. 2002, American Institute of Physics: Albuquerque, NM.
35. Kaya, T. and J. Ku, *A Parametric Study of Performance Characteristics of Loop Heat Pipes*, in *29th International Conference on Environmental Systems*. 1999, SAE International: Denver, CO.
36. Ku, J., *Methods of Controlling the Loop Heat Pipe Operating Temperature*, in *38th International Conference on Environmental Systems*. 2008, SAE International: San Francisco, CA.
37. Pastukhov, V.G., et al., *Miniature Loop Heat Pipes for Electronics Cooling.* Applied Thermal Engineering, 2003. **23**(9): p. 1125-1135.
38. Nagano, H. and J. Ku, *Start-up Behavior of a Miniature Loop Heat Pipe with Multiple Evaporators and Multiple Condensers*, in *45th Aerospace Sciences Meeting and Exhibit*. 2007: Reno, NV.
39. Maydanik, Y.F., et al., *Development and Test Results of a Multi-Evaporator-Condenser Loop Heat Pipe*, in *Space Technology and Applications International Forum*. 2003: Albuquerque, NM. p. 42-48.
40. Ku, J., L. Ottenstein, and G. Birur, *Thermal Performance of a Multi-Evaporator Loop Heat Pipe with Thermal Masses and Thermal Electical Coolers*, in *13th International Heat Pipe Conference*. 2004: Shanghai, China.

41. Anderson, W.G., et al., *Electronics Cooling Using High Temperature Loop Heat Pipes With Multiple Condensers*, in *Power Systems Conference*. 2010, SAE International: Fort Worth, TX.
42. Muto, M., et al., *Thermal Behavior of a Double-Condenser Design LHP for Monitor of All-sky X-ray Image*, in *32nd International Conference on Environmental Systems*. 2002, SAE International: San Antonio, TX.
43. Kaya, T. and J. Ku, *Thermal Operational Characteristics of a Small-Loop Heat Pipe.* Journal of Thermophysics and Heat Transfer, 2003. **17**(4): p. 464-470.
44. Vasiliev, L., et al., *Loop Heat Pipe for Cooling of High-power Electronic Components.* International Journal of Heat and Mass Transfer, 2009. **52**(1–2): p. 301-308.
45. Singh, R., et al., *Miniature Loop Heat Pipe With Flat Evaporator for Cooling Computer CPU.* IEEE Transactions on Components and Packaging Technologies, 2007. **30**(1): p. 42-49.
46. Nagano, H. and J. Ku, *Gravity Effect on Capillary Limit in a Miniature Loop Heat Pipe with Multiple Evaporators and Multiple Condensers*, in *Space Technology and Applications International Forum*. 2007: Albuquerque, NM.
47. Ku, J. and H. Nagano, *Effects of Gravity on Start-up and Heat Load Sharing of a Miniature Loop Heat Pipe*, in *37th International Conference on Environmental Systems*. 2007, SAE International: Chicago, IL.
48. Kaya, T., et al., *Mathematical Modeling of Loop Heat Pipes*, in *37th Aerospace Sciences Meeting and Exhibit*. 1999: Reno, NV.
49. Kaya, T. and T.T. Hoang, *Mathematical Modeling of Loop Heat Pipes and Experimental Validation.* Journal of Thermophysics and Heat Transfer, 1999. **13**(3): p. 314-320.
50. Hoang, T.T. and J. Ku, *Mathematical Modeling of Loop Heat Pipes with Multiple Evaporators and Multiple Condensers*, in *3rd International Energy Conversion Engineering Conference*. 2005: San Francisco, CA.
51. Furukawa, M., *Model-Based Method of Theoretical Design Analysis of a Loop Heat Pipe.* Journal of Thermophysics and Heat Transfer, 2006. **20**(1): p. 111-121.
52. Adoni, A.A., et al., *Thermohydraulic Modeling of Capillary Pumped Loop and Loop Heat Pipe.* Journal of Thermophysics and Heat Transfer, 2007. **21**(2): p. 410-421.
53. Launay, S., V. Sartre, and J. Bonjour, *Analytical Model for Characteriation of Loop Heat Pipes.* Journal of Thermophysics and Heat Transfer, 2008. **22**(4): p. 632-631.
54. Launay, S., et al., *Transient Modeling of Loop Heat Pipes for the Oscillating Behavior Study.* Journal of Thermophysics and Heat Transfer, 2007. **21**(3): p. 487-495.
55. Kaya, T., et al., *Numerical simulation of transient operation of loop heat pipes.* Applied Thermal Engineering, 2008. **28**(8–9): p. 967-974.
56. Munson, B.R., D.F. Young, and T.H. Okiishi, *Fundamentals of Fluid Mechanics*. Fourth Edition ed. 2002, New York, NY: John Wiley & Sons.
57. Green, D.W. and R.H. Perry, *Perry's Chemical Engineer's Handbook*. Eighth Edition ed. 2008, New York, NY: McGraw Hill.
58. Mills, A.F., *Heat Transfer*. Second Edition ed. 1999, Upper Saddle River, NJ: Prentice Hall.
59. Domínguez Espinosa, F.A., *Effect of Fabrication Parameters on Thermophysical Properties of Sintered Wicks*. 2011, Massachusetts Institute of Technology: Cambridge, MA.
60. Anderson, W.G., et al., *High Temperature Titanium/Water and Monel/Water Heat Pipes* in *4th International Energy Conversion Engineering Conference and Exhibit* 2006: San Diego, CA.
61. Pittinato, G.F., *Hydrogen Gas Generation in Water Heat Pipes.* Journal of Engineering Materials and Technology, 1978. **100**(3): p. 313-318.
62. Petrick, S.W., *Hydrogen Gas Generation in Water/ Stainless Steel Heat Pipes*, in *Winter Annual Meeting of the American Society of Mechanical Engineers*. 1972, ASME: New York, NY.

63. Rosenfeld, J.H. and N. Gernert, J., *Life Test Results for Water Heat Pipes Operating at 200 °C to 300 °C*, in *Space Technology and Applications International Forum*. 2008: Albuquerque, NM.
64. Riehl, R.R. and T.C.P.A. Siqueira, *Heat Transport Capability and Compensation Chamber Influence in Loop Heat Pipes Performance.* Applied Thermal Engineering, 2006. **26**(11–12): p. 1158-1168.
65. Ren, C., Q.-S. Wu, and M.-B. Hu, *Heat Transfer with Flow and Evaporation in Loop Heat Pipe's Wick at Low or Moderate Heat Fluxes.* International Journal of Heat and Mass Transfer, 2007. **50**(11–12): p. 2296-2308.
66. Hanks, D.F., *Design, Fabrication, and Characterization of a Muilti-Condenser Loop Heat Pipe*. 2012, Massachusetts Institute of Technology: Cambridge, MA.
67. Rodriguez, J.I. and A. Na-Nakornpanom, *Investigation of Transient Temperature Oscillations of a Propylene Loop Heat Pipe*, in *31st International Conference on Environmental Systems*. 2001, SAE International: Orlando, FL.
68. Ku, J. and J.I. Rodriguez, *Low Frequency High Amplitude Temperature Oscillations in Loop Heat Pipe Operation*, in *33rd International Conference on Environmental Systems*. 2003, SAE International: Vancouver, B.C.
69. Goncharov, K.A., et al., *Investigation of Temperature Fluctuations in Loop Heat Pipes*, in *24th International Conference on Environmental Systems*. 1994, SAE International: Friedrichshafen, Germany.
70. Muraoka, I., F.M. Ramos, and V.V. Vlassov, *Analysis of the Operational Characteristics and Limits of a Loop Heat Pipe with Porous Element in the Condenser.* International Journal of Heat and Mass Transfer, 2001. **44**(12): p. 2287-2297.
71. Sun, K.H. and C.L. Tien, *Thermal Performance Characteristics of Heat Pipes.* International Journal of Heat and Mass Transfer, 1975. **18**(3): p. 363-380.
72. National Engineering Laboratory, *Analysis, Design and Manufacture of Heat Pipes, Course Papers*. 1973, East Killbride, UK: Birniehill Institute.
73. Chi, S.W., *Heat Pipe Theory and Practice*. 1976, New York, NY: McGraw-Hill.
74. de Bock, H.P.J., et al. *On the charging and thermal characterization of a micro/nano structured thermal ground plane*. in *12th IEEE Intersociety Conference on Thermal and Thermomechanical Phenomena in Electronic Systems*. 2010. LAs Vegas, NV.
75. Cao, Y., M. Gao, and E. Pinilla. *Fabrication and test of a filling station for micro/miniature devices*. in *Proceedings of the 32nd Intersociety Energy Conversion Engineering Conference,*. 1997. Honolulu, HI.
76. Lafferty, J.M., *Foundations of Vacuum Science and Technology*. 1998, New York, NY: John Wiley & Sons.